Analysis of a 3D optical scanner based on photogrammetry suitable for industrial applications in close and micro-range

Politecnico di Bari

Department of Mechanics, Mathematics and Management

MECHANICAL AND MANAGEMENT ENGINEERING

Ph.D. Program

SSD: ING-IND/16

Final Dissertation

Analysis of a 3D optical scanner based on photogrammetry suitable for industrial applications in close and micro-range

---

by

GUERRA MARIA GRAZIA

Referees:

Prof.ssa Elisabetta Ceretti

Prof. Michele Dassisti

Supervisor:

Prof. LUIGI M. GALANTUCCI

_____

Coordinator of Ph.D Program:

Prof. GIUSEPPE P. DEMELIO

_____*firma*

Course n°31, 01/11/2015-31/10/2018

Abstract

The new paradigm of Industry 4.0 encompasses the manufacturing metrology and the necessity for fast, flexible, reliable and holistic systems arises, in order to accompany the more advanced manufacturing technologies. The more extensive use of additive manufacturing techniques, which entail the realization of complex structures and freeform geometries, as well as, the use of new materials, enhances this concept.
These driving forces are the basis for the great interest towards 3D scanning systems because they perfectly fit the key factors of the new manufacturing metrology 4.0. Among other things, they have the capacity to reconstruct complete and detailed 3D models in a very short time, which makes them suitable for on-machine verification.
In this context, close-range photogrammetry is recognized as a simple, versatile, and effective methodology for 3D measurements of components, even if they are characterized by a prevailing dimension respect to the others (e.g. height is much higher than length or vice versa), complex free form geometry, and under-cuts. Moreover, it is able to provide accurate measurements and 3D photorealistic (thanks to the computation of the texture) surface reconstructions in a simple and inexpensive way, as well as in very short time. Photogrammetry-based systems and, generally, optical-based techniques, are flexible and holistic systems, but their strengths are also their weaknesses, because this complexity results in more variables involved and more sources of error affecting the results.
The present thesis is focused on the development and the analysis of an optical 3D scanner based on photogrammetry, suitable for measurements of complex parts in close and micro range. The analysis started from the identification of the main sources of error affecting the measuring system, with the final goal to include them in a proper uncertainty assessment. In particular, there are errors due to the measuring system itself, errors due to the object under measurement, i.e. errors due to the manufacturing process, as well as, errors due to the interaction of the specific system with the object (materials, colours and surface texture). Thus, the uncertainty evaluation of such systems is still an open issue.

The first chapters are dedicated to the state of the art of currently available measuring techniques, highlighting the main advantages and drawbacks, in order to explain the importance of developing a photogrammetry-based system for industrial application.
The third chapter is of fundamental importance since it describes the state of the art of the currently available standards in 3D optical scanning. They mainly refer to the VDI/VDE 2634 series, in the form of acceptance and reverification test. In addition, the standards usually used for the uncertainty assessment of the more reliable Coordinate Measuring Machine (CMMs), such as the ISO 15530-3, were described, highlighting the main criticalities and the possible adaptation for optical-based scanners.
The *forth chapter* is entirely dedicated to photogrammetry-based systems, with a brief introduction to the state of the art when applying photogrammetry in close and micro range, a description of the measuring principle through the mathematical models behind and the main advances carried out in the development of the reconstruction software algorithms. Then, the photogrammetry-based system is presented together with the sensors and the

optical equipment used throughout the thesis. Finally, a summary of the main criticalities is reported.
The experimental investigations carried out during the PhD course are collected in the chapters from 5 to 11. Each chapter is dedicated to a specific measuring task, with the aim to analyse a specific aspect or a criticality of the photogrammetry- based system under exam.
The *fifth chapter* is focused on the analysis of repeatability of the photogrammetric reconstruction software used, which has proved to be a fundamental part of the system. The study was conducted on a pyramidal artefact already used in previous experiments.
In the *sixth chapter*, a new three-dimensional reference artefact was presented. The purpose was double: for the estimation of the external orientation, *scale adjustment*, and for the uncertainty assessment, *calibration*. The effectiveness of this reference artefact was proved through the reconstruction of the test object used in the previous chapter, the pyramidal artefact.
The capacity of the presented system to reconstruct free form geometries was analysed through a preliminary test in *Chapter 7*. The tests were performed through the use of three artefacts produced by additive manufacturing techniques, which were a customized version of the NPL free form artefact designed and developed by NPL institute. The need for the customization was mainly due to the necessity to resize the artefact to make it measurable with the optical equipment under exam.
In *Chapter 8*, the application of the photogrammetry-based system for measuring additive manufactured biomedical devices was reported, highlighting critical aspects due to their object and surface textures characteristics.
Chapters 9 and 10 report the work conducted during the external stay period at the Department of Mechanical Engineering of the Denmark Technical University. The introduction of a step gauge reference artefact was analysed, and the photogrammetry-based system was then compared with other non-contact measuring techniques, such as structured light scanner, laser based scanner and a computed tomography scanner. The performance verification of all those 3D non-contact measuring techniques was conducted through the step gauge reference artefact. In chapter 10, the investigation was focused on the analysis of the interaction between the 3D optical scanning systems and the materials and colours of the objects under measurements. For the purpose, five miniature step gauges made of different polymeric materials and colours were scanned and analyzed.
Finally, *Chapter 11* is dedicated to the application of the photogrammetry to the microscopic range, for the acquisition of components realized through μEDM (Electro Discharge Machining). The optical equipment, used in this investigation, allowed to reach magnification levels higher than 2x, with optical resolutions up to 2,4 μm. The investigation was mainly focused on the verification of the reproducibility of the internal parameters estimated through the traditional mathematical models, for such magnification levels.

Introduzione

Il nuovo paradigma dell'Industria 4.0 coinvolge anche il settore della metrologia, sollevando la necessità di sistemi veloci, flessibili, affidabili e olistici, per accompagnare lo sviluppo delle tecnologie manifatturiere più avanzate. L'uso più estensivo delle tecnologie additive di produzione ha comportato la realizzazione di componenti dale geometrie molto complesse nonché l'utilizzo di nuovi materiali. Queste principi trainanti sono la base per il grande interesse nei confronti dei sistemi di scansione 3D perché si adattano perfettamente ai fattori chiave della nuova Metrologia 4.0. Questi sistemi presentano diversi vantaggi. Tra tutti, hanno la capacità di ricostruire modelli 3D completi e dettagliati in brevissimo tempo, il che li rende adatti per la *on-machine verification*. Al momento, i sistemi di misura a contatto sono considerati i sistemi più affidabili, anche se hanno molti svantaggi, soprattutto quando sono utilizzati per misurare superfici free form in modalità di scansione.
In questo contesto, la fotogrammetria close range è riconosciuta come una metodologia semplice, versatile ed efficace nel rilevamento di superfici e nella misurazione 3D di componenti, anche in presenza di alti rapport di aspetto (ad esempio, l'altezza è molto più alta della lunghezza o viceversa), geometrie free form e sottosquadri. Attraverso la combinazione tra i movimenti di rotazione e traslazione di una fotocamera e il campione da misurare, è possibile coprire l'intero volume di misura da diversi punti di ripresa, sfruttando la grande versatilitá del sistema attraverso diverse strategie di scansione. Un sistema basato sulla fotogrammetria é inoltre in grado di fornire misurazioni accurate e ricostruzioni di superfici 3D fotorealistiche (grazie al calcolo della *texture*) in modo semplice ed economico, nonché in tempi brevissimi.
La presente tesi è incentrata sullo sviluppo e l'analisi di uno scanner ottico 3D basato su fotogrammetria, adatto per scansioni di parti complesse nel close e micro-range. L'analisi è partita dalla necessità di identificare le principali fonti di errore che interessano uno scanner ottico 3D e, in particolare, uno scanner basato sulla fotogrammetria, con l'obiettivo finale di includere le varie componenti in una piú complete valutazione dell'incertezza. La valutazione dell'incertezza di tali sistemi è ancora un problema aperto, anche se sono stati compiuti molti sforzi in tal senso. I sistemi basati sulla fotogrammetria e, in generale, le tecniche di scansione ottica, hanno il grande vantaggio di acquisire grandi quantità di punti in brevissimo tempo, sono sistemi flessibili e olistici, ma questi grandi vantaggi sono anche delle debolezze, perché maggiore é la complessitá di un sistema, più sono le variabili coinvolte e più fonti di errore influenzano i risultati.
L'approccio seguito in questa tesi è stato quello di identificare e analizzare alcuni dei principali errori che interessano il sistema, considerando sia gli errori dovuti al sistema stesso, cosí come gli errori dovuti all'oggetto sottoposto a verifica dimensionale (errori dovuti al processo di fabbricazione), nonché errori dovuti all'interazione del sistema di misura specifico con la superficie dell'oggetto (materiali, colori e texture superficiale).
I primi capitoli sono dedicati allo stato dell'arte delle tecniche di misurazione attualmente disponibili, evidenziando i principali vantaggi e svantaggi, al fine di spiegare l'importanza di sviluppare un sistema ottico per applicazioni industriali.

Il terzo capitolo è di fondamentale importanza e descrive lo stato dell'arte degli standard attualmente disponibili per la scansione ottica 3D evidenziando le principali problematiche e criticità.

Il quarto capitolo è interamente dedicato ai sistemi basati sulla fotogrammetria, con una breve descrizione dello stato dell'arte della tecnica fotogrammetrica applicata nel close e micro range, una descrizione del principio di misurazione attraverso la descrizione dei modelli matematici alla base della tecnica e i principali progressi nello sviluppo di algoritmi software. Infine, viene riportato un riassunto delle principali fonti di errore che interessano questo tipo di sistema.

Nei capitoli dal quinto all'undicesimo, sono raccolte le indagini sperimentali svolte durante il corso del dottorato, incentrate sull'analisi di specifiche criticità del sistema di scansione in esame.

Il quinto capitolo è incentrato sull'analisi della ripetibilità del software di ricostruzione fotogrammetrica utilizzato, che si è dimostrato essere una parte fondamentale del sistema. Lo studio è stato condotto su un provino di forma piramidale già utilizzato in precedenti esperimenti.

Nel sesto capitolo è stato presentato un nuovo oggetto di riferimento. Lo scopo della sua implementazione era duplice: per la stima dell'orientamento esterno, che include il calcolo del fattore di scala, e per la valutazione dell'incertezza (calibrazione del sistema). L'efficacia di questo oggetto di riferimento è stata dimostrata attraverso la ricostruzione dell'oggetto di test utilizzato nel capitolo precedente, il provino di forma piramidale.

La capacità del sistema presentato nella ricostruzione di geometrie free form è stata analizzata attraverso un test preliminare nel capitolo 7. Il test é stati eseguito mediante l'uso di tre artefatti prodotti con tecniche di produzione additiva, che erano una versione custom dello standard fisico progettato e sviluppato dall'istituto NPL. La necessità della personalizzazione era principalmente dovuta alla necessità di ridimensionare l'artefatto per renderlo acquisibile e misurabile con la configurazione ottica in esame.

Nel capitolo 8 è stata riportata l'applicazione del sistema basato sulla fotogrammetria per misurare i dispositivi biomedicali prodotti con tecniche additive, evidenziando aspetti critici dovuti alle caratteristiche di tessitura superficiale di questi provini.

I capitoli 9 e 10 riportano il lavoro svolto durante l'esperienza all'estero presso il Dipartimento di ingegneria meccanica dell'Università Tecnica della Danimarca. Durante questo period, é stata analizzata l'introduzione di uno step gauge come oggetto di riferimento. Il sistema basato sulla fotogrammetria è stato quindi confrontato con altre tecniche di misurazione senza contatto, come uno scanner a luce strutturata, uno scanner laser e uno scanner per tomografia computerizzata. La verifica delle prestazioni delle suddette tecniche di misurazione senza contatto è stata, quindi, descritta.

Nel capitolo 10, l'indagine si è concentrata sull'analisi dell'interazione tra i sistemi di scansione ottica

3D e i materiali e i colori degli oggetti sottoposti a misurazione. Allo scopo, sono stati scansionati e analizzati cinque step gauges miniaturizzati e realizzati con diversi materiali, tutti polimerici, e diversi colori.

Infine, il capitolo 11 è dedicato all'applicazione della fotogrammetria al range microscopico, per l'acquisizione di componenti realizzati tramite µEDM (Electro Discharge Machining).

Contents

List of Figures

List of Tables

Chapter 1 - Driving Forces

Advanced digital technology is not a new concept in the manufacturing field and the new Industry 4.0 is going to change significantly the world of the industrial production. Advanced manufacturing is, indeed, an underpinning technology of Industry 4.0 and it is marked by a shift toward a physical-to-digital-to-physical connection (*Figure 1*). The main concept is commonly understood as creating a close connection between manufacturing industry and information technology. In this context, the definition of cyber-physical production systems (CPPSs) is of paramount importance. These systems are a special form of the cyber-physical systems (CPSs), which are defined by VDI/VDE technical committees, as systems linking real (physical) objects and processes to information-processing (virtual) objects and processes through global information networks, which ensure the connection at any time. With the purpose of linking the virtual and real world, sensors, which often have a measuring function, are used. The actual status, acquired by a sensor, is transferred into the “cyber-world” as actual data in order to derive pro-cess information, collect it in databases and use it as a basis for the adaptation of the models to the real situation [1].

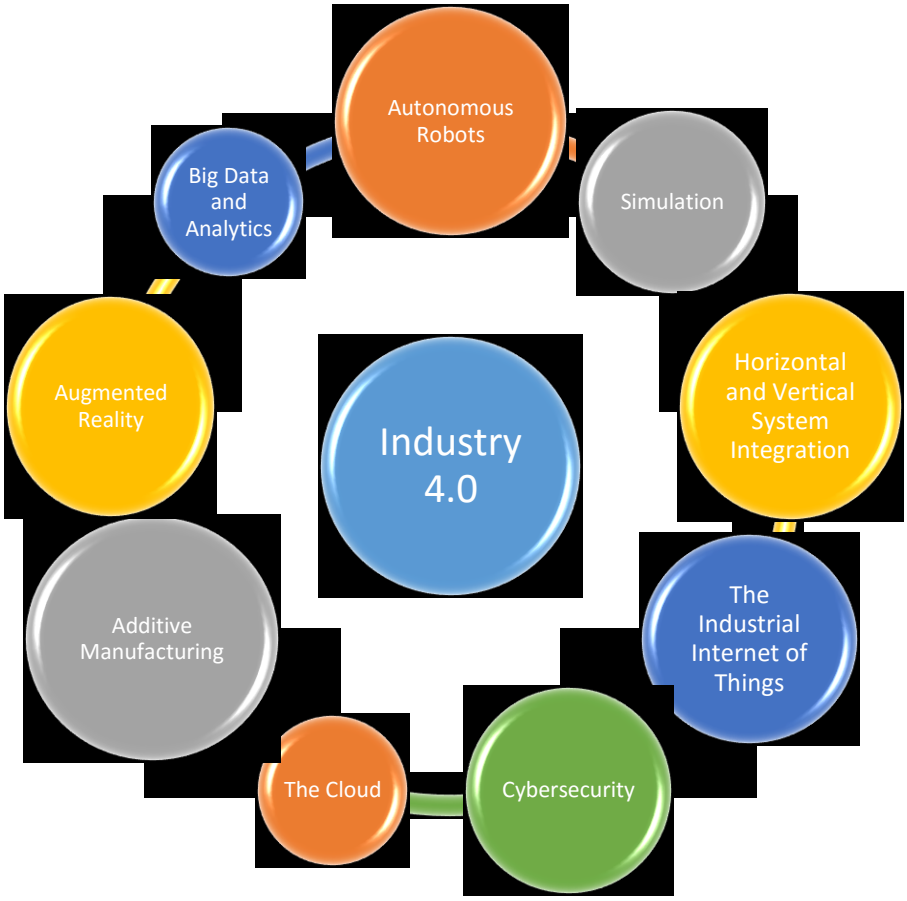

Figure 1 Industry 4.0 - Main Challenges.

1.1 "Manufacturing Metrology 2020"

It is clear that the transformation intrinsically defined in the concept of Industry 4.0 encompasses all the steps involved in the production field and measurement technology must adapt itself to the future trends and challenges in metrology [2]. The term "Measurement Technology 4.0" let understand the need for a change in this field and the main keys for this transformation were identified in the roadmap, under the title "Manufacturing Metrology 2020". The key words are ***fast***, ***accurate***, ***reliable*** and ***flexible***. Afterword, the term ***holistic*** was added, see *Figure 2*.

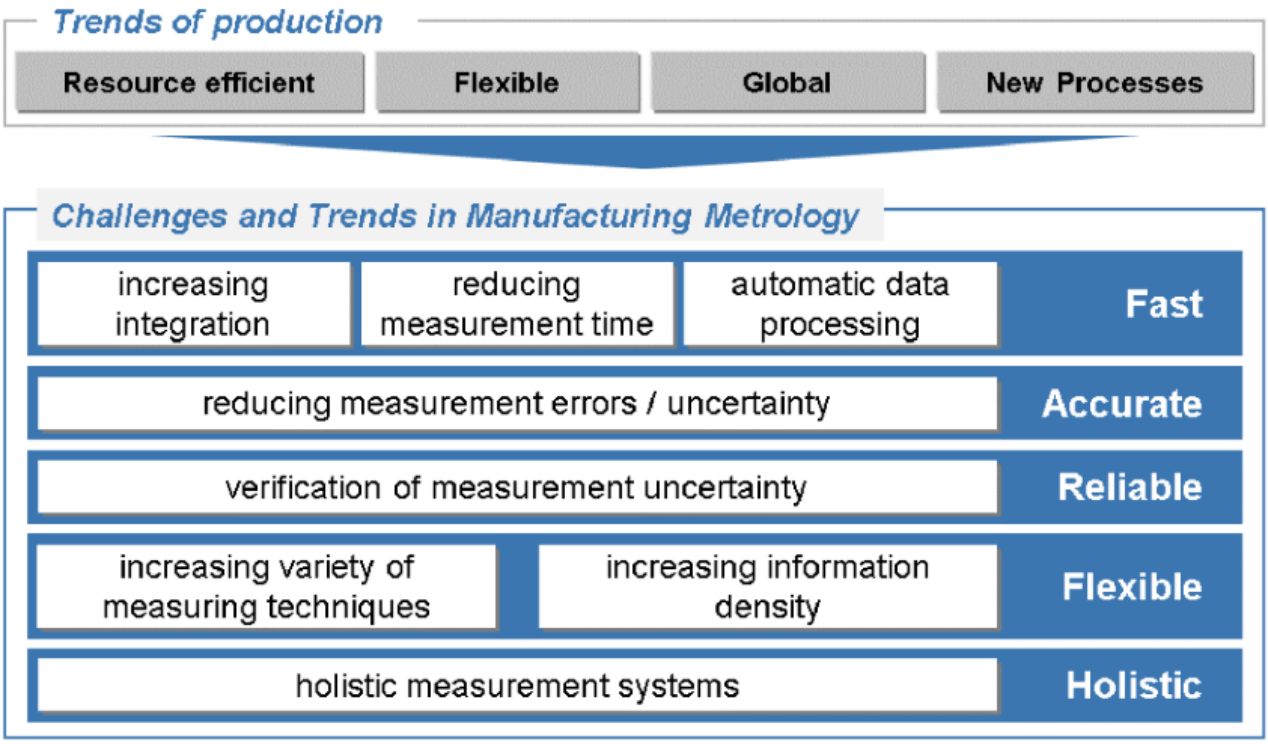

Figure 2 Challenges and Trends in Manufacturing Metrology [2].

1.1.1Fast

The term "fast" is related to the speed in delivering conformity checking and process control information in production, in order to avoid the slowing down of the production process. This rapidity is obtained on one hand, through quicker measuring techniques and, on the other hand, through the integration of the measurement technology, or technologies, into production processes, making the process fully or partially automated. In this context, in process and on–machine measurements have to be preferred respect to the metrological verification carried out in the laboratories. At the time being, contact probe systems are considered the most reliable systems for on-machine verification, but they have many drawbacks, especially when they are used to measure free form surfaces in scanning mode. Optical techniques have the great advantage to acquire large amounts of points in very short time, and they can be used for several applications: from dimensional verification of manufactured products to the inspection of damaged parts for repairing processes.

1.1.2 Accurate

According to the new definition of the VIM [3] is "*the closeness of agreement between a measured quantity value and a true quantity value of a measurand*" and it is not identifiable by a numerical value but it is a generic word. Its concept is related to the concept of trueness, as well as, to the concept of uncertainty of measurement. The final goal is the reduction of the total uncertainty, since it has to be considered in the conformity check of new manufactured parts, according to the ISO 14253-1[4]. Thus, it plays a fundamental role in the production environment. The reduction of the total uncertainty is one key point of the roadmaps of EURAMET (European Association of National Metrology Institutes) and it starts from decreasing the uncertainty of the

measuring instruments (sensors, transducers), improving, more generically, their accuracy. They are included in the traceability chain, often described as a pyramidal hierarchy, which provides that the uncertainty increases from the tip of the pyramid (definition of the base unit) to its base, which involves the actual measuring equipment.

1.1.3 Reliable

As explained in the previous section, the accuracy itself is not a quantitative value, but it is described quantitatively by the measuring uncertainty. Here the focus is on the methods used to assess the measuring uncertainty. The base principles of the uncertainty computation are described in the GUM (ISO/IEC Guide 98-3 – "Guide to the estimation of uncertainty in measurement")[5] but due to its complexity, the direction is towards more simplified approaches, which have been introduced for the implementation in the production environment. ISO 14253-2 [6] and ISO 15530-3 [7] are two examples. Moreover, in the philosophy of Industry 4.0, methods running automatically, are preferable: for example, methods using virtual replicate measurements based on Monte Carlo simulations. The reliability of the measuring instruments cannot ignore the component due to the software. Checking the mathematical algorithms and the underlying models used in the software utilized has become of fundamental importance.

1.1.4 Flexible

The term "flexibility" is explained as the capability of adaptation to changes in measurement tasks. This concept is intrinsically present in measuring technologies like computed tomography and 3D optical systems. 3D optical systems are also considered flexible systems, since they provide, in very short time, complete 3D digital models for the design of products, processes, quality control and production environments. Moreover, a more extensive use of simulation tools will be justified because it will allow operators to test and optimize the machine settings for the next product in the virtual world before the physical changeover, lowering the machine setup times and increasing quality.

1.1.5 Holistic

The term "holistic" refers to the complexity of the system. This means that the information about a product should be analysed together, without decomposing them according to their sources. Among the measuring techniques, computed tomography represents a good example of holistic system: it allows to obtain, in the same acquisition, data for dimensional verification and for density and porosity analysis, since it is capable of acquiring both, external shapes and internal feature of an object. Non-contact techniques (optical-based, x-ray based,..) are ever more used due to their good compromise between time needed and resolution, for both in-process measurements (the process is not stopped and the measuring process is carried out simultaneously) and on-machine measurements (the part is still placed on the machine tool, but the machining process is stopped)[8]. When the product shape is requested, the entire model is acquired and collected, differently from the typical coordinate measuring machines, which acquire surface data for each measurement characteristic (a length, a diameter) and not the entire model. This way, those kinds of instruments allow not only to detect defects but also to identify the root cause of the fault, through the full 3D comparison between the acquired point clouds and the CAD model. In this context, car manufacturers moved their attention from off-

line to in-line measurement in order to collect process data rather than product data, which allows them to extend quality control and process optimizing strategies[9].

1.2 Additive manufacturing techniques: a challenge for manufacturing metrology

It is important to highlight another aspect: the main challenges of industry 4.0 comprise the additive manufacturing technologies. The consolidation of these technologies, for example in the biomedical, as well as in the aeronautical field, poses the problem related to the dimensional verification of very complex geometries made of a large variety of materials, both polymers and metals. This challenge cannot be fully accomplished by the traditional coordinate measuring machines and many efforts have been carried out with the aim to make the optical and, more generically, non-contact measuring instruments, capable of fulfilling these tasks, without disregarding the importance of the "reliability" of these systems.

1.3 The role of close-range photogrammetry

Close-range photogrammetry is recognized as a simple, flexible, and effective methodology in shape detection and 3D measurement of components characterized by a prevailing dimension respect to the others (e.g., height is much higher than length or vice versa), complex free form geometry, and under-cuts. It shows great flexibility, where this term refers to the definition reported in the *section 1.1.4*, i.e. the capability of adaptation to changes in measurement tasks. Through the combination between rotation and translation of the sensor and the sample, the acquisition of very complex surfaces becomes possible. Moreover, it is able to provide accurate measurements and 3D photorealistic surface reconstructions in a simple and inexpensive way, as well as, in very short time (thanks to the computation of the texture).

For these reasons, it is fully embedded in the philosophy of Industry 4.0.

1.4 Conclusion

To summarize, Industry 4.0 concept applied to manufacturing metrology, consists of integrating the measuring technologies with components from information technology. This idea is embedded in the recent measuring instruments, such as coordinate metrology (contact and optical) or computed tomography. So that these measuring techniques are central in the context of Industry 4.0 and "Measurement Technology 4.0".

Chapter 2 - State of the art of non-contact measuring techniques

As underlined in the first chapter, the dimensional verification of industrial parts needs ever more performant measuring instruments in terms of time required and reliability of results, which have to be accompanied with a traceability statement. In the following sections, the techniques mostly adopted in the close and microscopic range will be described. The close range will be intended as the measurement of component with at least one critical dimension or a functional feature in the millimeter range. While, for micro range, the same definition could be applied, considering at least one critical dimension or functional feature in the micrometer range.

2.1 Introduction

Non-contact measuring instruments, which include optical-based or x-ray based systems are capable to acquire large amounts of points in a relatively short time, making these techniques widely used in industry [10,11]. Their usage depends on the dimensional range considered, the shape complexity and the material and surface [12]. In *Figure 3,* some of these techniques are reported, together with contact system, for an evaluation of their performance in respect to above mentioned factors, dimensions, shape complexity, material and surface, and, finally the their traceability assurance. Among the optical techniques, laser tracker are considered suitable for large and medium range, the fringe projection, which includes structured light scanners up to the micro range, interferometry is particularly suitable for small and micro range, together with confocal microscopy and the other optical profilometers. According to this research [12], photogrammetry is considered a valid technique up to the small range, with no application in the micro range.

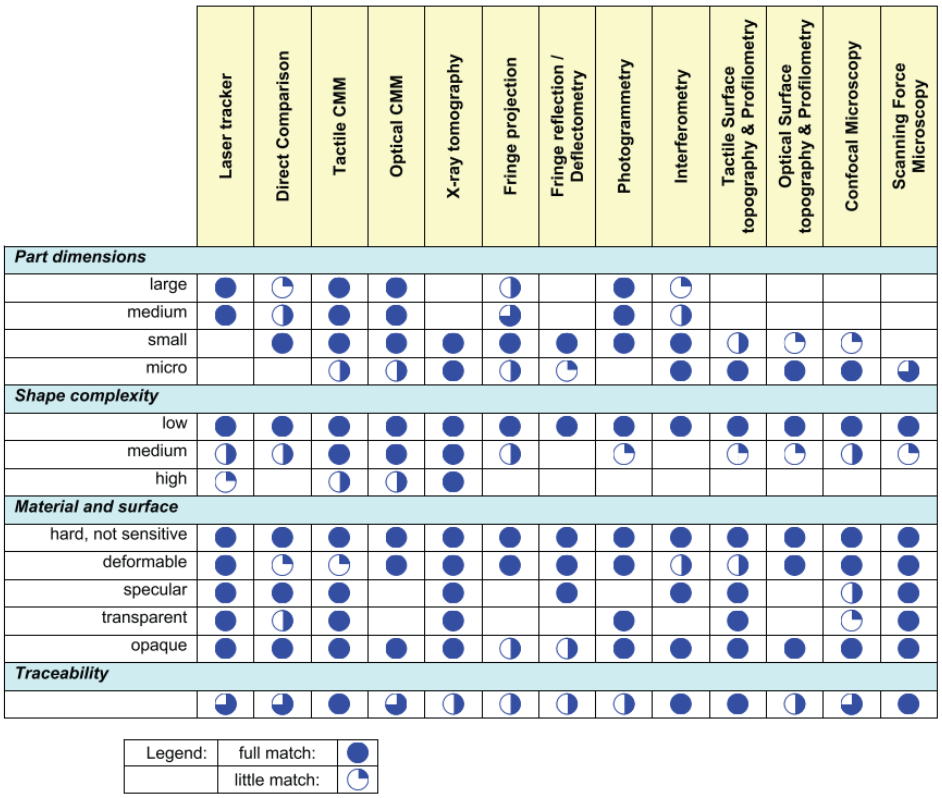

Figure 3 Evaluation of some measuring techniques with respect to the part dimensions, the shape complexity, material and surface and the traceability[12].

2.2 Close range non-contact measurement techniques

2.2.1 Optical-based techniques

In the close range, the most adopted optical measuring instruments are laser scanners, structured light scanners and photogrammetry. In [13] a comparison between different non-contact digitization techniques, comprising CT scanning, laser scanners and fringe projection methods is reported. Laser scanners are currently applied and cover most of dimensional ranges [14,15]. Laser scanners, in their several forms, through the well-known triangulation principle, see *Figure 4* (a), are commonly used for the inspection of machined surfaces with higher productivity. Because of their advantages, including the non-contact approach, speed, and high precision, the laser scanning method has been obtaining increasingly extensive applications[16]. Laser line scanners are often used in combination with contact probe CMMs [17–19] in order to exploit the different advantages that each of these sensors has. However, point cloud registration still represents a criticality and leads to a registration error, which cumulatively affects the final bias[20]. Laser-based scanners suitable for the close and small range are widely used for dental applications, in the form of extra-oral scanners.

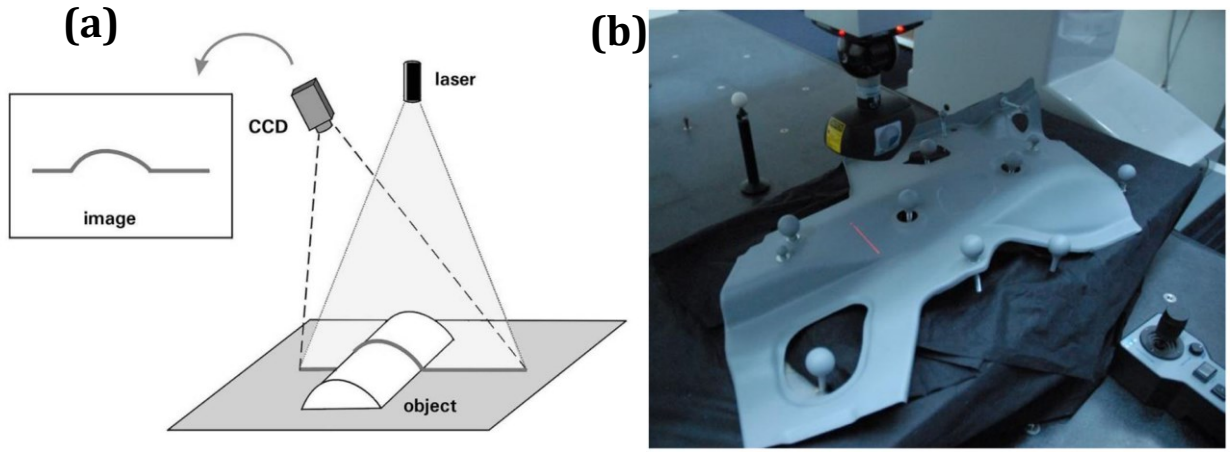

Figure 4 Working principle of a laser-based scanner [21]*(a); CMM equipped with a laser line scanner (b)* [19].

Structured light scanners are adopted as a consolidated technique in industrial metrology, and it is used in the small range for dental uses, for extra-oral and intra-oral scanners. As the laser based scanners, they exploit the triangulation principle, which can be obtained through a projector and two sensors, see *Figure 5* (a), or through a projector and one sensor Figure 5 (b). They feature several advantages: capability to acquire large amount of points in a short time, portability and high accuracy. Particularly relevant for this kind of instruments is the fringe projection mode. There are many approaches and an exhaustive overview is reported in [22]. Results reported on this research put emphasis on the shifting approaches, which allow to obtain dense reconstructions and high accuracy. However, they are only valid for static scenarios. Multi-phase shifting approach have been then introduced to reproduce parts in a moving scenario. The accuracy of those kind of instruments is strongly dependent on the calibration procedure [23], which is typically carried out with a calibrated plate and a calibration model. Calibration models usually adopted in 3D optical scanners field are those developed for photogrammetry and computer vision [24], but, in addition, for structured light scanners, information from structured illumination has to be considered [25]. A classification of this kind of instruments is based on the colour of structured light used for 3D scanning. It can be white or blue. White light scanning is ideal for scanning components, such as, sheet metal parts, tools and dies, turbine blades and moulded parts. However, structured blue light scanners present several benefits over structured white light ones, including the long-lasting light source, the increased portability of the equipment, the lower temperature influence due to the use of LEDs and the ability to scan inside a room while filtering out other light sources.

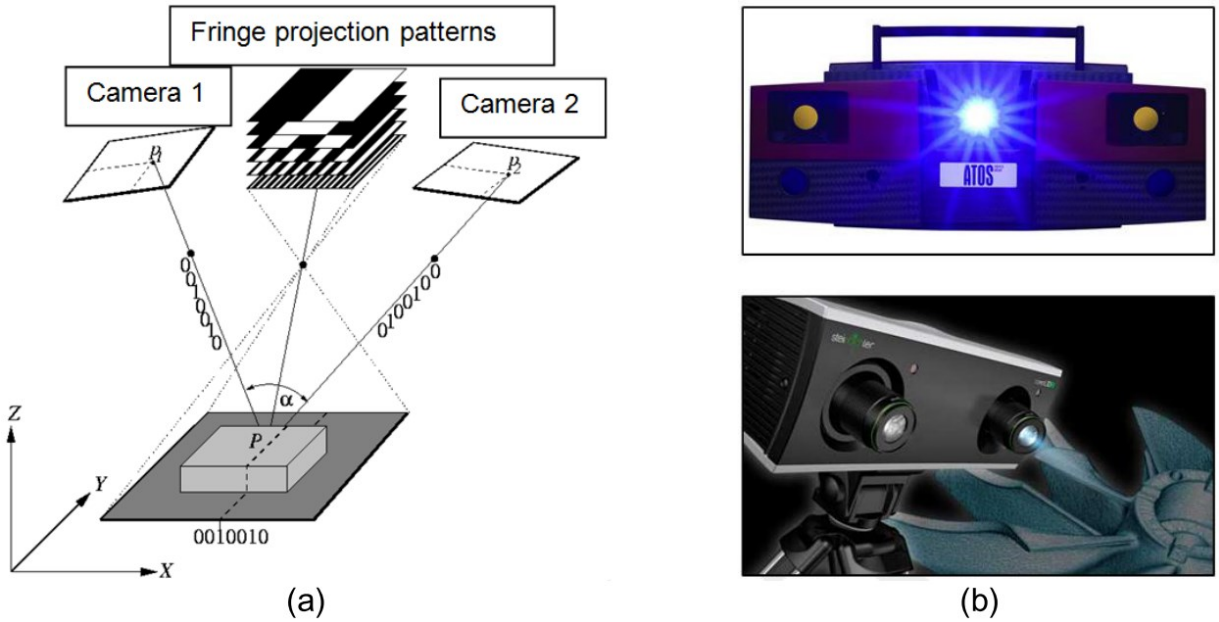

Figure 5 Basic working principle of structured light scanners (a), Sample structured light scanners (b)[21]

Photogrammetry, as well, is usually applied from large to close range [26–30].
Photogrammetry-based measurement derives 3D coordinates from images and tracking of cameras is not necessary, as camera positions and orientations are independently determined. Thus, for industrial application and on-machine verification it is possible to use several cameras in different fixed or flexible positions or, one camera mounted on a motorized structure, or integrated into a robotic machine tool, see *Figure 6*. Recently, a photogrammetry-based scanner was integrated in a robotic system for on machine verification purpose and a complete analysis of the main systematic error sources was carried out [31].

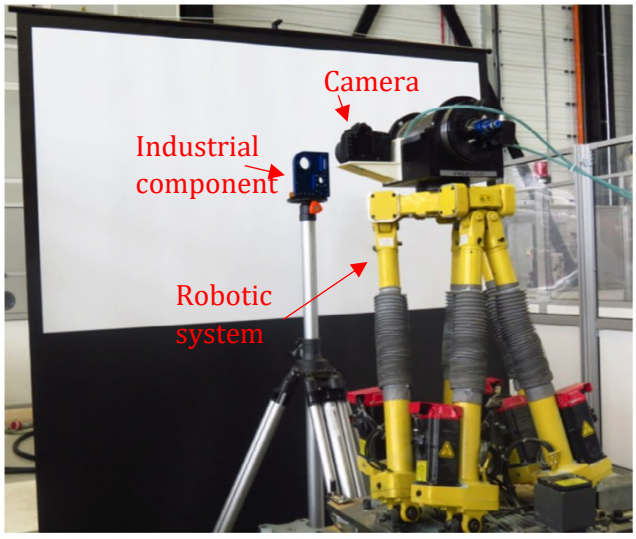

Figure 6 Example of photogrammetry integrated in a robotic system for on –machine verification [31].

Performance evaluations of 3D optical scanning systems refers to the VDI/VDE 2634 Part2 and Part 3, involving the usage of spheres and gauge blocks measured throughout the scanning volume. Some application of this guideline is reported in [32,33], however, this standard is better suited just for a first acceptance test because these geometries are not well-representative of the more complex industrial cases. Moreover, one of the biggest limit of the optical-based techniques

is their dependency on surface characteristics, in terms of colour, reflectivity and transparency [34,35].

2.2.2 x-ray-based techniques

Recently, Computed Tomography raised a lot of interest due to its several advantages, among which, the capability to reconstruct the internal features of a component. The basic element of a computed tomography scanner is the x-ray source. The x-rays emitted are attenuated due to absorption or scattering, as they propagate through the workpiece material. The amount of attenuation is determined by the material composition and its density and by the energy of the X-rays. The attenuation is measured by capturing the remaining X-rays that traverse the workpiece by means of an X-ray detector, resulting in a 2D gray image, in case of a flat panel detector or a 1D gray profile, in case of a 1D line detector [36]. Images are taken from different angular positions of the workpiece, see *Figure 7*.

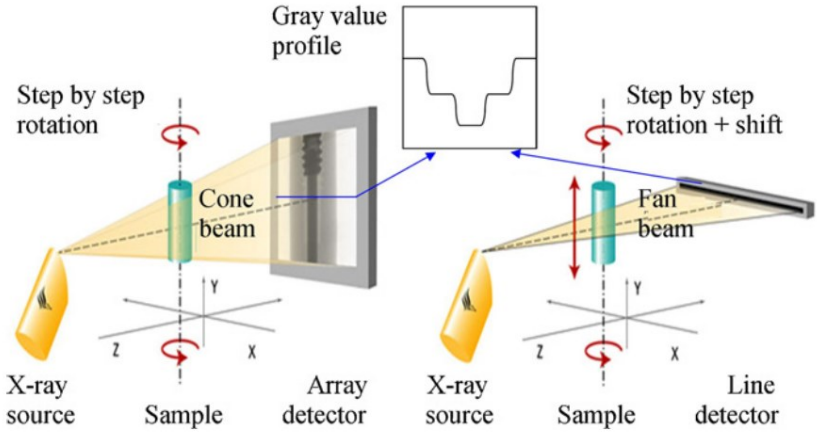

Figure 7 2D flat panel detector with cone beam and 1D line detector with fan beam [36].

This characteristic, which is unique among the overall measuring instruments currently available, made CT a suitable instrument for several dimensional verification purposes in the industrial field [37]. For example, the verification of machined parts with internal features like small or long channels, or to check the presence of burrs and intersecting holes, as well as, the verification of injection moulded polymeric parts, thanks to the good x-ray penetrability of these materials and, finally, the additive manufactured components. The latter are particularly interesting not just for a dimensional quality control of complex parts (e.g. hidden cavities or lattice structures) but also for a non-destructive density-porosity verification, which represents a fundamental issue in AM processes, see *Figure 8*, [38], as well as, in metal forming processes[39]. In this context, and at the time being, this is the only technique capable to carry out, contemporary, a dimensional verification and a material quality checking without destroying the sample. Moreover, differently from optical based systems, CT scanners are not sensitive to the surface texture and colours, but material density has to be considered [40,41].Recently, experimental applications of CT increased. In [42] CT was used as reverse engineering technique for the reconstruction of turbine blades external shape, as well as, the internal channels. From the traceability point of view, which remains a critical issue for the CT, many efforts have been carried out. The currently available German standard for CT system is

described in the VDI/VDE 2617-13 but it does not provide a standardized procedure to ensure traceability of measures. With the aim to find new procedures, many studies were conducted to investigate the main factors affecting the process and several reference objects have been designed and adopted. In [43] a step gauge, a cylindrical step gauge, a multi-material cylindrical assembly, a threaded tube for medical application and a LEGO brick were proposed. Each reference object is developed depending on its purpose to correct for different biases, e.g. those due to image artefacts, scale errors, CT system limits and data evaluation strategy. In [44,45] a CT crown and a CT tube were designed and measured for an on line calibration procedure, with the double purpose of scale adjustment and measurement traceability assurance.

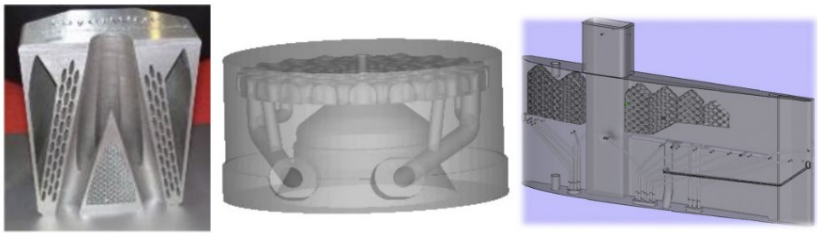

Figure 8 Examples of AM parts with internal features and lattice structures [37].

2.3 Measurement of micro-components

Micro-manufacturing is a crucial part of the trend towards the miniaturization of products and components, which has involved most of the industrial sectors during the last decades. In [46] the first definition of Micro Engineering was reported *"Micro engineering deals with development and manufacture of products, whose functional features or at least one dimension are in the order of µm".* In particular, it encompassed most of the already existing manufacturing techniques, from cutting technologies to injection moulding passing through the Electro Discharge Machining [47–49]. The same tendency is registered for additive manufacturing technologies [50]. In *Figure 9*, some example of micro-components are reported.

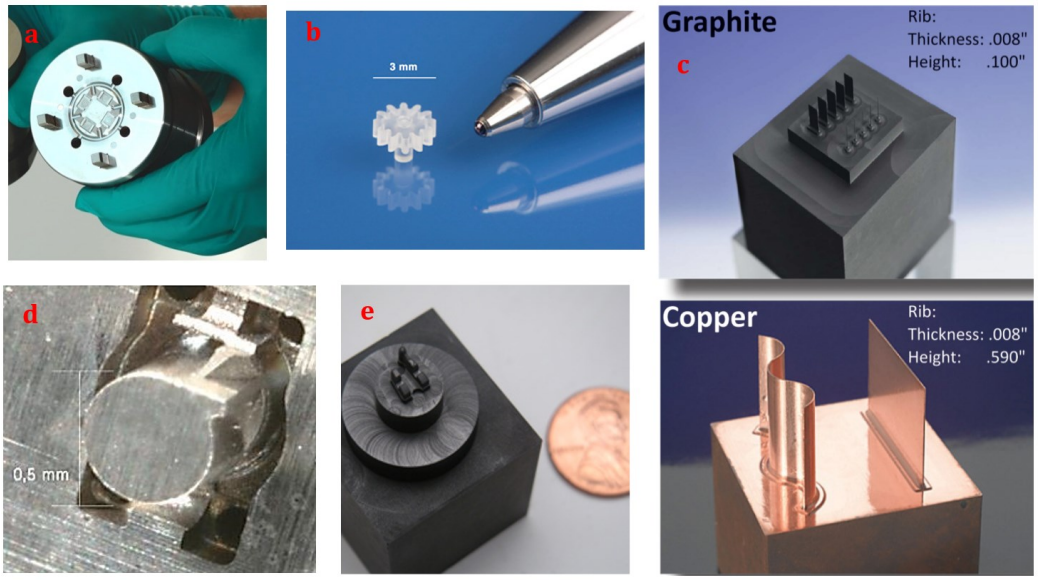

Figure 9 Example of micro-components: mould for injection moulding (a), injection moulded part (b), electrodes for µEDM (c) (e), micro-mould for casting (d).

Concomitantly with the development of the micro-manufacturing, the need for measuring systems capable of conducting the dimensional verification, as well as, the surface analysis of these micro-products or components arose, see *Figure 10*, [51,52]. Contact measuring instruments, in the form of Coordinate Measuring Machines (CMMs), considered the most reliable systems in dimensional metrology, were developed also in the micro range, thanks to the miniaturization of the stylus [53]. Although, these technologies are expensive and involve relatively long scanning times. Moreover, as approaching the close range and micro-nano-range other problems come out: accessibility and minimum measurable feature size due to the probe and stylus dimensions, measuring point density, measuring time, deformation of high aspect ratio structures under measurement and of soft substrate materials due to the probing force.

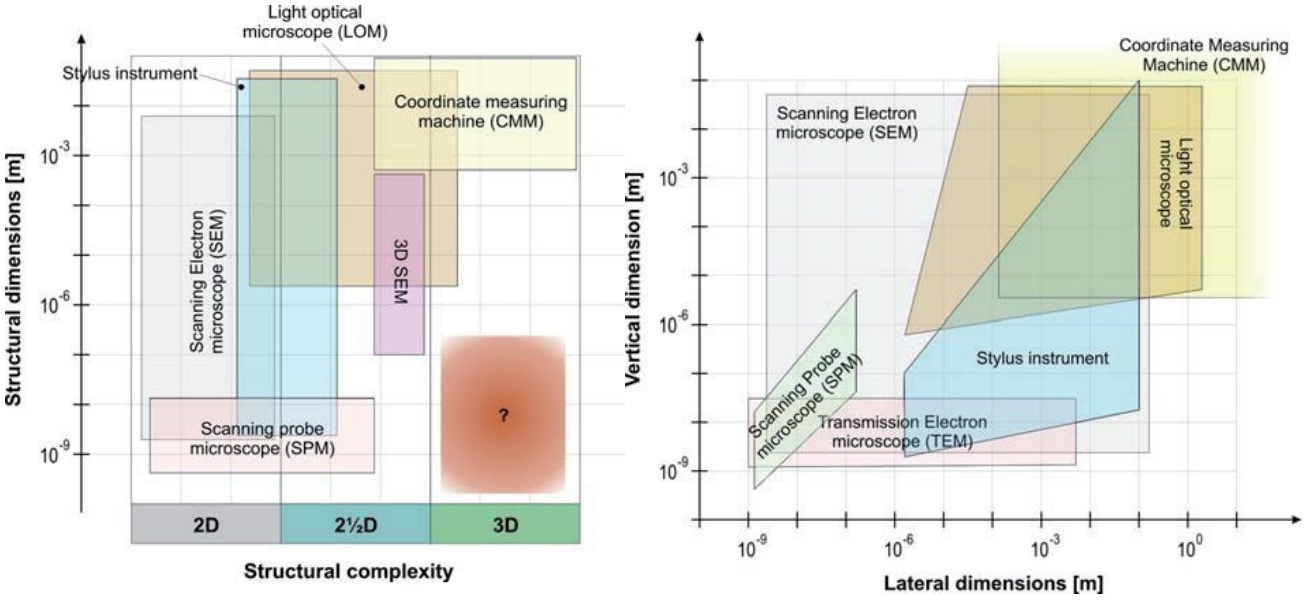

Figure 10 Classification of measuring techniques adopted according to the structural and vertical resolution needed [52].

The last issue is enhanced by the large variety of polymeric materials currently used in micro manufacturing. Among optical-based techniques, a possible classification is made according to the number of dimensions that can be measured simultaneously by the sensor itself [54]. Conoscopic holography [55,56], used as surface digitizing technique, is considered a 1D technique and it requires at least two moving axis to ensure a 3D reconstruction. White light interferometry [57] and confocal microscopy [58] are comprised in 2D measuring techniques and they require at least one mechanical axis for a 3D reconstruction. However, they present limitations when used for the measurement of micro-parts characterized by complex geometry and having surfaces with inclinations near to 90°. More innovative non-contact measurement instruments, which have been recently developed, are the 3D SEM (Scanning Electron Microscope) microscopy [59] and the micro-CT (scanning with computed tomography) [60]. To reach the third dimension, both integrate the reconstruction technique of stereo-photogrammetry, with the technology of scanning electron microscope and computed tomography, respectively. Especially the latter, micro CT, is arousing a lot of interest due to its capability to provide a densely populated point cloud of an object, allowing the measurements of both external and non-accessible internal structures, features, and multi-material components without the need for external access or destructive testing. For these reasons, lots

of efforts have been doing to provide a quality assessment [61]. Those non-contact systems present many advantages, such as the ability to capture small geometries and complex shapes as well as the high number of points acquired. Additionally, the portability of non-contact sensors, make them easy to install on different equipment such as coordinate measuring machines (CMM), articulated arm coordinate measuring machines, even in a production environment. Moreover, it is important to underline that confocal microscopy, interferometry and focus variation, allow to have contemporary dimensional data and surface texture data, if the proper magnification level is selected. However, despite their undoubted advantages, commercial non-contact scanners are considered less accurate than the traditional contact-type methods, since their accuracy depends strongly on the relative position and orientation of the sensor respect to the sample, the configuration parameters of the sensor, the geometry of the sample, the optical properties of material, as well as the surface roughness.

2.3.1 Photogrammetry applied to close and microscopic range

Photogrammetry was usually applied to large scale metrology [62] and more recently to close range [26], while there are still few applications of photogrammetry in micro-range. Small objects, with sub-millimeter or micrometer feature, need to be acquired with high magnification level and a micrometer resolution. There are several solutions proposed to ensure magnification levels higher than 1x or 2x, such as zoom lenses, macro lenses [63,64] or lenses with extension tubes [65]. Although, there are some important issues to be managed. Zoom lenses are mainly affected by the instability of camera calibration [66], while macro-lenses have the ability to capture a sharp image of a small object with a short working distance, retaining good stability in camera calibration. In macro-lens photogrammetry, the limited depth of field leads to the impossibility to have the entire image in focus when the lens is very close to the object. This issue can be overcome if many pictures are acquired at different distances, covering the entire object, but with the consequence of high CPU processing times. To solve this limitation, in [67] the use of focus stacking in combination with photogrammetry was proposed, i.e. using commercial software to create single, completely focused images, from several partially focused images, by combining the focused areas. Then, the completely focused images are used to perform photogrammetric computations (*Figure 11*) [67].

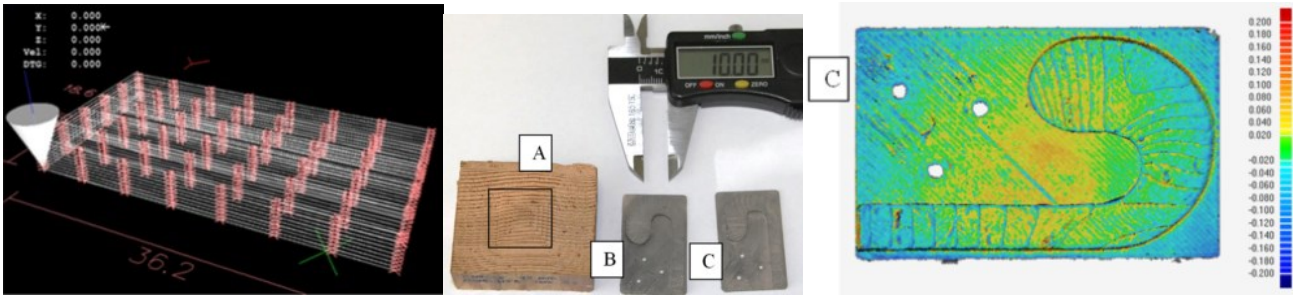

Figure 11 Example of photogrammetric mapping of samples (18.6 mm x 36.2 mm) and coloured maps describing their deviations from the reference model [67].

In [68] a multi-view passive stereo technique was used, as well, for the 3D reconstruction of small sized objects based on a sequence of macro images and an image fusion algorithm was implemented to extend the depth of field of the images used in the photogrammetric process.

Another method is the use of tilt-shift lenses, which represents a way for controlling and adapting the DoF (depth of field) to the scene of interest, using the so-called camera movements (tilt and shift) [69].
Recently, the usage of extension tubes [70] instead of macro-lenses was presented. This solution is well suited for automated and versatile scanning systems, see *Figure 12*.

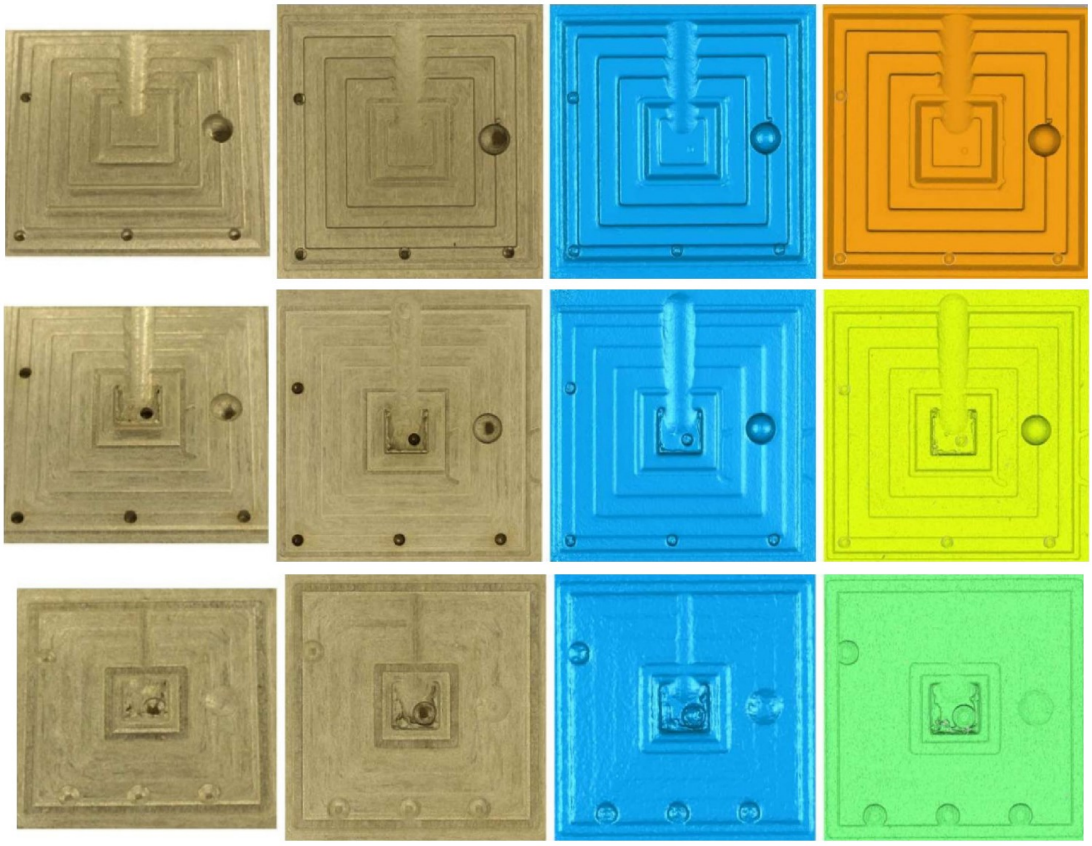

Figure 12 Examples of aluminium samples, with sub-millemeter sized feature acquired, with the use of extension tubes [65].

Depending on the size of the object, it is possible to increase or restrict the field of view (move away or move closer the camera from the object) just choosing a different extension tube length. In order to get the object in focus, the focus distance of the lens mounted on the extension tube is normally set to infinity, thus it is necessary to operate with a fixed distance from the object, which is unique and depends from the particular coupling of the lens/extension tube length. This criterion allows to get photographs with negligible distortion, and therefore greater precision in reconstructing the 3D digital model, even without a previous internal camera calibration, since the camera lenses are manufactured with the aim to minimize the distortions in the image when focuses to infinity. Extension tubes have been also adopted in conjunction with macro-lenses [71], see *Figure 13*.

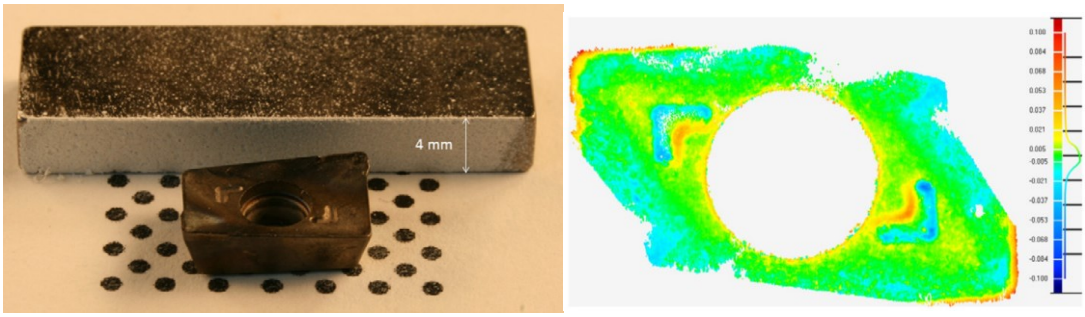

Figure 13 An application of macro lenses equipped with extension tubes: the tool insert [72].

Chapter 3 - State of the art of the International Standards

International standards represent the main tool for communicating in a global economy. In the context of measuring systems, among other things, they regulate the relation between manufacturers of those systems and customers especially in a global commercial context. The measurement limits and characteristics, such as accuracy, precision, as well as, resolution of a system should be obtained using standardized methods so that the manufacturer can provide specifications meaning something to the customer.
Even though, 3D optical scanning systems have been developed and used for a few decades, they are still considered to be an emerging technology.

3.1 Performance verification and testing of optical instruments

Performance verification tests are widely used as acceptance testing for optical 3D imaging systems [73]. Acceptance and reverification tests are fundamental for manufacturers (acceptance) and users (reverification) for:

1) proving the applicability of a given system to the task (fitness-for purpose);
2) comparing different instruments using proper methodologies and metrics;
3) managing instrument warranty issues;
4) reducing costs through effective use of 3D imaging systems;

The quality parameters for the acceptance tests are clearly defined in terms of recommended artefacts, the procedure, the method to calculate the results, and their interpretation. The reverification of the optical 3D measuring systems ensures long-term compliance with limits specified by the user and it allows to detect trends for preventive maintenance. With these purposes, physical standards, along with the different tests methods, are used to characterize 3D optical imaging systems, see *Figure 14*.

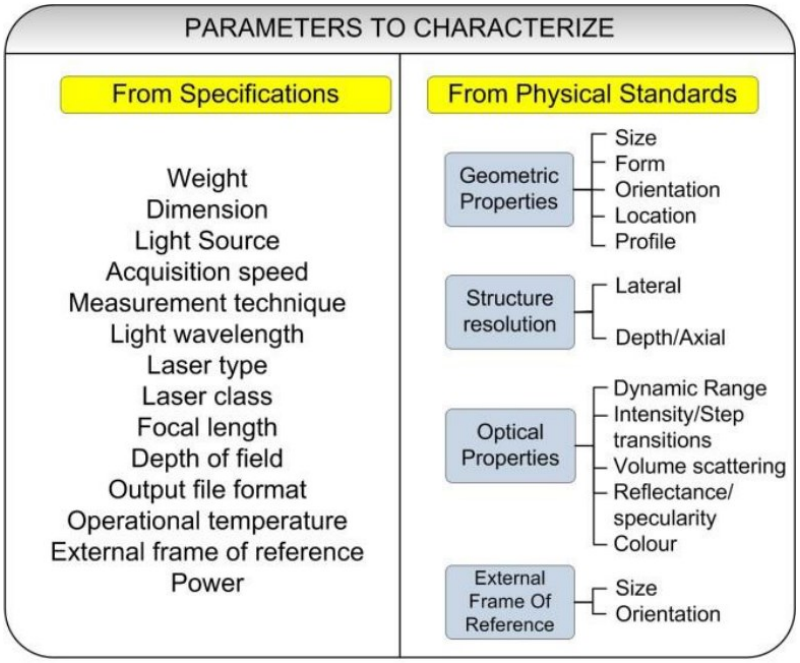

Figure 14 Parameters, which need characterization [73].

The ISO standards on performance verification are recent: ISO 10360-7 [74], ISO 10360-8 [75]. The ISO 10360-7 deals with CMM equipped with imaging probing systems, while the part 8 deals with CMM equipped with optical distance sensors.
The German VDI/VDE has been very active in defining standards for coordinate metrology and, in particular, for coordinate measuring machines (CMMs) equipped with optical probing and, more importantly, for stand-alone 3D optical measuring systems.

- VDI/VDE 2617 Part 6.2 (2005) – Guideline for the application of ISO 10360 to coordinate measuring machines with optical distance sensors;
- VDI/VDE 2634 Part 2 (2012) – Optical 3-D measuring systems: Optical systems based on area scanning;
- VDI/VDE 2634 Part 3 (2008) – Optical 3-D measuring systems: Optical systems based on area scanning in several single images.

The VDI/VDE 2617-Part 6.2 [76] proposes a revision to the ISO 10360-2 tests [17] specific for coordinate measuring machines equipped with an optical distance sensor (ODS), which could be both triangulation and interferometry-based optical sensors. The VDI/VDE 2634 series closely follows the recommendations of the VDI/VDE 2617 but the optical measuring systems can be mobile and considered as standing alone.
Part 2 and Part 3 of the VDI/VDE 2634 [77,78]are important to manufacturers and users for verifying systems compliance with required performance specifications. This is realized through acceptance tests performed by the manufacturers and verification tests performed by the users. Part 2 include single-view optical systems based on area scanning and Part 3, multiple-view systems. Area scanning is based on triangulation methods, which include fringe projection, moiré techniques, and photogrammetry or scanning systems with area-based measuring capabilities. The parameters, listed in *Figure 15*, are usually computed on a single point cloud or multi-view registered point clouds; however, not all 3D imaging systems provide data in that format. For this reason, the possibility to use polygonised or triangulated data files is discussed in the VDI\VDE 2634. Filtering and pre-processing of the measured values are allowed only if

they are part of the boundary conditions or it is a routine operation of the system's software procedure.

VDI\VDE 2634 **Part 3**

Symbol	Description
Characteristics	
F_D	Plane-spacing error
SD	Sphere-spacing error
P_F	Probing error (form)
P_S	Probing error (size)
E	Length measurement error
Limit value	
MPE_{XX}	Limit value for quality parameter XX (maximum permissible error) e.g. MPE_{PS} is the limit value for P_S
Auxiliary quantities	
D_a	Measured diameter of test sphere
D_r	Calibrated diameter of test sphere
L_{ka}	Measured sphere spacing
L_{kr}	Calibrated sphere spacing
L_a	Measured value of the test length
L_r	Calibrated value of the test length
L_O	Spatial diagonal of the measuring volume specified by the manufacturer
L_S	Spatial diagonal of the sensor measuring volume specified by the manufacturer
E_E	Length measurement error on short gauge block

VDI\VDE 2634 **Part2**

Symbol	Description
Characteristics	
F	Flatness measurement error
P_F	Probing error (form)
P_S	Probing error (size)
SD	Sphere-spacing error
Limit value	
$Y_{X,MPE}$	Limit value for parameter Y_X (maximum permissible error) e.g. $P_{S,MPE}$ is the limit value for the probing error P_S
Auxiliary quantities	
D_P	Dimension of the artefact
L_O	Body diagonal of the measuring volume specified by the manufacturer
L_a	Measured value of the test length
L_r	Calibrated value of the test length
L_P	Dimension of the artefact

Figure 15 Symbols used in the VDI|VDE 2643 Part 2 and Part 3.

3.1.1 VDI 2634 Part 2 – Optical 3D measuring systems based on area scanning

Part 2 include single-view optical systems based on area scanning. The main characteristics for the performance tests are listed in *Figure 15*. The probing error attempts to evaluate the intrinsic properties of a 3D imaging system, evaluated within a small portion of the measuring volume. It is expressed in terms of form (P_F) and size (P_S). Using a sphere of a given dimension, form is given by the range of radial distance between the measured points and a best-fit sphere. The fit is performed according to the least-squares method. The size is the difference between the measured and calibrated diameter of the sphere. The sphere has to be measured in at least ten positions within the working volume (*Figure 16*, a) and the specification of the probing error is fulfilled only if the computed values of the quality parameters are within the limits requested by the manufacturer, see Eq. (3.1) and (3.2).

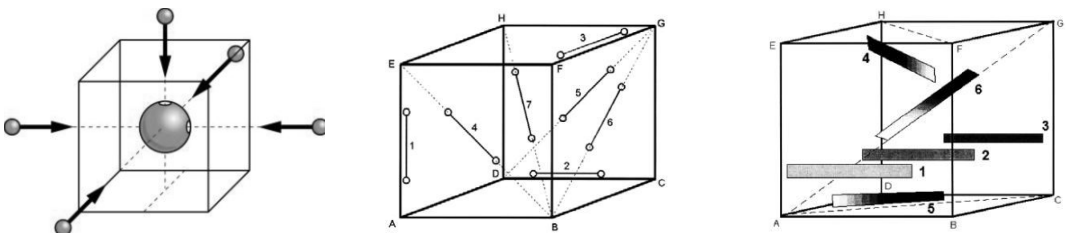

a **b** **c**

Figure 16 Probing error test (a) Sphere spacing quality parameters (b) Flatness quality parameters (c)

$$|P_X| \leq \left|P_{X,MPE}\right| - U \quad \text{for the manufacturer} \qquad (3.1)$$

$$|P_X| \leq |P_{X,MPE}| + U \qquad \text{for the user} \qquad (3.2)$$

In eq. (3.3) The expanded uncertainty computed according to the ISO 14253-2 [6] is reported, where W is the quality parameter (P or F) and Form is the form deviation of the artefact, i.e. either a sphere or flat plane.

$$U(W) = \sqrt{\left(\frac{Form}{2}\right)^2 + U^2(Form)} \qquad (3.3)$$

The sphere-spacing error, SD, is the difference between the measured and the calibrated values of the distance between the centres of two spheres. It aims to verify the length-measuring capability of the system and to ensure traceability. For the purpose, a ball bar, or simply two spheres, at a fixed and calibrated distance from each other can be used. The artefact dimensions, length L_P and diameter D_P, are specified as function of the measuring volume, L_O. Seven positions within the measurement volume are recommended for the artefact, see *Figure 16*, b. The basic equation for the expanded test uncertainty U in the case of SD is reported in Eq. (3.4).

$$U(SD) = \sqrt{\sum_i U^2(\varepsilon_i)} \qquad (3.4)$$

Where, ε_i represents each uncertainty component included in the uncertainty budget according to the ISO 14253-2.

Finally, the flatness measurement error, F, is the range of the signed distances of the measured points from the best-fit plane calculated using the least-squares method. The artefact is a parallelepiped with the width of, at least, 50 mm and the length function of the working volume size, no less than $0.5 \times L_O$. The flatness value must not affect the parameter under evaluation and its value must be declared in a calibration certificate. No less than six different orientations of the artefact should be considered, *Figure 16* (c).

3.1.2 VDI 2634 Part 3 – Optical 3D measuring system based on multiple views

The VDI/VDE 2634 Part 3 applies to 3D optical measuring systems based on multiple views or multiple images (3D) generated by re-positioning the sensor and/or the object to be measured. These 3D images are registered together in a common Cartesian coordinate system using reference coded or uncoded markers (e.g. contrast targets) or the actual shape of the object through the ICP (Iterative Closest Point) algorithm. If compared to the Part 2, it extends the acceptance testing and reverification to the effect of re-positioning of the sensor and/or the object. Generally, a single 3D image sees a volume smaller than the whole system measuring volume.

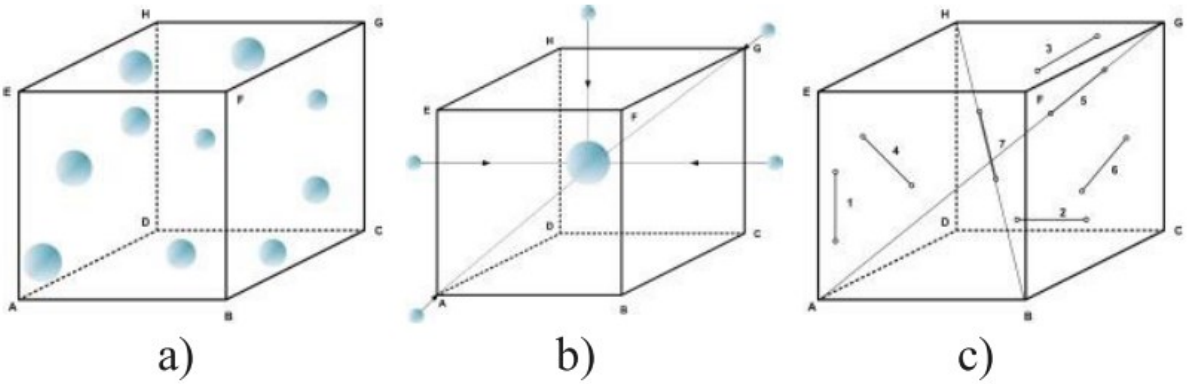

Figure 17 Location of an artefact according to VDI/VDE 2634 Part 3, a) example of ten locations for the test sphere, b) example of measurement directions of the sensor relative to the test sphere, c) recommended arrangement of artefacts when determining the sphere-spacing error[73] .

The probing error, in terms of P_F and P_S, consists of two influence factors, differently from the Part 2: errors of a single 3D image, as described in Part 2, and the errors due to the registration and transformation of the different 3D images in a unique coordinate system. The test sphere is measured in at least three randomly distributed positions within the measuring volume (*Figure 17*, a). In each position, the sphere must be measured from at least five sensor positions in order to capture the surface in a complete way (*Figure 17*, b). The evaluation and assessment is performed in a manner similar to Part 2 and both, form and size, describe the quality parameters. The sphere-spacing error, SD, is used to test the capability of the system of performing length measurements from multiple views. The length artefact is composed of two spheres, (a ball bar or two spheres with a calibrated distance) and needs to cover a large section of the measuring volume. SD is defined as reported in Part 2, but, differently from part 2, the quality parameter length measurement error, E, has to be added. It is computed using ball bars, gauge blocks, step gauges or ball plates in order to investigate the performance of the system throughout the working volume.

3.1.3 Physical standards

As previously described, the international standards ISO 10360 series and the German guideline VDI/VDE 2634 require only basic shapes, i.e., spheres and planes. The physical standards must be measurable and they are chosen for their physical and optical qualities, since optical instruments are more or less sensitive to a specific surface characteristic depending on their measurement principles. For example, interferometry-based and confocal-based are capable of measuring opaque, transparent and translucent materials, while triangulation-based techniques require reference artefacts with cooperative optical surface characteristics (Lambertian reflectance), such as negligible volume scattering (the optical and mechanical surface should coincide) and colour compatible with the light source. For these reasons, metallic surfaces are sometimes treated to make them diffusely reflecting. Some surface treatments, like vapour blasting, light particle blasting, or spray particle coating are able to change a specular surface into a diffusely-reflecting surface.
The required reference objects (see *Figure 18*) used for acceptance and reverification test are, then:

- **Spheres** with certified form and diameter values to determine form and size error;

- **A flat plane** is used for flatness measurement and as an alternative to the sphere form error test. The flat plate can be a machined or lapped plate, a 1-2-3 steel block, a 4-ways parallel block, an optical flat, a quartz block with chrome oxide deposition or any flat surface that is certified with a flatness characteristic.
- Length Measurement Error s determined using:
    - **Two spheres** mounted on a rigid axis: the accuracy of a 3D digitizer is evaluated using a two spheres centres distance test using a ball bar, or simply two spheres that are at a fixed and calibrated distance from each other;
    - **Two parallel faces** mounted in a rigid manner: An important way of finding the distance error between spheres is to evaluate the distance between two parallel flat surfaces, such as the two faces of a gauge block;

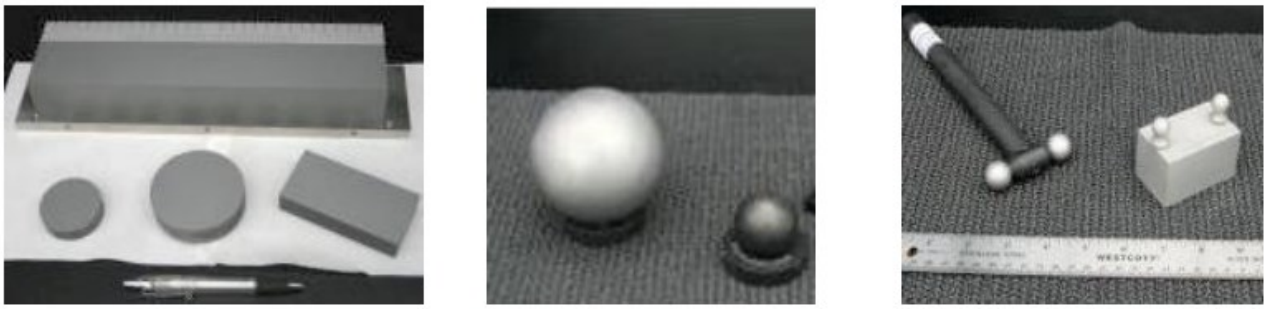

Figure 18 Reference objects used for the acceptance test. Gauge blocks, spheres and ball bars.

Although, these geometries are not well representative of the geometrical complexity of the real industrial cases. With the aim to cover most of criticalities related to 3D optical instruments when measuring complex artefacts, other reference objects have been designed. Among them, the NPL developed a new free-form calibrator geometry [79] specifically thought for 3D optical measuring instruments (*Figure 19*).

Figure 19 Photograph and schematic representation of NPL freeform artefact [79]

In [35] four artefacts have been designed and presented to aid understanding of 3D optical scanner main factors. Resolution, orientation, illumination effect, sensitivity to surface colour, material and finish.

3.2 Uncertainty assessment of a 3D optical-based system

With the aim to fully characterize a measurement carried out with an optical based system, as for every other measuring instrument, the uncertainty assessment has to be reported together with the measured values. Although, quantifying the uncertainty associated to an optical-based system is not a trivial task and, in the following sections, two main approaches are reported. First of all, a specific procedure for the uncertainty computation of a 3D optical scanner does not exist

and it is due to the complexity of those systems. If on one hand they allow to conduct very tough measuring tasks, on the other hand, there are many sources of error affecting these systems. Generally, the base guideline for the uncertainty assessment is the GUM approach (ISO/IEC Guide 98-3 – "Guide to the estimation of uncertainty in measurement") however, this approach often results to be hard and not easily implementable in a production environment. Starting from this fundamental guideline, other method for the uncertainty assessment have been developed. In particular, the ISO 14253-2 [6] is a guidance for the estimation of the uncertainty in the geometrical product specification field (GPS) and comprises methods for calibration of measuring equipment and for product verification (*section 3.2.1)*. Generally, in the field of dimensional verification, most of these standards were developed for CMMs and, in particular, a well-known method, widely used in the production environment is the substitution method explained in the ISO 15530-3 [7] and discussed in *section 3.2.2*. It transfers traceability from a calibrated reference object to an actual part and it is considered also a good method for assessing the uncertainty of an optical based system related to a specific task and to specific conditions. Indeed, due to the great flexibility of optical systems, it is almost impossible to calibrate them for all measuring tasks and a correct approach could be to calibrate it for each measuring task, under specified measuring conditions. Although, even if the ISO 15530-3 seems to fit the needs of optical based systems, the uncertainty assessment, currently implemented in that standard and used for contact probing systems, cannot be directly applied to optical-based instruments due to the necessity to add other error sources. In particular, for the ISO 15530, the similarity requirements must be satisfied not just as similar dimensions or form error or material, but also surface finishing, colour and the same optical characteristics [80]. In *Figure 20*, typical error sources for a 3D optical-based instrument are reported in the form of an Ishikawa diagram. Differently from contact instruments, there are other factors affecting the measurement:

- Lens distortion and aberration;
- Algorithms for reconstruction;
- Algorithms for point clouds and mesh managing;
- Algorithms for analysis;
- Interaction with the object surface;
- Interaction with the environmental conditions.

Among them, the interaction between the measuring system and the object is of paramount importance. The optical properties of the object, transparency, translucency and reflectivity play a fundamental role. There is a distinction between cooperative and non-cooperative surfaces. Generally, the latter produce large measurement errors undermining the application of those systems.

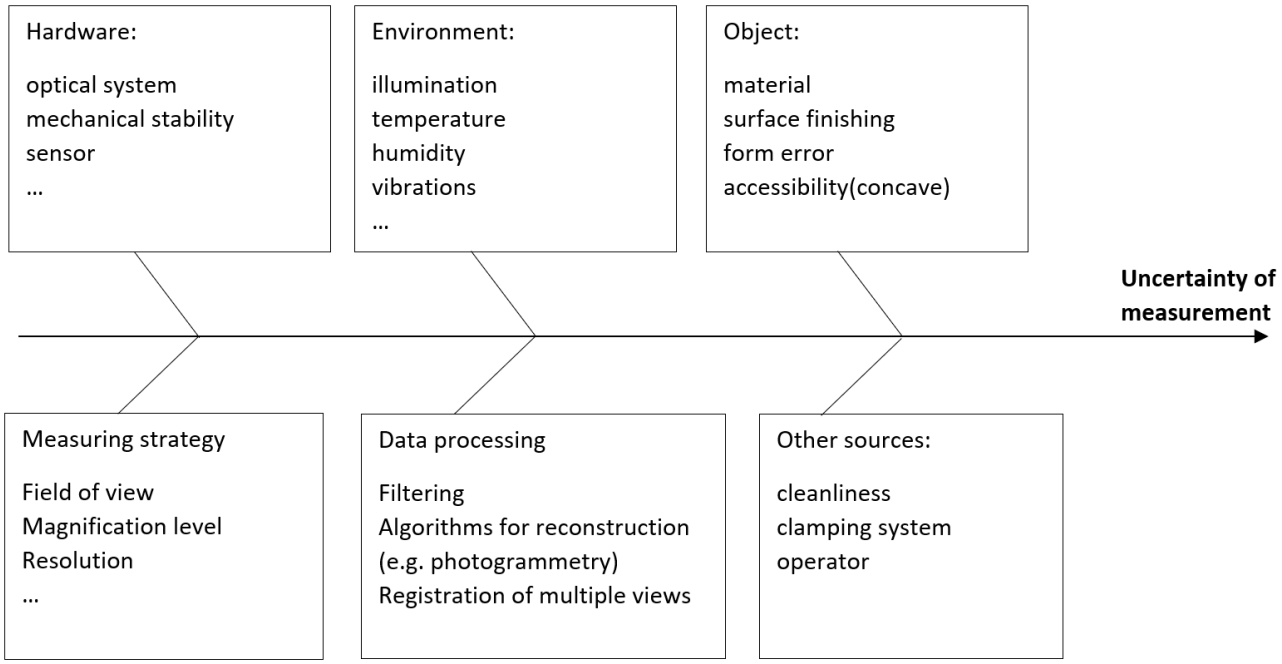

Figure 20 Typical error sources for a 3D optical-based instrument[54].

3.2.1 ISO 14253-2:2011 "Geometrical product specifications (GPS) -- Inspection by measurement of workpieces and measuring equipment -- Part 2: Guidance for the estimation of uncertainty in GPS measurement, in calibration of measuring equipment and in product verification"

The ISO 14253 part 2, introduces a guideline for the uncertainty assessment, which encompasses the GUM (ISO/IEC Guide 98-3 – "Guide to the estimation of uncertainty in measurement") and it is an iterative procedure with a value of target uncertainty (PUMA method). It is well suited for the industrial environment, to reduce time, risks and costs. The method for the uncertainty computation, proposed in this standard, comprises all the possible sources of error of a measuring system and each sources of error, which produces an uncertainty component, is considered in the uncertainty budget and computed according to the GUM. The latter [5] comprises type A and type B uncertainty components, depending on the method used for their computation, statistical method, type A, or non-statistical method, type B. The approach described in the ISO 14253-2 is defined as an upper-bound model, due to the natural overestimation of the resulting uncertainty and it is a precautionary measure in order to avoid wrong decisions based on measuring results. The assumption, which makes this method a simplified method, if compared to the GUM, is that all the uncertainty components are uncorrelated and, then, the total expanded uncertainty is the result of the root sum squared of the uncertainty components. The iterative procedure starts from a first rough estimation of the uncertainty (mainly composed by type B uncertainty components, which usually overestimates the amount of uncertainty) and then, the resulting value is compared with the target uncertainty. If the value obtained is less or equal to the target value, then it is acceptable and the iterative procedure can stop. Otherwise, a way to reduce the overestimation of uncertainty has to be found, e.g. considering type A components instead of type B components. The iterative procedure goes on until reaching an acceptable value and, in case it is not possible, the measuring

procedure has to be changed, somehow. The general equation for the combined uncertainty computed according to the ISO 14253-2, is reported below, Eq. (3.5).

$$u_c = \sqrt{u_{MPEx}^2 + \ldots + u_{Mx}^2 + \ldots + u_{Bx}^2 + \ldots + u_{Ox}^2 + \ldots + u_{Ex}^2 + \ldots} \quad (3.5)$$

$$U = u_c * k \ (k = 2) \quad (3.6)$$

Where:

MPEx refers to the uncertainty components related to the measuring equipment;

Mx refers to the uncertainty components related to the environment;

Bx refers to the uncertainty components related to the operator/s;

Ox refers to the uncertainty components related to the measurement set-up;

Ex refers to the uncertainty components related to the measurement object.

3.2.2 ISO 15530-3:2011 "Geometrical product specifications (GPS) -- Coordinate measuring machines (CMM): Technique for determining the uncertainty of measurement -- Part 3: Use of calibrated workpieces or measurement standards"

The ISO 15530-3 is addressed to CMMs and describes a simplified method for the computation of the uncertainty. It is thought for the application in the industrial environment and it implements the substitution approach. The basic concept is the transfer of the traceability from an artefact with known uncertainty to an actual artefact with unknown uncertainty, under some specific conditions and assumptions, which are identified as similarity conditions. Similarity shall include, similarity of the two artefacts (calibrated and actual) in terms of material, mechanical properties and thermal expansion coefficient, as well as, the identical measuring equipment and procedure and, finally, the environmental conditions. All the variations respect to the similarity requirements must be taken into account in the total uncertainty. The base equation is reported in Eq. (3.7).

$$U = k \times \sqrt{u_{cal}^2 + u_b^2 + u_p^2 + u_w^2} \quad (3.7)$$

$\mathbf{u_{cal}}$ is the standard uncertainty of the calibrated artefact;

$\mathbf{u_b}$ is the standard uncertainty of the systematic errors;

$\mathbf{u_p}$ is the standard uncertainty of the measuring procedure;

$\mathbf{u_w}$ is the uncertainty due to the variations of the uncalibrated artefact, considering variations of the mechanical properties $\mathbf{u_{wp}}$, as well as, variations of the CTE (coefficient of thermal expansion), $\mathbf{u_{wt}}$.

For the computation of the expanded uncertainty U, a coverage factor, k=2 is suggested, which means a confidence level of 95%.
Each uncertainty component is treated according to the GUM (ISO/IEC Guide 98-3 – "Guide to the estimation of uncertainty in measurement") and classified as type A and B.
The uncertainty due to the measuring procedure is computed as reported in Eq. (3.8).

$$u_p = \sqrt{\frac{1}{n-1}\sum_{i=1}^{n}(y_i - \bar{y})^2} \qquad (3.8)$$

Where, n is the sample dimension, y_i is the measured value of the measurand and y the average value computed over n repetitions.
In order to obtain a sufficient amount of data, at least 20 repetitions have to be conducted.

Chapter 4 - Photogrammetry based systems suitable for close and micro range

In this chapter, a description of the photogrammetric reconstruction principle and of the mathematical models behind is reported. Finally, the photogrammetry-based system used during the experimental investigations is presented.

4.1 Photogrammetric reconstruction process

The photogrammetric process is composed by two main subsequent steps: *image acquisition* and *image processing* (see *Figure 21*). Firstly, the acquisition of the images has to be carried out considering the choice of the proper optical equipment, as well as, the geometrical parameters defining the scanning strategy (Tilt Angle and Step Angle). This phase is followed by the *alignment* and by the creation of the dense cloud. The former, which is the core of the photogrammetric reconstruction, consists of the computation of internal and external parameters, allowing to obtain points in the 3D space, starting from the 2D information of the images acquired. Finally, the creation of the dense cloud and, eventually, of the texturized mesh is carried out. All the steps involved in the image processing are carried out within the photogrammetric software.

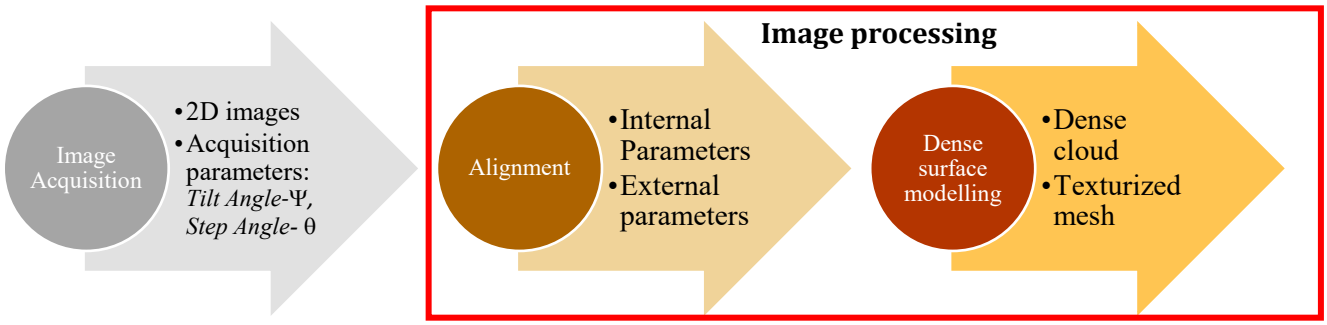

Figure 21 Photogrammetric reconstruction process.

4.1.1 Image acquisition and scanning strategy

One of the main advantages of a photogrammetry-based system is the ability to acquire very complex geometries thanks to the possibility to choose among different scanning strategies. When scanning small objects, using a polar configuration, it is necessary to choose at least two process parameters, tilt angle and step angle, depending on the shape and geometry of the object. Tilt angle (Φ) identifies the tilt of the sensor respect to the *xy* object plane, while the step angle (θ), defined as the rotating step of the turning table, determines the number of images and, then, the overlapping level between two subsequent images. These two parameters geometrically define the acquisition strategy (*Figure 22*).

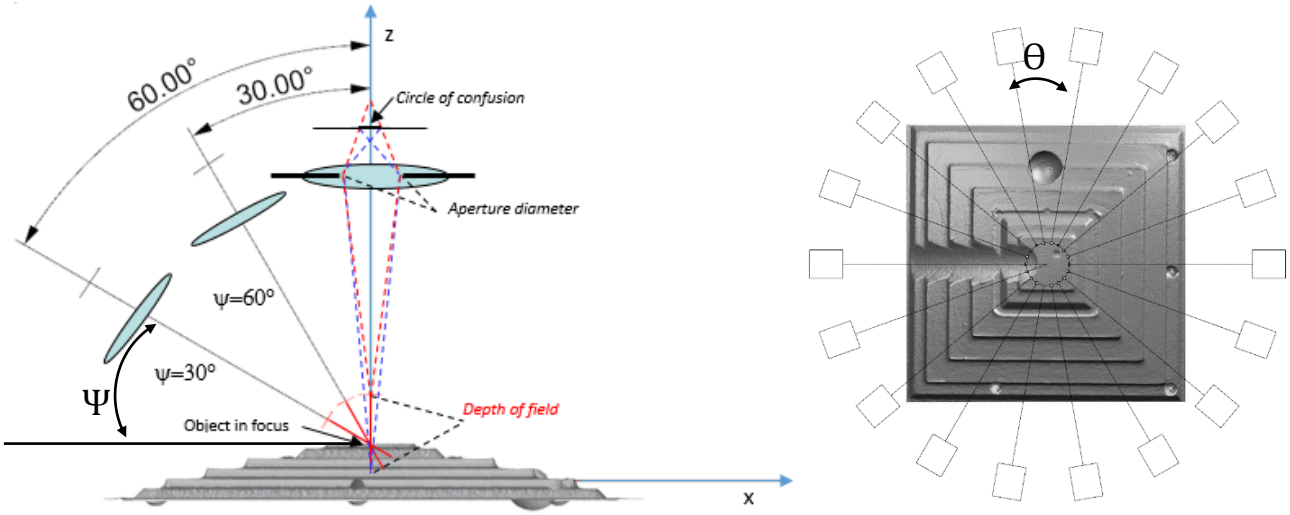

Figure 22 Sensor positions, e.g. configuration Tilt Angle 60°, Step Angle 30° (a). Tilt angle has been indicated as Ψ, and step angle as θ.

The choice of the scanning strategy must be done based on quantitative considerations. When the magnification level increases, there is a corresponding decrease of the field of view and of the depth of field. The depth of field (DoF) indicates the sharpness range (acceptably sharp to the eye) in the area beyond the lens, which depends, firstly, on the lens adopted and, secondly, on the aperture of the camera (A) chosen, well known as f-stop size. Geometrically, it is indicated by the width of a parallelepiped whose dimensions are dictated by the sensor dimensions and the magnification level, which define the length and the height values. Putting the object in focus means that the Plane of Focus (PoF), which lies in the middle of the above defined parallelepiped, is located in correspondence of the center of the object. Solving the Eq. (4.1) for the DoF, considering a value of f-stop size, A, of 22 and a focal length, F, of 50 mm, an extension tube of 36 mm and the diameter of the circle of confusion, c, equal to 0,018 mm, the resulted Depth of field value is about 3 mm. The object distance is considered as the distance between the lens and the object in focus.

$$DoF = \frac{2dF^2Ac(d-F)}{F^4 - (Ac(d-F))^2} \cong 3\ mm \qquad (4.1)$$

Where:

F is the focal length = 50 mm;

Extension tube = 36 mm;

A is the aperture of the camera (f-stop size) = 22;

d is the object distance (from lens) =240 mm;

c is the circle of confusion = 0,018 mm.

The following pictures, *Figure 23* and *Figure 24*, report a graphical example of the practical concept of the depth of field on a pyramidal sample widely used within this thesis.
In *Figure 23*, a configuration with a tit angle value of 60° is reported. As can be seen, a relation between the Tilt Angle (Ψ) and the maximum slope of the test object (α) exists. Generally, the sum of these two angles should be as much close as possible to 90° because a high tilt angle value, leads to a PoF tilted of 30° (almost horizontal), like the almost flat geometry of the test object, which means a great portion of the object in focus. Analogue considerations could be done, considering the second configuration reported in *Figure 24*. In that case, The PoF results to be tilted of 60° and then, almost vertical, which means a low portion of object in focus due to the maximum slope of the object, which is 15°. Consequently, the sum between the tilt Angle and the maximum slope of the object is 45°, far from 90°.

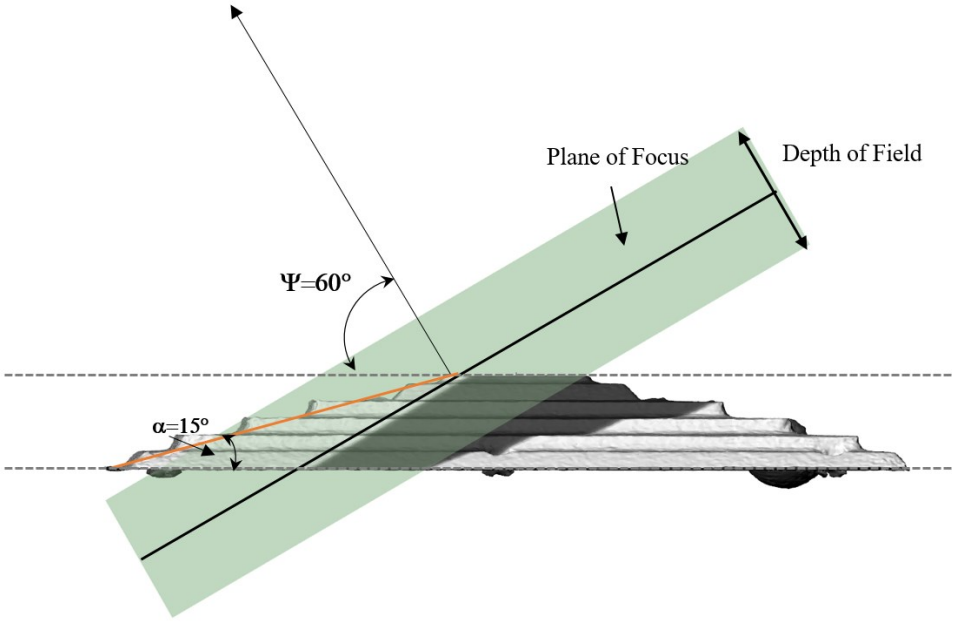

Figure 23 Configuration with camera tilted of 60°; α represents the object slope equal to about 15° for the sample[81].

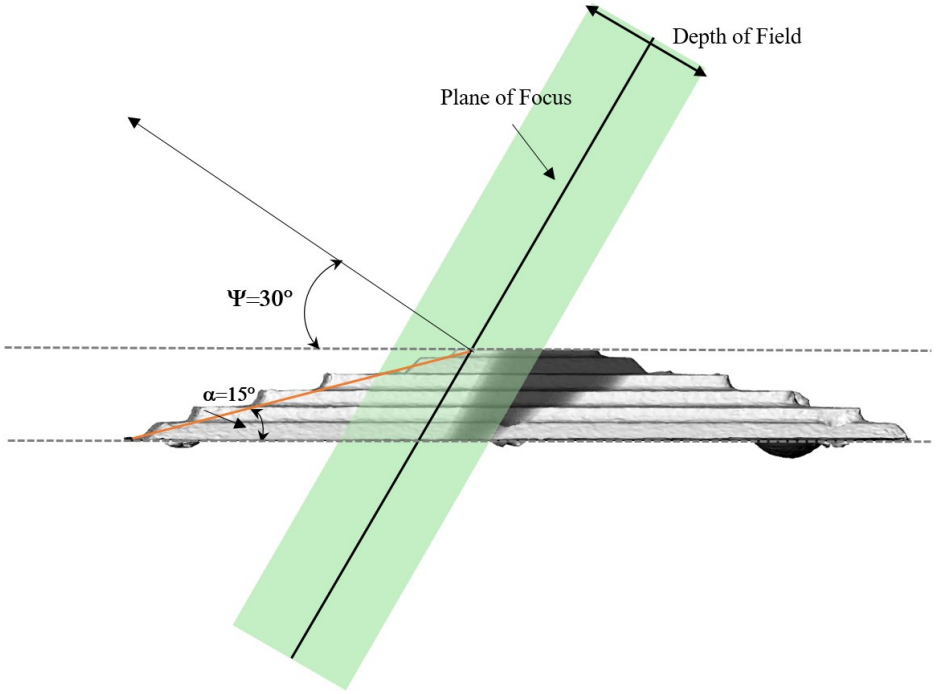

Figure 24 Configuration with camera tilted of 30° [81].

In *Figure 25*, a 3D visualization of the sample in both configurations is reported. On the left, it can be seen a visualization from the camera tilted at 60° respect to the xy plane, while on the right the same visualization from the camera tilted at 30° is reported. This picture confirmed what has been said already. Moreover, a tilt angle of 60° allows to reconstruct deep holes and concave geometries, while a tilt angle of 30° is more suitable for almost vertical geometries.

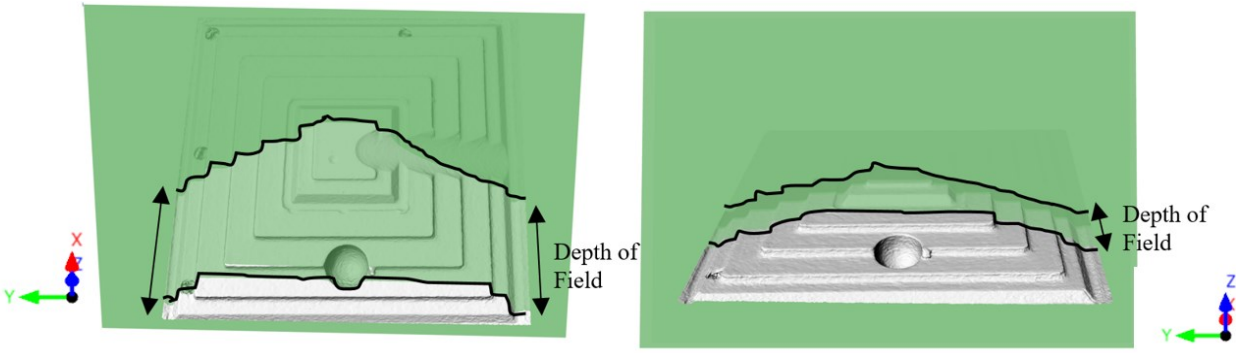

Figure 25 3D tilted views. On the left, visualization from camera tilted of 60° from the xy plane, while, on the right, visualization from camera tilted of 30° from the xy plane [81].

All the discussion, reported in this section, would be representative to understand how the geometrical scanning parameters can affect the goodness of a 3D reconstruction and the best choice must consider these parameters and their relations with the depth of field limitation and the maximum slope of the object under measurement.

4.1.1.1 The development of motorized and automated systems for the image acquisition

The optimization of the scanning strategy is greatly aided by the implementation of motorized systems, which allow to plan and control the scanning strategy through the control of the camera

movements and the rotation of the object. This is an important step for some reasons: firstly, the planning of an automated acquisition leads to a considerable time saving, while the control ensures that the correct distance sensor-object is always respected and the system positioning precision and accuracy traced. Last, but not least, the control of the system ensures the reproducibility of the measuring procedure under controlled conditions.

Motorized systems usually exploit two main cinematic configurations: Cartesian [67] and polar [82]. The polar configuration, characterized by the use of a turning table, which allows to acquire images from multiple views in a structured way (choosing the step angle value), is preferred in many cases because it reduces significantly the space needed for the image acquisition and the overall dimensions of the scanner. It is an important factor, considering the limited space normally available in deposits and conservation labs. The same implementation is more difficult for very large objects, but it surely represented a great advantage for the acquisition of small objects [83]. In [70] a low-cost Photogrammetric Scanning System with Rotary Table (PSSRT) was designed and implemented to return precise 3D digital models of small objects featuring complex surfaces and sub-millimeter features. The system comprised a camera mounted on an arm positioned at fixed angles respect to the rotary table. It allowed great process control, as well as, the assurance of a high reproducibility of the measuring procedure, see *Figure 27*.
The experimental investigations carried out within the present thesis are conducted using a polar configuration.

4.1.1.2 Environmental lighting conditions

Since photogrammetry is an optical-based measuring instrument, it is particularly sensitive to the environmental illumination. Most of the currently available systems tried to overcome this problem, putting the object inside a white box with a diffusely illumination which allows, firstly, to isolate the system from the environmental influences, but also to ensure a more diffusive light effect. A photogrammetric acquisition is affected by reflections and shadows, because they can change during the multi-view acquisition. The latter could be avoided adopting a lighting system, typically white-light led strips, which moves solidly with the rotating table [70].
Another crucial point, in passive photogrammetry, is the sensitivity of this instrument to the object's texture. The term texture can refer to the photogrammetric definition or to the surface metrology definition. The former refers to the *visual texture* (the chromatic characteristics), while the latter refers to the *tactile texture*, which implies the surface profile and roughness. Objects without a good visual texture, such as many injection moulded polymer parts, as well as, parts obtained with additive manufacturing technologies (Stereolithography or Fused Deposition Modelling with polymeric materials), represent a big challenge for this kind of instruments.

4.1.2 Image processing

4.1.2.1 Advances in software developments

The recent success of the photogrammetric technique coincided with the rise of new algorithms capable to reconstruct objects even if the optimal conditions are not fully accomplished.
The *alignment*, i.e. the computation of the internal and external parameters (IO and EO parameters), which describe, respectively, the camera model and the relative camera-object positions registered during the image acquisition, represents the core of the photogrammetric

reconstruction and it is crucial for the success of all the subsequent steps (the dense cloud generation and the meshing process). Thus, the development of new algorithms with the aim of simplifying and automating the *alignment* is of great importance. It could be further decomposed in *feature recognition*, *image matching*, and optimization of the parameters (*bundle adjustment*). At the beginning of the image processing, descriptors are used to recognize features on acquired images. The next *image matching* phase matches common points on images and this is the start of the triangulation process. The quality and the quantity of the recognized features greatly influences the subsequent steps. The data obtained from this phase, as bidimensional vectors, become the input for the next one, the computation of internal and external orientation parameters. The estimation of the internal and external parameters can be carried out in the same phase, starting from the same input, or in two subsequent ones. In this contest, the development of commercial software belonging to the Computer Vision (CV) community, thanks to the high level of automation in data processing, allowed time and computational load saving. The consolidated availability of algorithms, such as Structure From Motion (SFM) and descriptors [84] such as Structure Invariant Feature Transform (SIFT) [85] and SURF [86], simplified and automated the alignment phase, so that, codified targets are no longer necessary, and high quality images are sufficient for the reconstruction of many kinds of objects.

4.1.2.2 Internal and external orientation: mathematical models

The term *alignment*, used in the previous section, is referred to the specific terminology embedded in the reconstruction software used in this thesis [87] and it comprises:

- The estimation of the 10 internal parameters (IO parameters), which define the camera model: focal length, principal point coordinates, distortion parameters and a coefficient called skew; this phase is also known as *camera calibration*, or *internal calibration.* Although this term is usually adopted in the photogrammetric field, the meaning is not the same reported in the VIM (Vocabulary of Metrology) [3];
- The estimation of the mutual positions between cameras and object. It is known as *external orientation* (EO) and in next chapters it will be indicated also as *scale adjustment*.

Before describing the mathematical models behind the photogrammetric reconstruction, it is important to do a clarification. There is a slight difference between the photogrammetric model and the computer vision model. Both are characterized by the same basic concept but there are few distinguishing factors. The basic concept, underlying both, derives from the central projection model. Firstly, two coordinate systems have to be considered: the world coordinate system and the camera coordinate system, see *Figure 26*.
Within these definitions, O and PP denote the perspective centre and the principal point, respectively.

Figure 26 Coordinate Systems for photogrammetry (left) and computer vision (right)

The central projection in three dimensions is described by the following equations (4.2) and (4.3):

$$\begin{pmatrix} X \\ Y \\ Z \end{pmatrix} = \begin{pmatrix} X_0 \\ Y_0 \\ Z_0 \end{pmatrix} + m_x * R(\omega, \varphi, k) * \begin{pmatrix} x - x_0 \\ y - y_0 \\ \pm f \end{pmatrix} \tag{4.2}$$

$$m_x = \frac{1}{\pm f}\left(r_{1\,3}(X - X_0) + r_{2\,3}(Y - Y_0) + r_{3\,3}(Z - Z_0)\right) \tag{4.3}$$

Where:

X, Y and *Z* are the coordinates of an object point in the world coordinates;

X_0, Y_0 and Z_0 are the coordinates of the camera perspective centre in the world coordinates;

m_x is the scale factor;

R(ω, φ, k) is the rotation matrix from the camera coordinates to the world coordinates, function of the three rotation angles;

X_0, Y_0 and Z_0, and ω, φ, k are the six parameters of the external orientation (EO parameters);

x and *y* are the coordinates of an image point in the camera coordinates;

x_0 and y_0 are the coordinates of the principal point, and *f* is focal length (principle distance). They represent the three internal orientation parameters in photogrammetry (IO parameters) and the sign of f depends on which camera coordinates is considered, photogrammetry or computer vision.

The camera model reported in Eq. (4.2) has, in total, 9 degrees of freedom, the three IO parameters and the six EO parameters.
Afterwards, in photogrammetry, the collinearity equations are defined, as well as, the projection equation in computer vision. The collinearity equations in photogrammetry are the Cartesian representation of the central projection in Euclidean geometry, while the projection equation in computer vision is the homogeneous representation of the central projection in projective geometry. The mathematical fundamentals of photogrammetry and computer vision are

essentially the same. In this section, only the projection equation will be reported, because, for the experimental investigations conducted in this thesis, only a computer vision product was used, Agisoft Photoscan [87].

$$\begin{pmatrix} X' \\ Y' \\ Z' \end{pmatrix} \triangleq R^T \begin{pmatrix} X - X_0 \\ Y - Y_0 \\ Z - Z_0 \end{pmatrix} = R^T \begin{pmatrix} 1 & 0 & 0 & -X_0 \\ 0 & 1 & 0 & -Y_0 \\ 0 & 0 & 1 & -Z_0 \end{pmatrix} \begin{pmatrix} X \\ Y \\ Z \\ 1 \end{pmatrix} \tag{4.4}$$

Considering $m_x = Z'/f$ and by considering $f = f * Z'/Z'$, the equation (4.4) becomes:

$$Z' \begin{pmatrix} x \\ y \\ 1 \end{pmatrix} = \begin{pmatrix} f & 0 & x_0 \\ 0 & f & y_0 \\ 0 & 0 & 1 \end{pmatrix} \begin{pmatrix} X' \\ Y' \\ Z' \end{pmatrix} \tag{4.5}$$

The result is that coordinates of the image points are independent on the Z depth, so that the Eq. (4.5) becomes:

$$\begin{pmatrix} x \\ y \\ 1 \end{pmatrix} = P \begin{pmatrix} X \\ Y \\ Z \\ 1 \end{pmatrix} \tag{4.6}$$

Where:

$$P = KR^T[I| - C] \tag{4.7}$$

K is the calibration matrix:

$$K = \begin{pmatrix} f & 0 & x_0 \\ 0 & f & y_0 \\ 0 & 0 & 1 \end{pmatrix} \quad , \quad C = \begin{pmatrix} X_0 \\ Y_0 \\ Z_0 \end{pmatrix}$$

Equation (4.7) is the projection equation better known as the basic pinhole camera model.
In CCD cameras, two parameters are added into the calibration matrix, see Eq. (4.8):

$$K = \begin{pmatrix} f & s & x_0 \\ 0 & \alpha f & y_0 \\ 0 & 0 & 1 \end{pmatrix} \tag{4.8}$$

Where α is the aspect ratio and s is the skew parameter.
The aspect ratio is the ratio between the pixel size along x and y and due to its definition, it is 1 for square pixel, while the skew parameter accounts for the misalignment between the pixel axis, but, in most cases, it is considered 0. These two parameters allow to fill the gap of DOF between a general 3x4 camera matrix and the pinhole camera model.
The projection equation (4.7) is the fundamental formula in computer vision and, due to its linear form, many analytical methods in computer vision are linear.

4.1.2.3 Criticalities of the implemented methodologies for IO and EO computation, when measuring small objects with sub-millimeter feature

The implementation of the traditional mathematical models belonging to the photogrammetric field and the computer vision, present some limitations when measuring small object with sub-millimeter feature, because they require the use of zoom lenses, macro lenses or lenses with extension tubes. Firstly, the estimation of the internal parameters become more difficult: using zoom lenses implies a bad stability of estimated parameters, while, for every narrower field of view, the traditional collinearity model could lead to an unstable camera model. Another criticality is related to the size of calibration pattern needed, which has to be of the same order of magnitude of the measured sample, so that the internal calibration carried out in the laboratory is not obvious as for the other dimensional ranges. The necessity to develop good procedure for autocalibration (which is the corresponding word in computer vision for the self-calibration procedure in traditional photogrammetry) led to the development of algorithms able to extract the necessary information from the multi-view images of the objects, without requiring any initial information or the calibration usually carried out in the laboratories [82,88,89]. A set of images depicting a scene with a good texture is sufficient for the extraction of natural corresponding image points. These are automatically matched with feature-based approaches and robust estimation techniques. The successive photogrammetric bundle adjustment retrieves the unknown camera parameters and their theoretical accuracies.
The higher quality of the results often obtained with the autocalibration, is due to the fact that the internal calibration conducted in the laboratory is often carried out with different environmental conditions respect to the acquisition of the sample and, for example, the influence of a different illumination is not taken into account. After the estimation of the internal parameters, the external orientation is computed (EO parameters) less than a scale factor. This is one drawback of the photogrammetric process, but several ways to produce a real scaled object have been developed. Codified targets with known absolute coordinates and distances, placed around and on the sample surface, are used to provide the scale factor and contemporary a coordinate reference system. This is the most used procedure in large scale and close-range photogrammetry, but when small objects with sub-millimeter feature have to be acquired, its application becomes more difficult. When the magnification level increases, the object cover more than the 80% of the image, with few possibilities to place codified targets around it. Placing targets on the object surface is also quite difficult because of the presence of small features, as well as free-form shaped parts. This led to the necessity to find other ways to compute the scale factor. A recent methodology consists in using reference objects with codified targets to compute the external orientation with the correct scale factor. The reference object could be a 2D pattern of targets or a 3D geometry with targets with known positions already measured with an optical CMM [70]. To ensure the success of this procedure, the same acquisition strategy must be used for the reference object and for the sample to be reconstructed, which involves the same optical configuration, the same reciprocal position between camera and the object, the same number of images. This condition is ensured by using systems with automatically controlled axis or systems in which camera (or cameras) are fixed and the object is placed always in the same position. The main advantage of this *scale adjustment* method is that it is not user-dependent, and it can be used for every kind of objects, independently on their shape. Moreover, it involves the usage of optical coordinate measuring machine to measure targets positions on reference objects and it provides a reliable result. The first drawback is represented by the realization of these reference objects, because, the higher is the magnification level required, the smaller is the field of view

and the smaller is the size of codified targets to use (less than 1 mm). The simplest way is to print them on paper, but commercially available printers are not able to ensure a sufficient printing quality.

4.2 Critical issues affecting a photogrammetry-based system

The relevant factors for an optical 3D scanning system based on photogrammetry are listed and explained below [90]:

Camera sensor – The quality, the number of pixels, pixel size, and the size of the sensor are very important. To obtain high quality for photogrammetric scanners good quality CCD or CMOS sensors must be used. Increasing the number of pixels of the sensor will increase the resolution, but smaller pixel and sensor sizes will give lower signal/noise ratios. For this reason, full frame or APS-C sensors must be preferred.

Camera lens – The quality and the focal length of the optics are very important. Higher quality lenses produce better images with lower distortions. Higher focal length allows higher camera-object distance and the camera-object distance, increases the magnification ratio and the number of images needed for the photogrammetric reconstruction.

Images Overlapping – Photogrammetry needs an overlap among adjacent images, of about the 80%.

Internal calibration – It is of great importance to evaluate the stability of this phase when dealing with specific optical configurations, such as zoom lenses, macro lenses or lenses with extension tubes, especially when it is carried out as *autocalibration* together with the estimation of the external parameters.

Resolution - The ability to distinguish two objects or features from each other is fundamental in optical 3D metrology. This represents the structure resolution limit of detection of an instrument. It is divided into two component: a lateral part, which is the perpendicular component, and an axial part, which is the parallel component, both with respect to the 3D sensor's optical axis. In photogrammetric field, the lateral resolution (Equation 4.9) (GSD: Ground Sampling Distance) is calculated as [91]:

$$\mathrm{GSD}\left[\frac{\mathrm{mm}}{\mathrm{pixel}}\right] = \frac{\text{Flying Altitude[mm]}}{\text{Focal Lenght[mm]}} * \text{Pixel size [mm/pixel]} \qquad (4.9)$$

Software Repeatability – software and algorithms developed in 3D image systems played a fundamental role for the application of these techniques.

Hardware - in case of motorized and controlled system, it would be interesting to quantify the influence of any errors in axis positioning on resulting reconstruction.

Scale adjustment–the estimation of internal and external parameters is carried out less than a scale factor.

Texture-dependency - The term texture can refer to the photogrammetric definition or to the surface metrology definition. The former refers to the *visual texture* (the chromatic characteristics), while the latter refers to the *tactile texture*, which implies the surface profile and roughness. Triangulation-based techniques require reference artefacts that have cooperative optical surface characteristics. However, in order to quantify a 3D optical scanner's

ability to measure different surface finishes (material, reflectance, roughness and colour), National Physical Laboratory's (NPL) developed the 3D material coupon plate, a multi-faceted test artefact [35].

Environmental characteristics – (temperature, humidity, lighting conditions). Their effects could be reduced if measures are carried out in a controlled environment. Anyway, temperature affects not just the object to measure but also the 3D optical scanner. Ways to quantify thermal effect and illumination effect on 3D optical scanners are reported in [92].

4.3 Presentation of the photogrammetry-based system used for the experimental investigations - PSSRT

The photogrammetry-based system adopted consists of an hardware and a software part.
The physical part is based on the structure described in [70], see *Figure 27,* and it was completely redesigned and improved in several aspects. At first, every camera movement has been completely automated. The camera axis performs a tilting and a linear translation movement. The former is used to adapt the tilting of the sensor to the specific geometry of the object as explained in *section 4.1.1*, while the translation is necessary to get closer or farther respect to the object in order to get it in focus. Every axis has been equipped with an encoder having a resolution equal to 0,004° for the tilting axis Ψ, 0,001mm for the axis ensuring the linear translation of the camera and 0,18° for the rotating axis Θ, with the aim to know exactly the spatial camera position. The system has been programmed to automatically acquire images, according to the scanning strategy adopted, and to storage the set of acquired images in the desired directory.

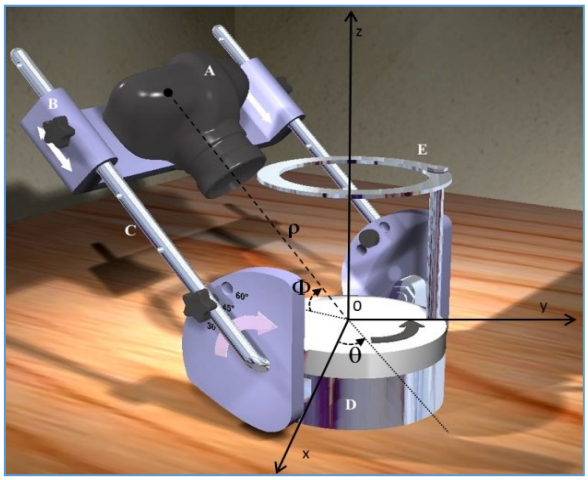

Figure 27 Design of the proto-type realized for the low-cost Photogrammetric Scanning System with Rotary Table: A) Digital SLR Camera; B) Platform for focus distance tuning; C) Rigid tubular frame for tilt angle tuning; D) Rotary Table; E) Light [70].

The software for the image processing is Agisoft Photoscan, using, in particular, the versions 1.0.4, and 1.2.6.

Table 1 Camera, sensors and main characteristics of the optical equipment used during the experimentations.

Camera model	Sensor	Tested Measuring Volume (mm3)	Focal length (mm)	Extension Tube (mm)	Pixel size Mm/pixel	Magnification level	GSD mm/pixel	Depth Resolution mm/pixel
Canon EOS 760D	**APS-C 22,2x14,8 mm²**	74x42x25	50	20	0,0037	0,3	0,012	0,024
Canon EOS 40D	**APS-C 22,2x14,8 mm²**	32x18x10	50	36	0,0057	0,7	0,0081	0,0162
Canon EOS 6D	**Full frame 36x24 mm²**	36x20x11	100	-	0,0066	1	0,0066	0,012
Canon EOS 400D	**APS-C 22,2x14,8 mm²**	9x5x3	60	60	0,0057	2,4	0,0024	0,0048
		10x5x3	60	52	0,0057	2,23	0,0027	0,0054
		11x6x4	60	44	0,0057	2,06	0,0029	0,0058

Where the measuring volume, expressed as $MV=ML_X \times ML_Y \times ML_Z$, is a function of:

- magnification level (M);
- sensor dimensions (along x and y);
- sensor tilt angle (Ψ) respect to the object.

In Figure 28 a graphical representation is reported.

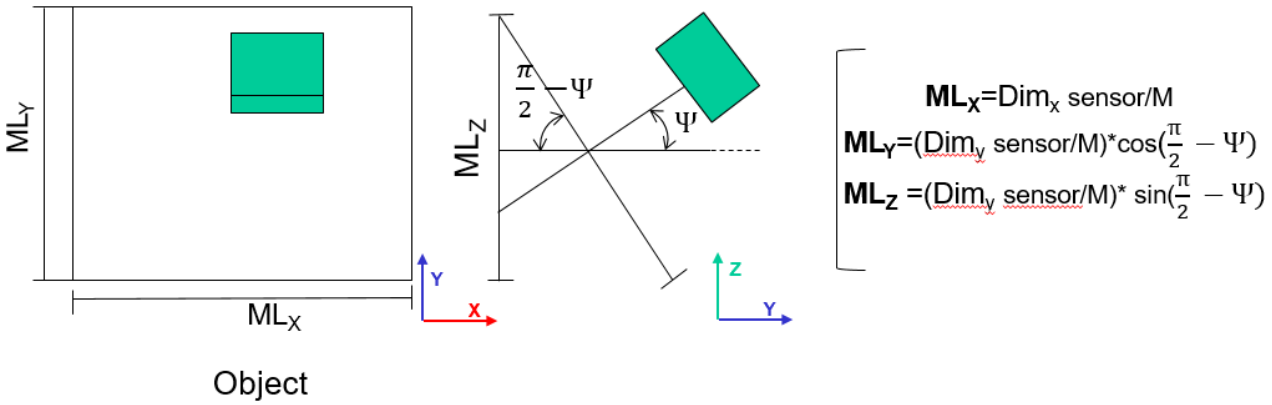

Figure 28 Measuring volume dependency on sensor dimensions, M and the tilt angle (Ψ) value.

In the following chapters, the photogrammetric system will be indicated with PSSRT (Photogrammetric Scanning System with Rotary Table) as in [70].

Chapter 5 - Experimental Investigation on software repeatability

The reconstruction software play a fundamental role in any 3D image processing systems. The measuring principle is embedded in the algorithms, which transform information from 2D images in 3D models. Due to their great importance within the photogrammetric reconstruction, they have also to be included in the uncertainty assessment.
Purpose of the experimental investigation reported in this chapter, is computing the component of the 3D reconstruction uncertainty due to the repeatability of the software used for the reconstruction. Due to the complexity of the entire image processing phase, in this investigation only the alignment was considered. It comprises the reconstruction of the internal and external orientations (IO and EO parameters).
It is important to underline that all the results and considerations, carried out from this investigation, are related to the specific test object used, which presents an optimized design to test the suitability of a photogrammetric scanning system for micro and sub-millimeter features placed on a complex shape.

5.1 Materials and methods

In a previous work [65], four artefacts characterized by similar geometry and overall dimensions were reconstructed and the statistical uncertainty component related to the reproducibility of the photogrammetric scanning system was computed.
With the aim to evaluate the uncertainty component due to the software repeatability, the artefact, which reported the lowest data dispersion was considered as test object of this investigation. The artefact presents a pyramidal structure, with a square base and six steps, see *Figure 29.* An experimental plane was designed, comprising two factors, linked to the acquisition strategy, and a process parameter set during the image processing. Among these factors, tilt angle is defined as the angle comprised between the camera axis and the object plane, while the step angle determines the number of photos. The point limit value, which is the upper limit of matching points of each image involved in the alignment process, was considered as the third factor. Each factor was considered at two different levels with the result of a 2^3 factorial plane with three repetitions. Due to their definition, only external factors define the number of required acquisitions, so that, 22 acquisitions were realized, each for every scanning configuration, while the total number of processed projects is 23 x 3 = 24.

TEST OBJECT

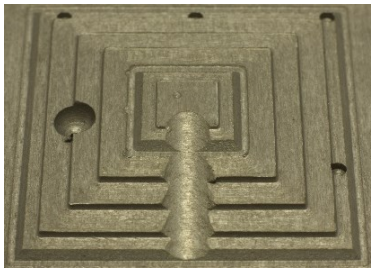

Base [mm²]	24 x 24
Total Height [mm]	2,75
Step Height [mm]	0,5/0,25

EXPERIMENTAL PLAN

Factors	**Low level**	**High level**
Tilt Angle (Ψ)	30°	60°
Step Angle (θ)	18	72
Point Limit (P.L.)	40000	400000

Figure 29 Test object and experimental plane description.

5.1.1 Scanning strategy adopted and image processing

The images acquisition was done with the PSSRT equipped with a digital SLR camera Canon 40D (Effective pixels 10 megapixels), sensor size APS-C (22,2 mm x 14,8 mm), with Canon EF 50 mm 1:1:8 II lens focused to infinity and a Kenko Extension Tube of 36 mm length. The two tilt angle values, chosen in the factorial plane, are the results of preliminary tests [70] and represent two extreme cases. A high slope like 60° is to prefer particularly for geometry with length much higher than height (almost flat geometry), or for the inspection of deep areas such as deep holes or concave geometries. Otherwise, for almost vertical object, a lower tilt angle value works better. The image processing was conducted with Agisoft Photoscan, software version 1.0.4 [65]. Agisoft Photoscan is probably one of the most widely used commercial software for many advantages. It implements a descriptor similar to the SIFT (Scale Invariant Feature Transform), the SFM (Structure from motion) algorithm for the estimation of the external and internal parameters, which describe the camera model, and a SGM (Semi Global Matching) method based on a Multi-view stereo mode for the dense surface model generation. Many research works documented its performances from short to middle-long dimensional range and it is generally considered as a very flexible solution.
The alignment phase starts from the feature detection and finishes with the optimization of the parameters estimated. The first step is the recognition and the feature matching among the acquired images. Using the typical language of the software Agisoft Photoscan, this step can be done more quickly enabling the pair selection mode [86], which is a way to save time thanks to the creation of a subset of photos to be matched. With the software version 1.0.4, there are two options, the *generic mode*, which selects pairs of overlapping photos based on the number of matching points, and the *ground control mode*, which selects the pairs of photos starting from already estimated camera positions.
The *ground control* mode is often used in aero-photogrammetry thanks to the gps coordinates and remote sensing. In this investigation, the experimentation has been carried out using the *ground control* pair selection mode, because it allows to obtain a real dimension model. In particular, the specific procedure, described in *Figure 30*, was followed.

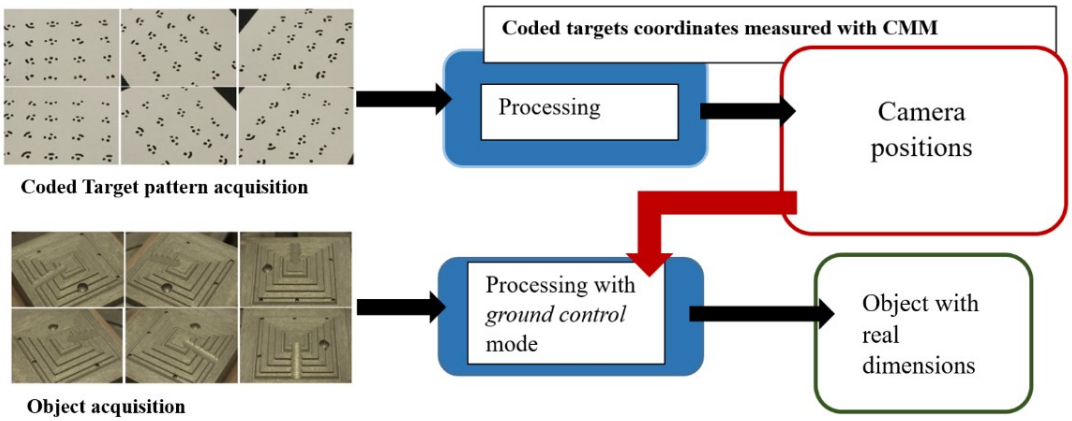

Figure 30 External orientation with the scale factor computed through a pattern of targets with known coordinates[81]

According to *Figure* 30, the pattern of coded target and the test object have to be acquired in two subsequent acquisitions under the same conditions. The pattern of target was previously measured with a CMM DeMeet 400, 1,5 × magnification, MPE X = 5,33 µm, Y = 5,33 µm, Z = 4,33 µm.
Regarding the camera model and the estimation of the internal parameters, they were obtained during the alignment phase from the same images used for the reconstruction.
At each software iteration (three in total), maintaining the same conditions, a variability in the estimation of the parameters describing the camera model can be observed and, understanding the contribution of the variability of each of these parameters to the output, becomes of great importance.

5.2 Methods for evaluating the repeatability of the software

5.2.1 Reprojection Error (RE)

The first output variable for the evaluation of the repeatability of the software algorithms during the alignment phase is the Reprojection Error (RE). It is a geometric error used to quantify how closely a 3D point estimate recreates the point's true projection and it is defined as the difference between a projected point (u, v) and a measured one (X,Y). For its definition, it is often used to evaluate the quality of the calibration. In *Table 2*, results related to the variability of the RE throughout the repetitions are reported, in terms of average values, standard deviation and max-min range.

Table 2 Reprojection Error computation and variability.

Groups	Average R,E [pixel]	Max-Min [pixel]	Standard Dev, [pixel]	(Max-Min) *Ground Resolution [mm]	(Max-Min)* Vertical Resolution [mm]
I C - P,L, High	0,4022	0,0006	0,0003	5,04E-06	1,008E-05
I C - P,L, Low	0,5202	0,0006	0,0003	5,04E-06	1,008E-05
II C - P,L, High	0,3566	0,0004	0,0002	3,36E-06	6,72E-06
II C - P,L, Low	0,4783	0,0017	0,0010	1,428E-05	2,856E-05
III C - P,L, High	0,3989	0,0001	0,0001	8,4E-07	1,68E-06

III C - P,L, Low	0,5058	0,0004	0,0002	3,36E-06	6,72E-06
IV C - P,L, High	0,4468	0,0523	0,0275	4,39E-04	8,79E-04
IV C - P,L, Low	0,5284	0,0121	0,0061	1,02E-04	2,03E-04

Although, a low Reprojection error (less than 1 pixel) is not always a good indicator of the quality of 3D reconstruction. Thus, for this purpose a further analysis was carried out, investigating more deeply the camera model behind the photogrammetric reconstruction.

5.2.2 Proposed mathematical model for the computation of the repeatability of the reconstruction software during the alignment

The repeatability of the reconstruction software during the alignment phase, Rep_inst_i, was computed for each set of iteration with fixed conditions, as the root sum squared of two components:

- Variability of the projected point coordinates estimated through the camera model implemented in the software $\Delta(u,v)_t$;
- Variability of the estimation of the external orientation (relative camera positions), CPsi.

$$Rep\_inst_i = \sqrt{CPs_i^2 + \Delta(u,v)_t^2} \qquad (5.1)$$

With i= each set of iteration= 1, 2 …, 2^3

5.2.2.1 Variability of the projected point coordinates, $\Delta(u,v)_t$

The description of the camera model, implemented by Agisoft Photoscan, involve the computation of 10 parameters: focal length, principal point coordinates, distortion parameters and a coefficient called skew.
The camera model describes the transformation from the coordinates of the points in the local camera coordinate system to the image coordinate system (see *Figure 31*). The local camera coordinate system has its origins in the camera projection centre. The mathematical model implemented in the software, for this specific optical equipment and configuration, led to the estimation of 7 internal parameters, 2 for the focal length, 2 for the principal point estimation and 3 for the radial distortion. All the rest was considered negligible.

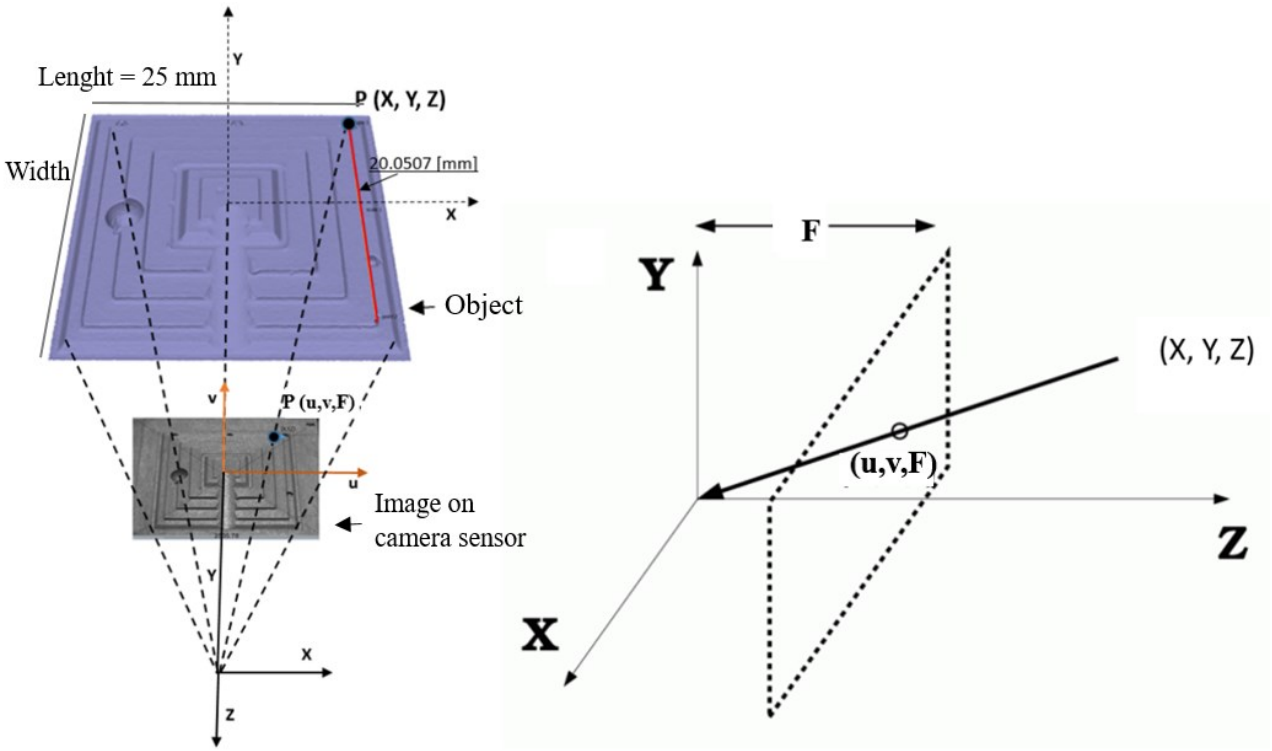

Figure 31 Projection model [81]

Points coordinates in the form of X, Y e Z coordinates in the local camera reference system can be projected in the image reference system through the following equations:

$$x = X / Z \quad (5.2)$$

$$y = Y / Z \quad (5.3)$$

$$r = sqrt(x^2 + y^2) \quad (5.4)$$

$$x' = x(1 + K_1 r^2 + K_2 r^4 + K_3 r^6) + P_2(r^2 + 2y^2) + 2P_1 xy \quad (5.5)$$

$$y' = y(1 + K_1 r^2 + K_2 r^4 + K_3 r^6) + P_1(r^2 + 2y^2) + 2P_2 xy \quad (5.6)$$

$$u = C_x + x' F_x + y' skew \quad (5.7)$$

$$v = C_y + y' F_y \quad (5.8)$$

Where:

(X,Y,Z) - point coordinates in the local camera coordinate system;

(u,v) - projected point coordinates in the image coordinate system (in pixels);

(F_x, F_y) - focal length;

(C_x, C_y) - principal point coordinates;

K1, K2, K3 - radial distortion coefficients;

P1, P2 - tangential distortion coefficients;

skew - skew coefficient between the x and the y axis.

With the aim to investigate the contribution of the variation of each parameter of the camera model to the projected point coordinates, a sensitivity analysis was conducted, considering each parameter at a time, being equal all other parameters. E.g. "How does ΔF =1 pixel affects the projected point (u,v)?"
This computation was done for all parameters involved and the sensitivity coefficients (CS_i) were estimated for each parameter, considering a Δinput equal to 1. Results are reported in Table 3.

Table 3 Computation of the sensitivity coefficient for each internal parameter.

ΔInput	**ΔOutput**	**Δ [Pixel]**	**Mean [Pixel]**	**Cs_i = Δ/Mean**	**% C_s**
ΔF=1 [Pixel]	Δu	-0.0907	3380.45	**2.68E-05**	0.0027%
	Δv	-0.0605	2193.39	**2.76E-05**	0.0028%
ΔC_x=1 [Pixel]	Δu	1	3380.90	**2.96E-04**	0.0296%
	Δv	1	2193.86	**4.56E-04**	0.0456%
ΔC_y=1 [Pixel]	Δu	-13.571	3373.62	**4.02E-03**	0.4023%
	Δv	-9.047	2188.84	**4.13E-03**	0.4133%
ΔK_1=1	Δu	-13.571	3373.62	**4.02E-03**	0.4023%
	Δv	-9.047	2188.84	**4.13E-03**	0.4133%
ΔK_2=1	Δu	-0.1946	3380.30	**5.76E-05**	0.0058%
	Δv	-0.1297	2193.30	**5.92E-05**	0.0059%
ΔK_3=1	Δu	-0.0907	3380.45	**2.68E-05**	0.0027%
	Δv	-0.0605	2193.39	**2.76E-05**	0.0028%

Hence, for each set of iterations, statistics were computed and reported in the Table A1 (Appendix).
The output of the analysis was represented by the projected point coordinates, (u,v). And the variation of the output due to the variation of the input was computed as follows:

$$\Delta u_i[\text{px}] = S_i * Cs_i \tag{5.9}$$

$$\Delta v_i[\text{px}] = S_i * Cs_i \tag{5.10}$$

$$\Delta(\text{u},\text{v})_i[\text{px}] = \sqrt{(\Delta u + \Delta v)_i^2} \tag{5.11}$$

$$\Delta(\text{u},\text{v})_t[\text{px}] = \sqrt{\sum(\Delta(u,v)_i^2)} \tag{5.12}$$

$$\Delta(\text{u},\text{v})_t[\text{mm}] = \left(\sqrt{\sum(\Delta(u,v)_i^2)}\right) * (ground_{resolution}) \tag{5.13}$$

With S_i = standard deviation evaluated on 3 repetitions of i^{th} factor and i= F, C_x, C_y, K_1, K_2, K_3

From results obtained applying the reported equations, from (5.1) to (5.13), considering the sensitivity coefficient for each parameter, the maximum variation registered on the output coincided with the configuration with low tilt angle value (30°), low number of images and point limit low. Even though, the variation in this case was found to be 0,0015 mm.

5.2.2.2 Variability of the external orientation (relative camera positions), CPs_i

In this investigation, the external orientation was pre-computed based on the data obtained from the pattern of targets previously measured with a CMM with an optical probe (DeMeet 400, 1.5 X magnification, resolution of 0,5 μm). The output parameter for the external orientation was not, then, the camera positions themselves, but the Error estimated by the software over the camera positions pre-computed, E(m). The total error E(m) on pre-computed coordinates is the RMS of distances between the camera position entered in ground control panel and the camera position re-computed at the end of the bundle adjustment procedure.

$$E(m) = \sqrt{\frac{1}{n}\sum_{i=1}^{n} \Delta CP^2{}_i} \qquad (5.14)$$

Where:

ΔCPi: *i-camera position distance* is the Euclidean distance between the i^{th} camera position pre-computed and imported and the i^{th} camera position obtained by the software after the bundle adjustment optimization.

$$\Delta \mathrm{CP_i} = \sqrt{(\Delta x^2 + \Delta y^2 + \Delta z^2)} \qquad (5.15)$$

Then, the standard deviation of the three subsequent results obtained was computed.

$$CP_{S=}\, S_x(E(m)) \qquad (5.16)$$

Where:

S_X is computed as the standard deviation of $E(m)_i$ which is the E(m) computed according to the Eq. (5.14) for each i^{th} iteration.

5.2.3 Computation of the uncertainty component due to the software repeatability

The statistical uncertainty, due to the repeatability of the software, was computed through the variability obtained in the 3D comparisons with a model obtained with a conoscopic holography laser scanner with 50 mm HD lens mounted, considered as reference model. The 3D comparisons were carried out using the commercial software Geomagic Control, which allows to achieve a best fit alignment thanks to the Iterative Closest Point algorithm (ICP) between the reference and the test models and, then, computes the deviations expressed as average distance between homologous points on the reference and on the test model. An example of 3D comparison is reported in *Figure 32.*

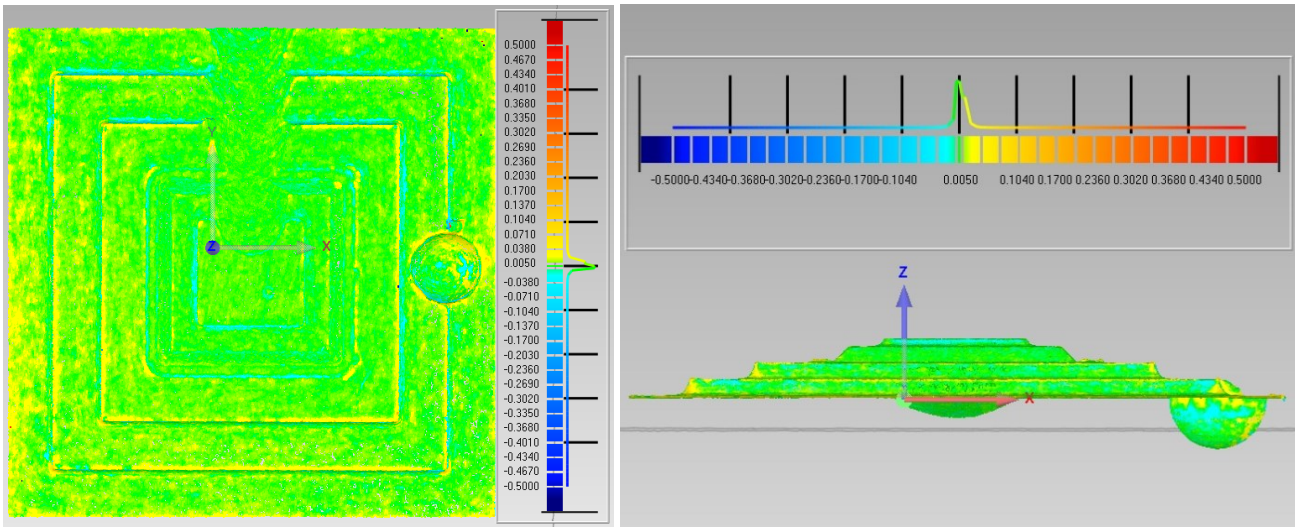

Figure 32 Example of 3D comparison carried out with the software Geomagic Control [81].

The output value chosen was the average distance between the test and the reference model, obtained from the 3D comparison, and then the statistical uncertainty was computed according to the [5], by the statistical analysis of a set of observations, Eq. (5.17).

$$U_R = \frac{S_x}{\sqrt{n}} \tag{5.17}$$

Where:

S_x is the experimental standard deviation calculates as the square root of the variance;
n is the number of observations, or, in this case, the number of iterations of each set.

5.3 Results

Results are expressed as average distances between homologous points on the surface models and as standard deviation of these differences, see *Figure 33*.

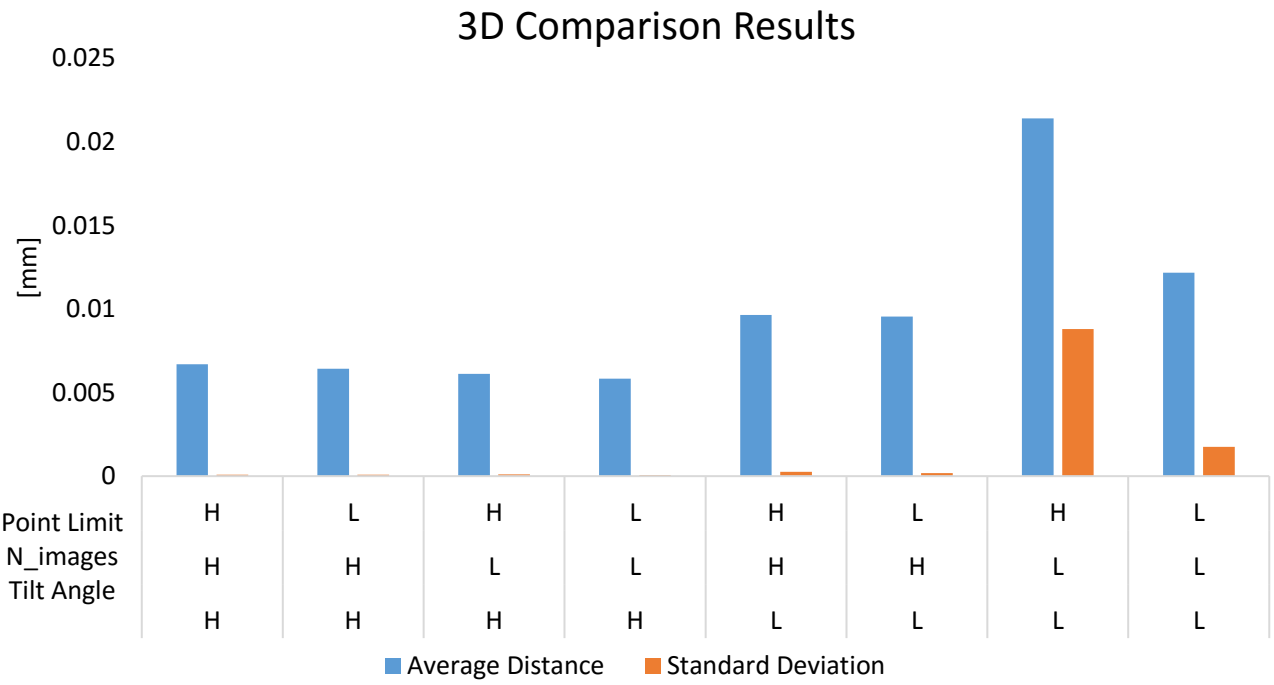

Figure 33 3D Comparison Results: average distances respect to the reference model and Standard Deviation over three repetitions.

Finally, the repeatability computed according to Eq. during the alignment, was compared with the standard uncertainty evaluated on the final 3D reconstructed models. Results are reported in *Figure 34.*

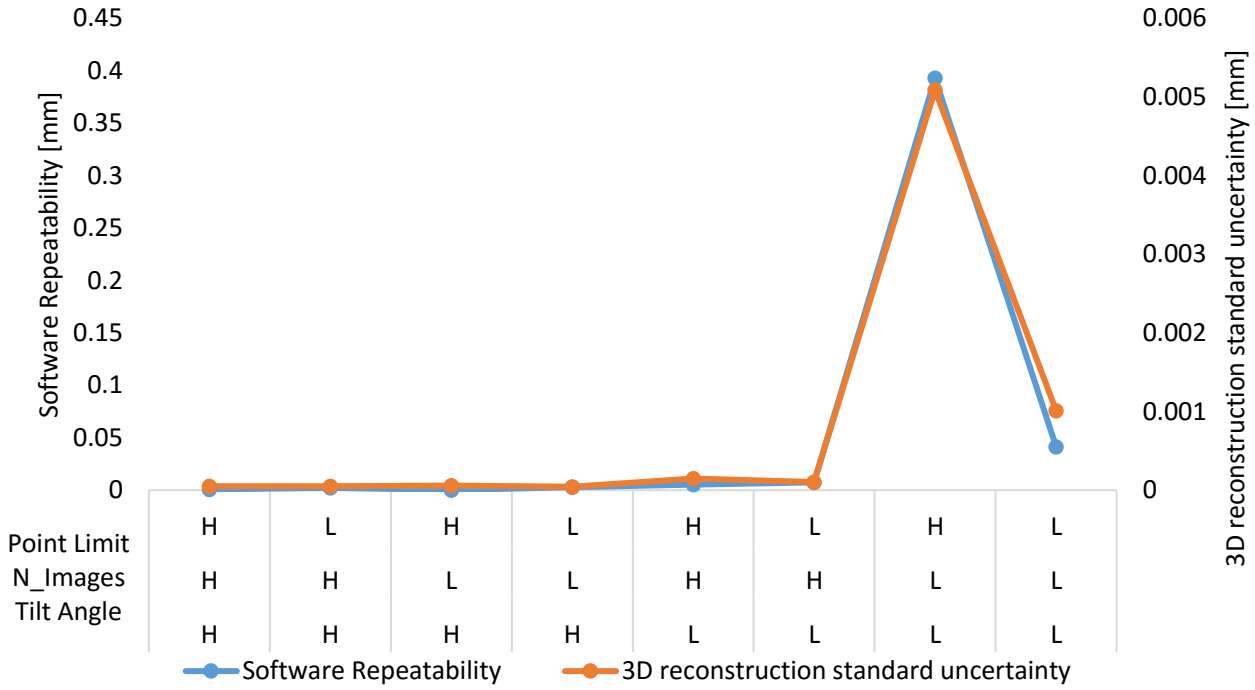

Figure 34 Relation between software repeatability computed according to Eq (5.1) and the statistical uncertainty obtained in 3D reconstruction.

Results obtained highlights two main aspects.
The first is that the factor, which mostly affected both the repeatability of the software and the reconstruction statistical uncertainty was the Tilt Angle, see *Figure 33*. While the number of images is an influential factor just in combination with a low tilt angle value, which is the same consideration obtained in [70]. Moreover, as it is possible to observe in *Figure 34*, the software repeatability and the 3D reconstruction uncertainty follow the same trend, even if with different scale. This means that the amount of influence, expressed as statistical uncertainty of the 3D reconstruction, is generally two order of magnitude lower than the software repeatability computed according to the Eq. (5.1) and it is related to the configuration involved. Thus, the standard uncertainty due to the software repeatability could be considered negligible when the combination of external parameters, Tilt Angle and N of images is optimum configuration for the 3D reconstruction.

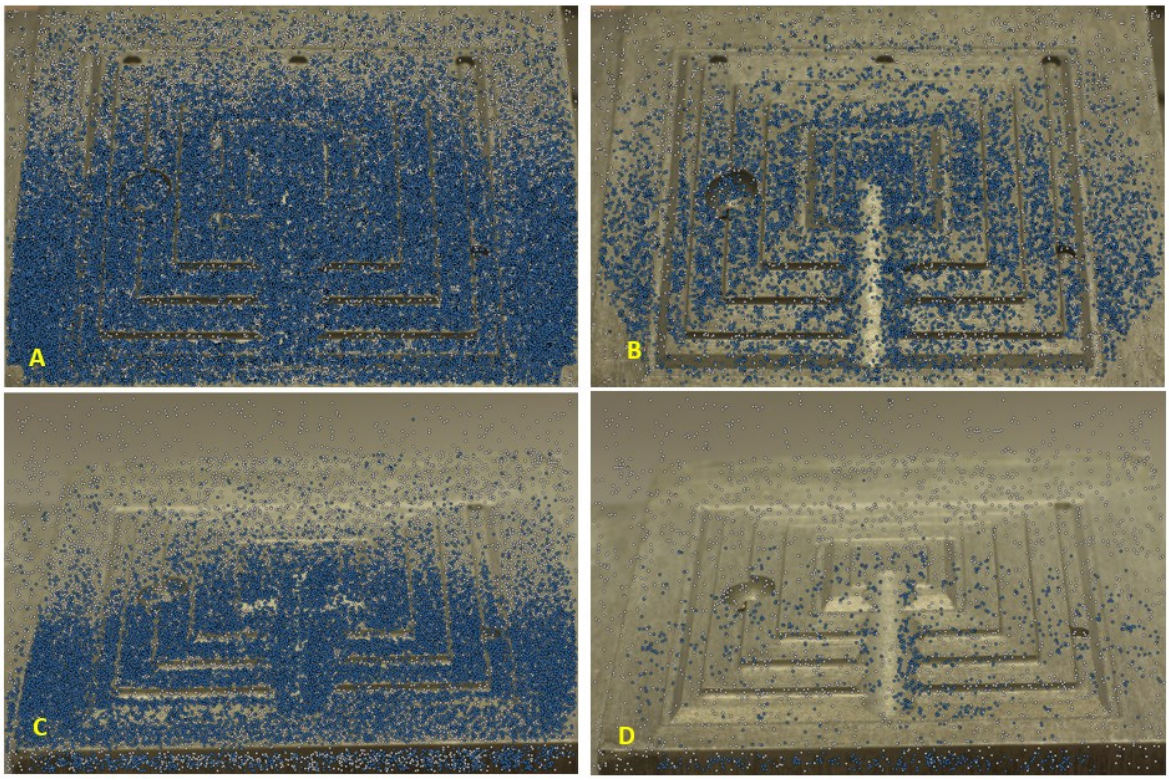

Figure 35 Tie points (blue points) detected on the same picture (Θ =0°), according to the different configuration. A (Ψ=60°, Θ=5°); B (Ψ=60°, Θ=20°); C (Ψ=30°, Θ=5°); D (Ψ=30°, Θ=20°) [81].

Moreover, in *Figure 35*, images of points detected during the alignment process, called *tie points* or matching point projections, were reported for each shooting configuration. The number of tie points is directly influenced by both tilt angle value and step angle. As it was previously discussed, a low tilt angle value means that the focus is on the vertical faces and then, for object almost flat, this means that the object represents only a low percentage of the entire photo. Otherwise, a high tilt angle allows to obtain, for this kind of artefact, a good percentage of the object covering the image. In *Table* 4 some outputs from the alignment phase are reported, comparing the four configurations adopted in this investigation.

Table 4 Comparison between two images with different tilt angle and results in terms of number of points after the alignment process.

Tilt Angle	**30°**	**60°**
Photo coverage	43,32%	64,58%
Ground resolution	8,35 µm /pixel	8,34 µm /pixel
Vertical Resolution	16,7 µm /pixel	16,7 µm /pixel
Sparse cloud (72 photos)	430818 points	596165 points
Sparse cloud (18 photos)	6756 points	80899 points

Tilt angle value also affects the quality of photos expressed as errors [pixel] computed on the images (*Figure 36*). This picture refers to image residuals on the photos computed as the average vector of the Reprojection error for the pixels in the corresponding cells. Therefore, the averaging is done across all the images in the calibration group and all the pixels inside the cell.

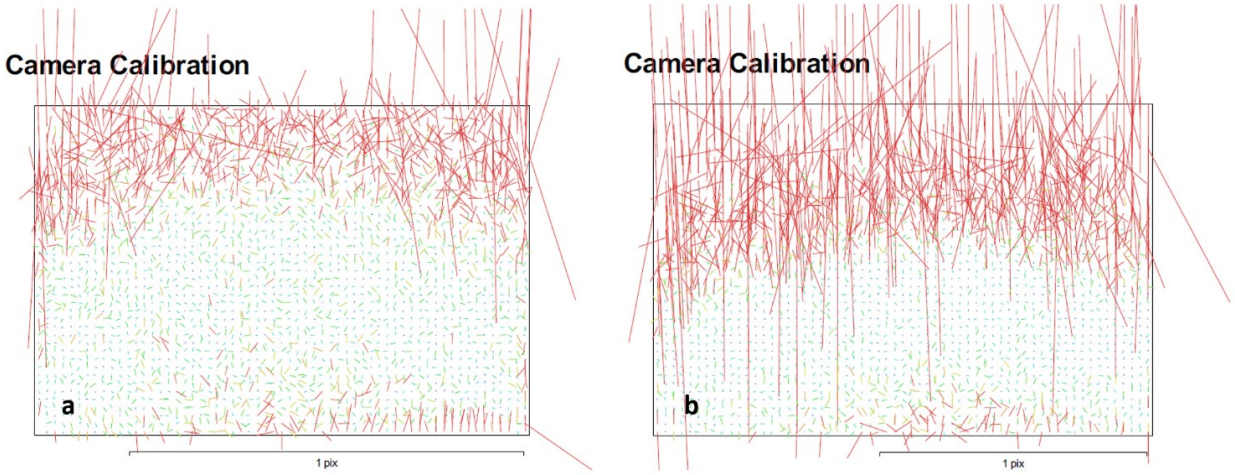

Figure 36 Image residuals on photos [pixel]: (a) Tilt angle=60°; (b) Tilt angle=30°[81].

5.4 Conclusion

What emerges from the results is that the repeatability of the software, computed according to the Eq. (5.1), and the statistical uncertainty of the 3D reconstruction follow the same trend. Although, the amount of uncertainty depends on the scanning strategy. Generally, two parameters have to be considered, Tilt Angle Value (Ψ), and the slope of the object (α). Much closer is the sum of these two parameters to 90°, better is the reconstruction, otherwise bad results could be obtained. Values of standard uncertainty lower than 1 micrometre were observed for the best configurations while greater values were registered for the worst configurations, but anyway, lower than 10 micrometres.
Even though results obtained refers to a specific case, a general conclusion could be drawn: the repeatability of the software affects the photogrammetric reconstruction in a negligible way if the choice of the scanning strategy such as tilt angle value and number of images are made considering the sample geometry and the depth of field behaviour.

Chapter 6 - Staircase reference artefact

In this chapter, the implementation of a 3D reference object, in the form of a staircase artefact, for the estimation of the external orientation, *scale adjustment*, and for the uncertainty assessment, *calibration*, is reported. The effectiveness of this reference artefact was proved through the reconstruction of the test object used in the previous chapter, the pyramidal artefact.

6.1 Materials and Methods

6.1.1 Reference object geometry

The reference object used for the external orientation computation was designed considering characteristics which aid the photogrammetric reconstruction, such as the presence of clearly visible edges and a good surface texture, where with the term “texture” the photogrammetric definition is considered.
The reference object was then designed being inspired by the one developed in [59], a staircase-like artifact, with converging steps used to calibrate a 3D SEM instrument.
It has a three-dimensional geometry with converging steps of different heights (0,25 mm, 0,50 mm, 1,00 mm). The size of the artefact (20 x 20 x 9,75 mm) was calculated according to the magnification level of the optical equipment, while the step heights correspond to the step heights of the test object used for the experiment. It was realized in steel by machining and then treated with a phosphating chemical process. Finally, 12 targets encoded at 12 bits (inner diameter equal to Ø 0,7 mm), were realized on its surface, using the laser ablation technology (*Figure 37*). The process parameters related to the laser ablation process were set by carrying out experimental tests, in order to obtain a negligible depth of ablation (equal to the thickness of the anodized layer 20 - 40 μm).

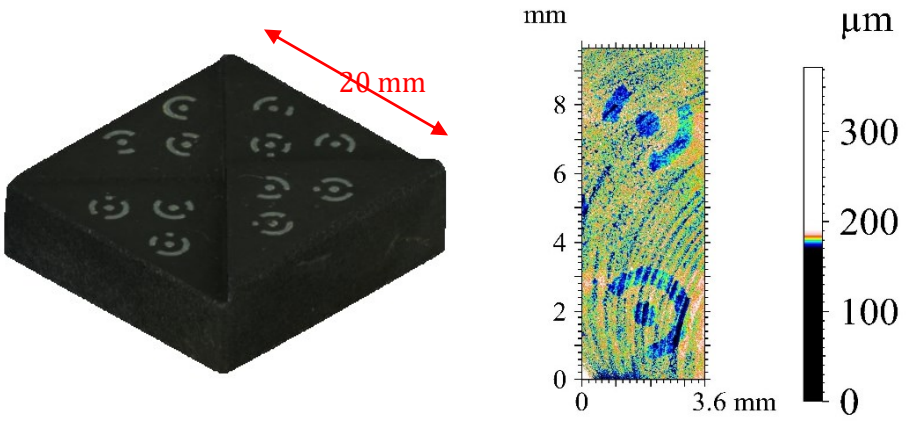

Figure 37 A 3D calibrator texturized model (a). Visualization of a surface portion with targets ablated reconstructed with a 3D optical profilometer Taylor Hobson CC-MP-HS (b) [91].

The coordinates of the coded targets etched on calibrator, were measured using a coordinate measuring machine (CMM DeMeet 400, 1.5 × magnification, MPE X = 5.33 µm, Y = 5.33 µm, Z = 4.33 µm).

6.1.2 Acquisition parameters

The image acquisition was carried out with the PSSRT equipped with a digital SLR camera Canon 40D (Effective pixels 10 megapixels), sensor size APS-C (22,2 mm x 14,8 mm), with Canon EF 50 mm 1:1:8 II lens focused to infinity and a Kenko Extension Tube of 36 mm length.

6.1.3 Measurand definition

The staircase reference object was acquired and reconstructed with the PSSRT using two geometrical configurations:

- Configuration A: Tilt Angle = 60°
- Configuration B: Tilt Angle = 30°

The dimensional analysis was carried out on bi-dimensional profiles. Each step was univocally signed and the step height values were measured for each iteration involved (*Figure 38*).

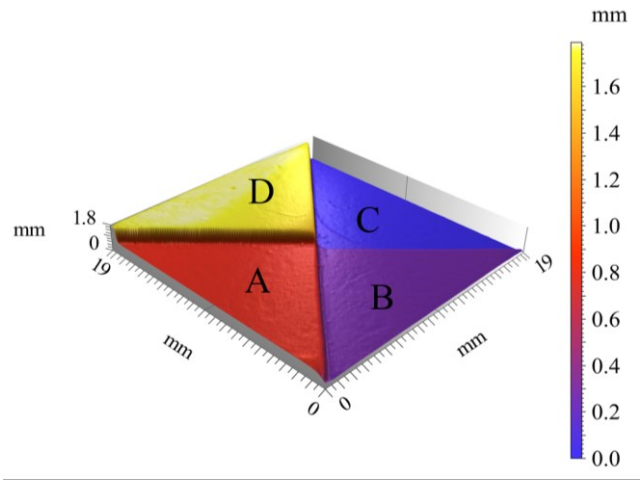

Figure 38 3D visualization of staircase artefact with steps univocally signed with letters[91].

The scanned surfaces of the artefact were analysed with TalyMap software. For each model, four profile series were computed, one series for each step. The average profile derived from 15 profiles was then analysed and the step height measured according to the standard ISO 5436-1 [93], which allow to avoid errors due to the rounding of the corners and just 1/3 of the step width is used during the analysis.
In order to estimate the bias of the photogrammetric system, associated to the staircase artefact, a reference model of the artefact was obtained using a Taylor Hobson CC-MP-HS Optical profiler, with a 20x lens mounted and an optical resolution of 1 μm. Results are reported in *Table 5*.

Table 5 Calibrated values of the staircase artefact

Step	Measurement Unit	Nominal Value	Calibrated Value
AB	mm	0,500	0,474
AD	mm	1,000	0,893
CD	mm	1,750	1,582
BC	mm	0,250	0,256

6.1.4 Experimental plan for scale adjustment procedure

With the aim to evaluate if and how the geometry of the reference object effectively improves the performance of the adjustment procedure already introduced in [70], a pyramidal artefact, used as test object, was reconstructed.
For the purpose a three-factors at two levels factorial plane (2^3) was designed and carried out. For each scanning condition of the experimental plan, three acquisitions were collected and executed in a random order. *Figure 39* shows the test object with colored height levels.

Test object

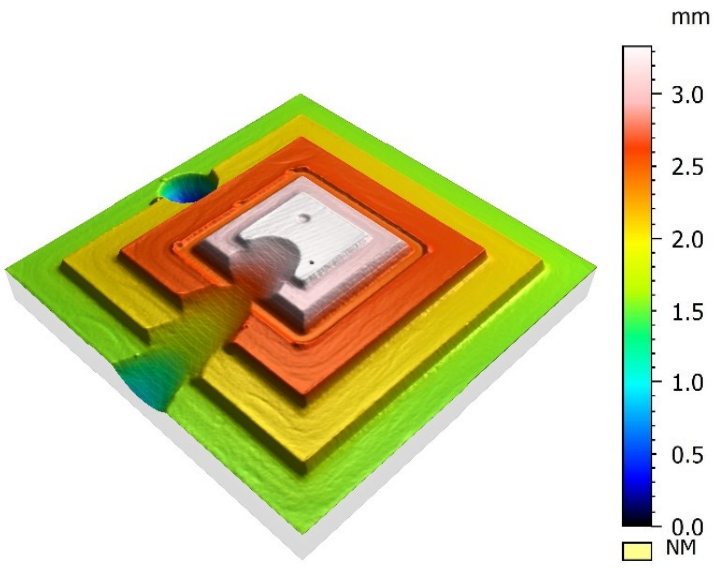

Experimental plan

Factors	Low level	High level
X_1 – Tilt Angle [deg]	30°	60°
X_2 – N_Images	18	72
X_3 - Autocalibration	yes	no

Figure 39 Pyramidal test object and experimental factors of the two-level full factorial design.

The three factors chosen were: camera tilt angle X_1, number of images X_2 and the use of internal parameters automatically estimated during the alignment process or the use of internal parameters estimated during the calibrator processing. The factor N_Images is determined by the angular step of the rotary table and it affects the overlapping level between the acquired images.
The first two factors, and their related levels (high and low), were the same investigated in [70]. The third factor was chosen to investigate if it could be better to use also fixed internal parameters, e.g., focal length, principal point coordinates, previously computed during the reference object processing, or the autocalibration, where these parameters are computed based on the picture of the test object. In order to highlight the effects of the factors influencing the process, factors not involved in the factorial plane were kept constant.

6.1.5 Uncertainty evaluation

A calibration procedure has to be accompanied with an uncertainty assessment. In order to quantify the uncertainty of the PSSRT related to the staircase artefact, the uncertainty components were estimated according to the approach proposed by the GUM (ISO/IEC Guide 98-3 – "Guide to the estimation of uncertainty in measurement").
Starting from the single standard uncertainty components, a combined uncertainty and then an expanded uncertainty with a coverage factor, k=2, which means a confidence level of 95%, was estimated. The uncertainties sources chosen for this case study are the following:

- Procedure reproducibility $\mathbf{u_p}$
- Resolution of the system, $\mathbf{u_{res}}$
- Influence of the workpiece, form errors, $\mathbf{u_w}$
  - Roughness Rz, $\mathbf{u_{w1}}$
  - Flatness Error $\mathbf{u_{w2}}$

In [94] the uncertainty component (type A) due to the software algorithms repeatability during the alignment phase, was analyzed for the operating mode implemented in this investigation. What was found is that this component was negligible in most cases, but it could become significant, (in the order of few micrometers) just if the acquisition conditions, in terms of sensor tilt angle or overlapping level, were not favorable in relation to the test object geometry. In this investigation, it was considered negligible. The expanded uncertainty *(U)* was computed according to the Eq. (6.1).

$$U = k * \sqrt{u_p^2 + u_{res}^2 + u_w^2} \tag{6.1}$$

6.1.5.1 Procedure reproducibility (u_p)

The first uncertainty component computed on the staircase artefact is the standard uncertainty due to the procedure reproducibility which is a type A uncertainty component, see Eq. (6.2).

$$u_p = \frac{S_y}{\sqrt{n}} \tag{6.2}$$

Where:

- S_y is the experimental standard deviation calculates as the square root of the variance;
- n is the number of observations, or, in this case, the number of iterations of each set;
- y is the value of measurand.

Results from the computation of the procedure reproducibility is reported in *Table 6*.

Table 6 Step height measurements.

	Configuration A				Configuration B			
Step	**CD**	**AC**	**AB**	**BD**	**CD**	**AC**	**AB**	**BD**
Average (y) [mm]	1,583	0,887	0,483	0,257	1,583	0,887	0,484	0,253
St. Dev.[mm]	0,0003	0,0014	0,0006	0,0011	0,0021	0,0026	0,0027	0,0005
N- iterations	3	3	3	3	3	3	3	3
u_p (y) [mm]	0,0002	0,0008	0,0003	0,0007	0,0012	0,0015	0,0015	0,0003

6.1.5.2 Uncertainty due to resolution of the system (u_{res})

The component related to the measuring instrument considered was the resolution of the system in the form of *ground sampling distance* GSD, which is distance between two adjacent pixel centres measured on the ground, Eq. (6.3).

$$\text{GSD}\left[\frac{\text{mm}}{\text{pixel}}\right] = \frac{\text{Flying Altitude[mm]}}{\text{Focal Lenght[mm]}} * \text{Pixel size[mm/pixel]} \qquad (6.3)$$

The value computed in this case was 0.0081 mm. Generally, the resolution is considered to have a rectangular distribution, Eq. (6.4).

$$u_{res} = 0.29*\text{GSD} = 0.00235 \text{ [mm/pixel]} \qquad (6.4)$$

6.1.5.3 Uncertainty related to form error (u_w): roughness and flatness error

The uncertainty component associated with the influence of the workpiece (u_w), contributes to the expanded uncertainty. Form error is composed by several elements; in this case, roughness (u_{w1}) and flatness error (u_{w2}) were considered.
The Rz parameter was considered for each step's surface and computed according to the ISO 4288 [95], (cut off filter of 0.8 mm). The roughness measures were performed with a non-contact 3D optical profiler Taylor Hobson CC-MP-HS 20x lens (optical resolution equal to 1 μm) which is also the reference instrument considered. The average Rz value registered was 11.38 μm, with a standard deviation of 0.189 μm. The Rz value was considered to have a rectangular distribution.
Moreover, flatness error was also evaluated and a rectangular distribution considered.

6.2 Results

6.2.1 Scale adjustment procedure with the 3D staircase reference object

As result, 24 3D models of the test object were obtained in the form of texturized meshes.
3D comparisons (*Figure 40*) were carried out between the photogrammetric models and the gold standard realized with a scanner based on the conoscopic holography principle with a "Conoprobe Mark 3.0 HD" sensor mounted and 50 mm lens that allow to perform 3D measurement with 2 mm working range, measurement errors of 0,0025 μm and repeatability 3σ of 0,0005 μm.
Results from the 3D comparisons showed that the scale adjustment obtained with a 3D reference object led to a general improvement if compared with the same methodology implemented in [70] with a bidimensional reference object. An improvement was registered, in terms of average error and standard deviation, even in those cases penalized when a bidimensional pattern was used. Best results were obtained with the 60° tilt angle configuration with average errors of about 0,005 mm and standard deviation less than 0,002 mm.

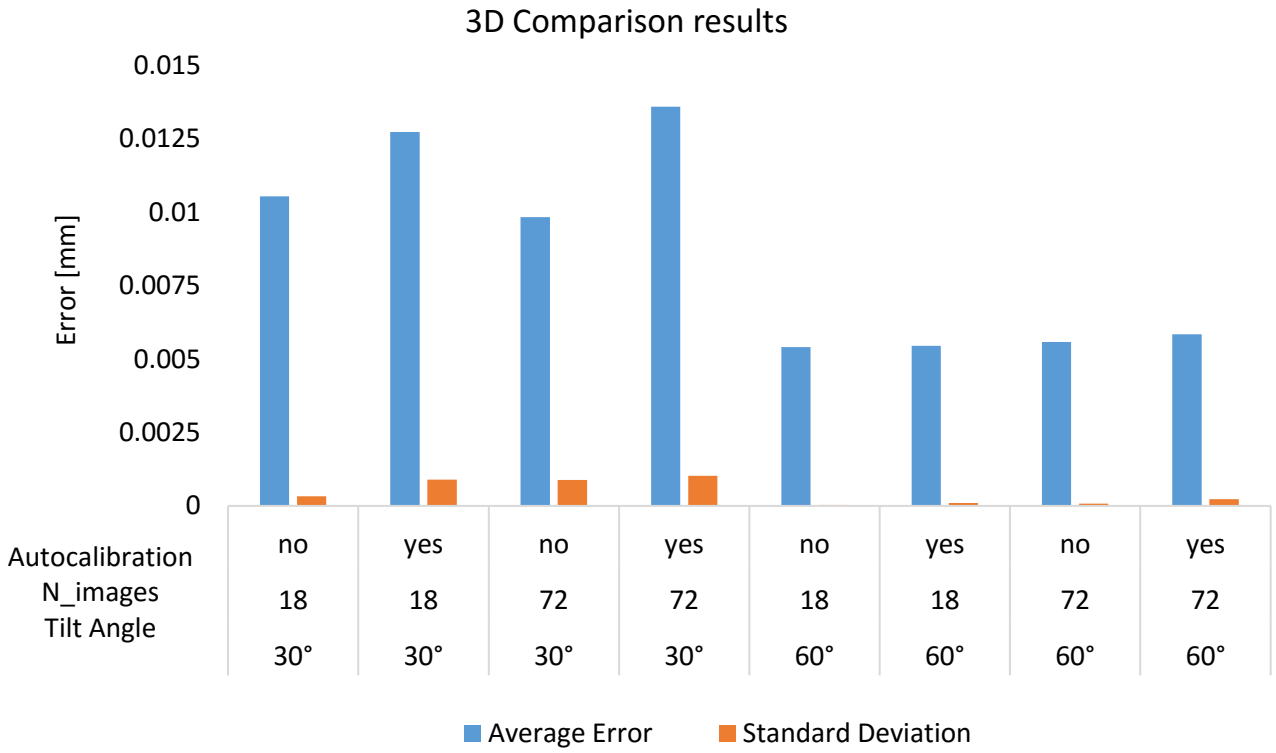

Figure 40 3D comparisons results: average error and standard deviation respect to the reference model obtained with Optimet Conoscan.

To confirm the remarks made, the factorial plane used, see *Figure 39*, was analysed to identify which factors had the main effect on the response variables chosen and which were the interactions between them. With this aim, as response variable, the average error, computed in the 3D comparisons with the reference model, was selected.

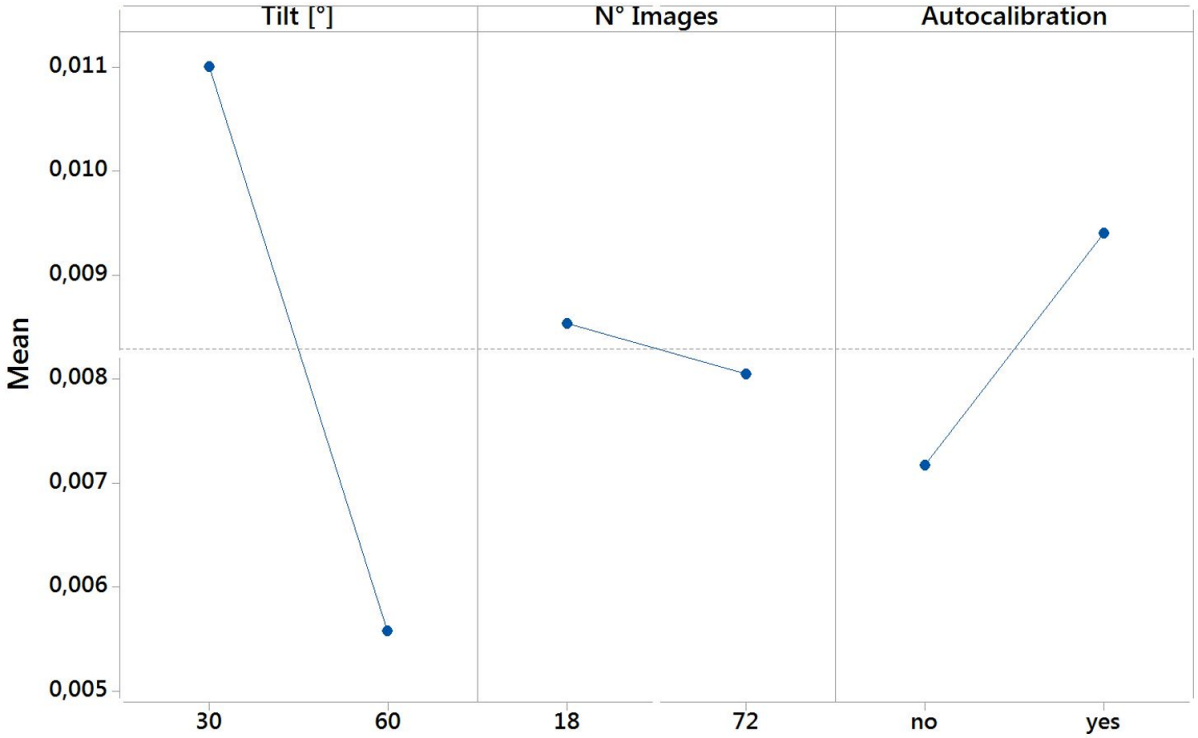

Figure 41 Main Effect Plot. Factors X1: Tilt Angle [°], X2: N° Images, X3: Autocalibration; Response variable: Average Error [91].

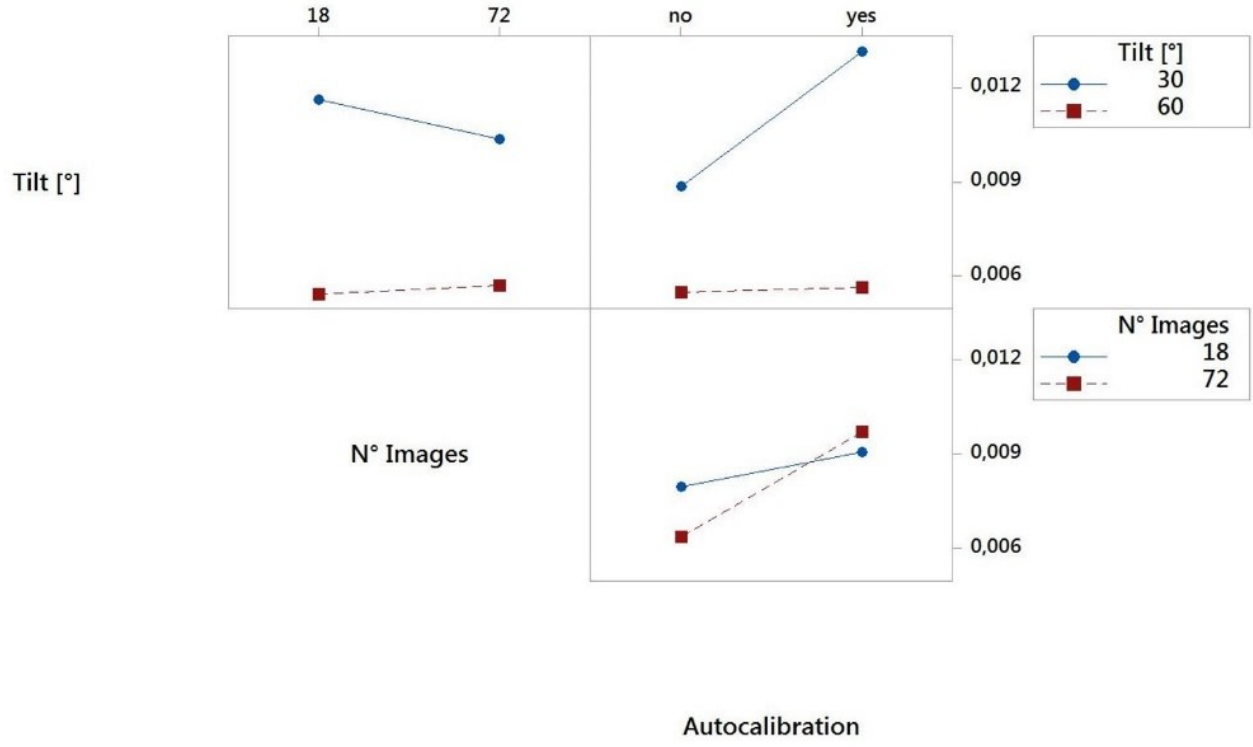

Figure 42 Interaction Plot. Factors X1: Tilt Angle [°], X2: N° Images, X3: Autocalibration; Response variable: Average Error [91].

According to the *Main Effect Plot* reported in *Figure 41*, factors, which mostly affect the error, are Tilt Angle value and Autocalibration, while the number of images (X_2) resulted to be uninfluent

in the range of the adopted values. From the *Interaction Plot*, see *Figure 42*, it was also possible to detect how the interaction of the factors acted. If the tilt angle is set to the high value, the N of images is un-influent, but if tilt angle is set to the low value, it becomes more influent. Same consideration could be done for the Tilt Angle and the Autocalibration parameters.
However, even in the configurations with the tilt angle set to 30°, results were greatly improved if one considers that the blind hole (ø3,0 mm and 2,0 mm depth), involved in the comparison, is very difficult to acquire with a low tilt angle value. In *Figure 43*, the same graph reported in *Figure 40*, was proposed excluding from the comparison the above mentioned blind hole. The difference between the two configurations were greatly reduced.
With both step angle values (18-72 - number of images) the scale adjustment obtained with the 3D reference object, resulted to be robust and effective, unlike the case of bidimensional pattern of targets used in previous tests. The highest deviations obtained in the 3D comparisons correspond to the vertical sides of the sample. The conoscopic holography technology, used to scan the pyramidal artefact, cannot detect points over a certain limit of slope because the laser beam is orthogonal respect to the xy plane (tilt angle value 90°). Otherwise, photogrammetric methodology allows to reconstruct vertical sides thanks to the possibility to use tilt angle value different from 0° and 90°.

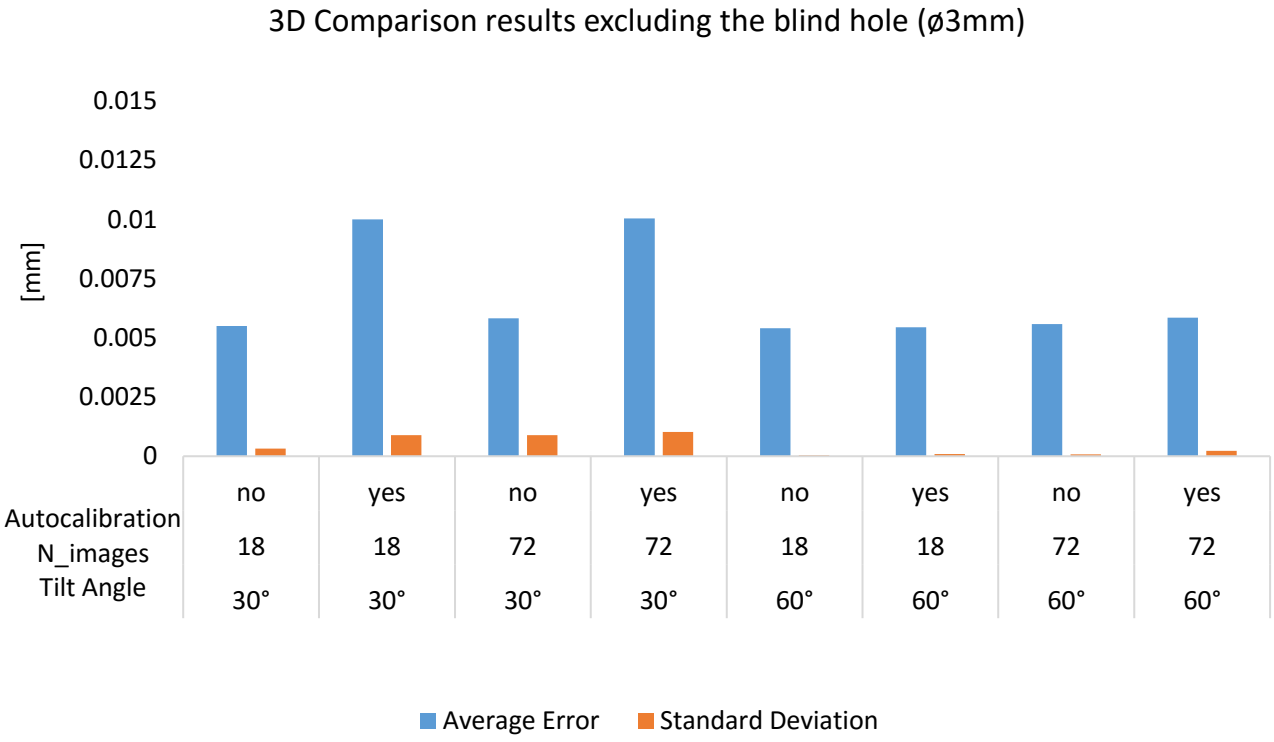

Figure 43 3D comparison results obtained excluding the blind hole.

6.2.2 Calibration procedure

The measurement bias, evaluated as difference between the measures carried out with the PSSRT and the same measures carried out with the reference instrument, (Taylor Hobson CCI-MP-HS Optical profiler), was found to be less than 0,01 mm in all cases analysed, independently on the Tilt Angle value used during the image acquisition (*Table 7*).

Table 7 Bias of the photogrammetric system respect to the reference.

Step	Measurement Unit	Calibrated Value	Measurement bias	
			Conf. A	Conf. B
BC	mm	0,256	0,008	0,008
AB	mm	0,474	-0,006	-0,005
AD	mm	0,893	0,001	0,001
CD	mm	1,581	0,001	-0,004

Moreover, the uncertainty contributors, were calculated and the resulting expanded uncertainty (confidence level 95%, K=2) reported in *Table 8*. The standard uncertainty due to *procedure reproducibility* represented the smallest component of the combined uncertainty, which means a good reproducibility of the reconstruction process; while the most influential components (about the 80% of the whole combined uncertainty), were related to the instrument limit, in terms of resolution component, and to the object, in terms of form errors.

Table 8 Uncertainty budgets obtained for the two main configurations involved.

		Configuration A				Configuration B			
		CD	**AC**	**AB**	**BD**	**CD**	**AC**	**AB**	**BD**
Average Value (y)	mm	1,583	0,886	0,483	0,257	1,583	0,887	0,483	0,252
Procedure reproducibility.- $u_p(y)$	mm	0,0002	0,001	0,0003	0,0006	0,0012	0,0015	0,0015	0,0003
Resolution u_{res}	mm	0,0024	0,0024	0,0024	0,0024	0,0024	0,0024	0,0024	0,0024
Roughness u_{w1}	mm	0,0033	0,0033	0,0033	0,0033	0,0033	0,0033	0,0033	0,0033
Flatness error u_{w2}	mm	0,0014	0,0014	0,0014	0,0014	0,0014	0,0014	0,0014	0,0014
Combined Uncertainty $U_c(y)$	mm	0,0043	0,0044	0,0043	0,0044	0,0045	0,0046	0,0046	0,0043
Expanded Uncertainty U(y)–k=2	mm	0,0086	0,0088	0,0087	0,0087	0,0089	0,0091	0,0091	0,0086
Relative Uncertainty U(y)/y	%	**0,54%**	**0,99%**	**1,78%**	**3,38%**	**0,56%**	**1,03%**	**1,89%**	**3,41%**

The uncertainty assessment carried out on the reference object could be transferred to the test object, if an adaptation of the ISO 15530-3 is considered, however, the similarity requirements must be considered. In this case, the similarity is limited to the dimensions, but even though the material is different, steel the reference object and aluminium the test object, the texture, according to its definition in the photogrammetric field, is favourable for both artefacts with comparable form errors.

6.3 Conclusion

In this chapter, the implementation of a 3D reference object was presented. The usage of the artefact was double: the scale adjustment of the PSSRT through the estimation of the external camera orientation, and its calibration with an uncertainty assessment. The scale adjustment effectiveness was proved by reconstructing a pyramidal test object. The calibration procedure was carried out to characterize the photogrammetric instrument in terms of measurement uncertainty and it can allow to transfer traceability from the calibrated artefact to the test object (pyramidal object), specifically for the configuration of the system and limited to the verification of the similarity requirements. Numerically, with the system adopted, an expanded uncertainty values less than 0,01 mm were registered for both configurations involved, taking into account that the 80% of the expanded uncertainty obtained was attributable to the roughness and flatness error.

Chapter 7 - Preliminary tests carried out through a customized free form physical standard

In this chapter the PSSRT, equipped as in the previous chapters, was tested through a customized free form physical standard. The artefact was a prototype realized scaling the original artefact developed by the NPL Institute (150x150x40 mm^3). The artefacts were manufactured with additive technologies to explore the capability of the photogrammetric system to reconstruct free form geometries. Results must be considered as preliminary, due to the texture of additive manufactured parts, which made difficult to conduct a reliable dimensional verification.

7.1 Materials and methods

7.1.1 NPL Artefact

The NPL freeform artefact, see *Figure 44*, features both concave and convex forms of various sizes and it is realized with highly reflective material, 6082-T6 – Aluminium Dural, with the aim to identify the weaknesses of optical-based systems [79]. The surface roughness, indicated with Rz and considered in the uncertainty evaluation is 0,6 μm, further below the resolution of the majority of industrial optical-based systems.
The artefact includes also four ceramic spheres mainly used for defining the reference system.

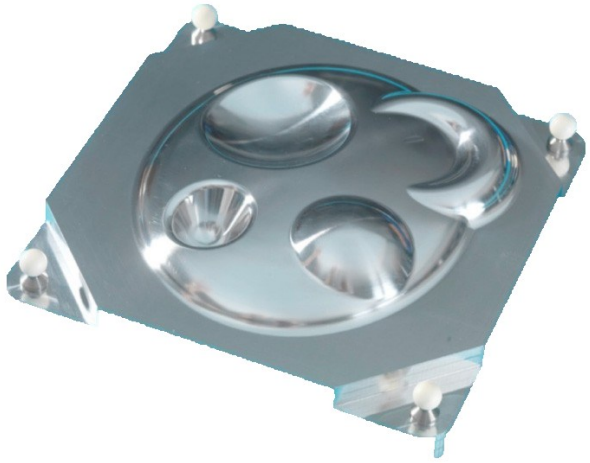

Typical calibration and measurement uncertainty for an NPL-WP-150 standard, expressed as an uncertainty (k = 2)	
Four corner reference features	
Diameter	< 1.0 µm
Position	< 2.0 µm
Three spheres in surface	
Diameter	< 4.5 µm
Position	< 2.5 µm
Cone	
Included Angle	< 0.0001 °
Diameter	< 1.5 µm
Position	< 2.0 µm
Torus	
Major Diameter 1	< 1.5 µm
Minor Diameter 2	< 1.5 µm
Position	< 2.0 µm
Points cloud of surface (150 x 150 grid)	
Position	< 2.5 µm

MATERIAL	6082-T6 – Aluminium Dural
ROUGHNESS (RZ) [µM]	0,6

Figure 44 Original NPL artefact description.

In order to use the NPL artefact for the photogrammetric scanning system under exam, it was ri-dimensioned and scaled with a ratio 1:8 starting from the original dimensions of the NPL 150 (150x150x40 mm^3). The main dimension "150" is the distance between the centres of two ceramic spheres. The resulting artefact, see *Figure 45*, had the characteristic distance between centres of the ceramic spheres 18,75 mm instead of 150 mm, in order to cover the working volume of the configuration with M=0,7x and ground resolution 0,0086 mm.

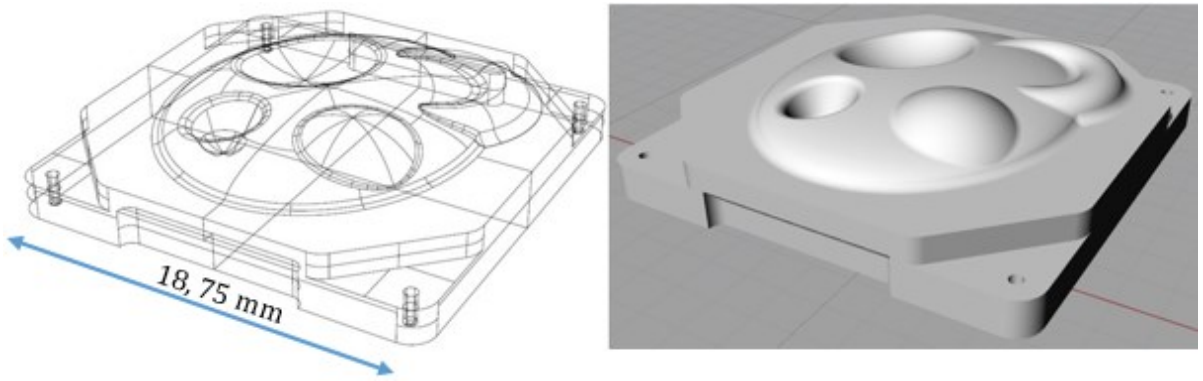

ID SPHERE	Centre (X) [mm]	Centre (Y) [mm]	Centre (Z) [mm]	Diameter [mm]
C1	0,000	18,750	0,000	0,625
C2	18,750	18,750	0,000	0,625
C3	18,750	0,000	0,000	0,625
C4	0,000	0,000	0,000	0,625
S5	6,249	12,499	6,249	10,622
S6	12,499	6,249	-0,625	8,124
S7	6,249	4,999	1,681	2,499

Figure 45 Main dimensions of the NPL artefact adaptation with 18,75 mm of characteristic distance.

7.1.2 Test objects realization through additive manufacturing techniques

The artefacts used for this investigation were realized through additive manufacturing techniques, see *Figure 46*. The first artefact was realized with DLP (Digital Light Processing) using a photosensitive resin, Maker Juice SF with 18-35°C of working temperature) and layer thickness set to 0,0015 mm. The DLP 3D printer was a Make X M-One.
The FDM artefacts were realized using 3D FDM printer Zortrax M200, a layer thickness of 0,09 mm and the material was ABS of two colours, black and grey.

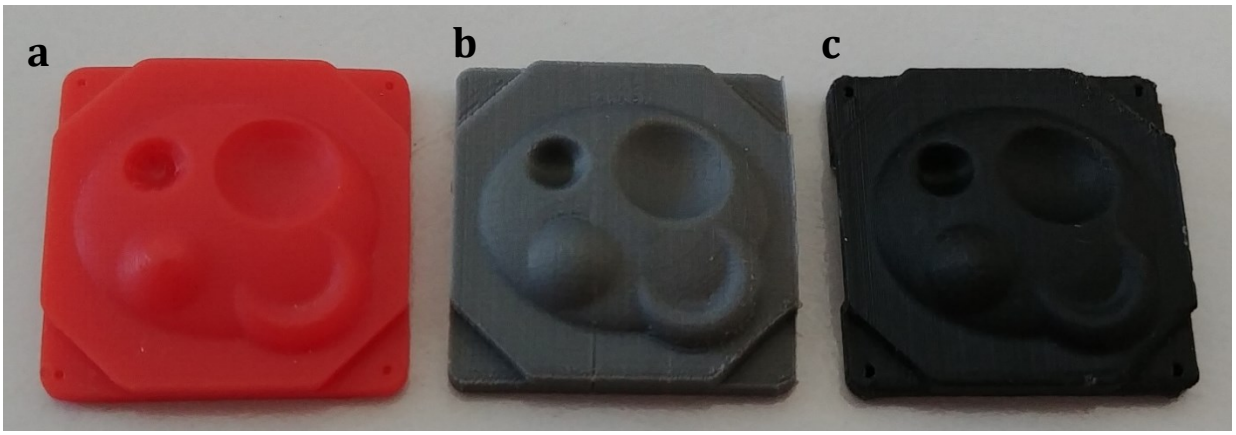

Figure 46 Customized NPL artefacts realized by DLP (a), FDM (b,c).

7.1.3 Accuracy of the manufacturing processes

In order to verify the dimensional accuracy of the 3D printed artefacts, they were measured using an optical profilometer (Taylor-Hobson CCI-MP HS) equipped with a 20x lens, to which, an optical resolution of 1 µm corresponds. From the 3D comparison between the 3D reconstruction of each artefact and the CAD model it was possible to observe how the complexity of the geometry, together with the different materials behaviour (thermal stability, humidity) affected the manufacturing process. The artefact made by DLP was found to have reduced dimensions, especially on the top, with an average deviation respect to the CAD of 0,2 mm, see *Table 9*.

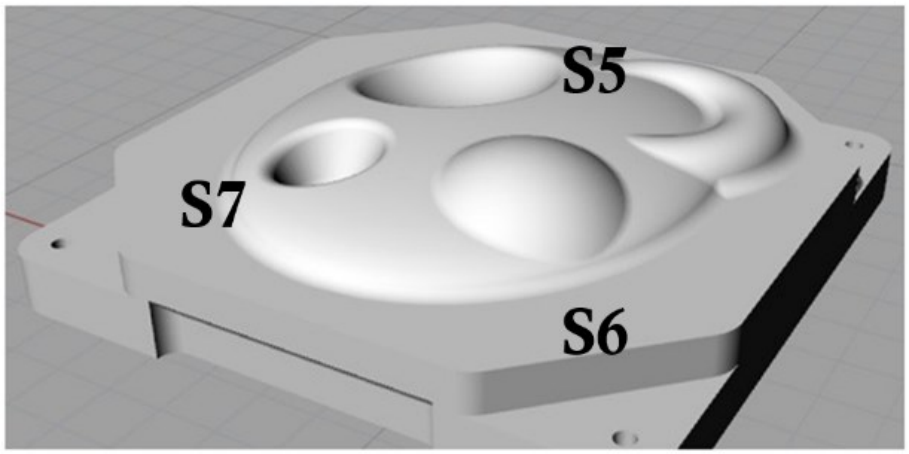

Figure 47 Sphere indexes indication on the cad model.

The feature analysis carried out on Sphere 5, 6 and 7 (the first four indexes were referred to the ceramic spheres), see *Figure 47*, highlighted manufacturing errors in the order of 10% of the nominal value. Moreover, considering the total height of the artefact, together with the number

of slices necessary to build the sample, the difference obtained between the nominal value, 5,19 mm and the measured value, 4,95 mm, can be interpreted as the layer thickness was not really 0,015 mm but 0,0143 mm. The reason can be attributable to the inaccuracies in the axis movement, as well as, the shrinkage of the material. No further consideration can be done, due to the lack of information regarding the characterization of the photosensitive resin.

Table 9 3D comparison and feature analysis on DLP artefact with the CAD model.

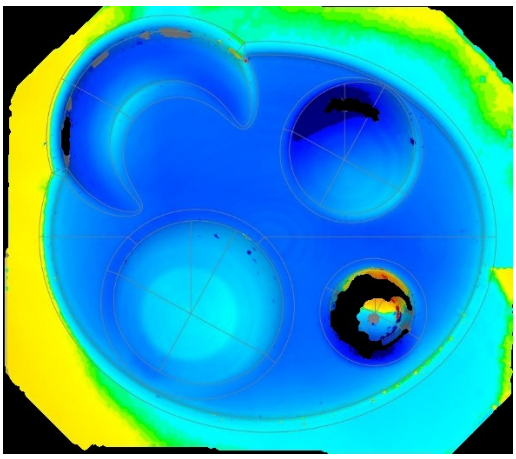

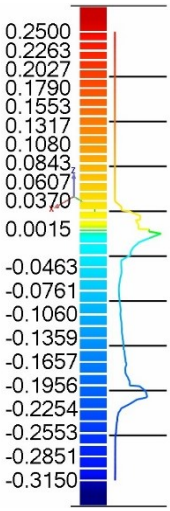

Sphere 5	Sphere 6	Sphere 7	
10,623	8,124	2,499	**Nominal value [mm]**
11,762	7,180	2,516	**Average measured value [mm]**
0,019	0,014	0,009	**Standard Deviation over 10 repetitions [mm]**
1,139	**-0,944**	**0,016**	**Average error respect to the nominal value [mm]**
10,7	*-11,6*	*0,65*	***Relative Error %***

Table 10 3D comparison and feature analysis on FDM-B artefact with the CAD model.

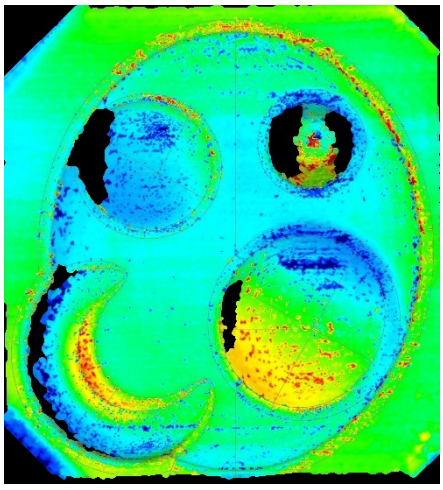

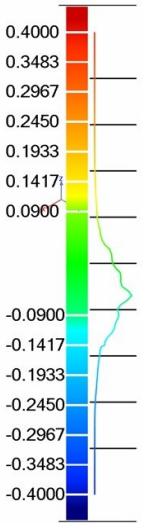

Sphere 5	Sphere 6	Sphere 7	
10,624	8,124	2,499	**Nominal value [mm]**
11,0887	8,1365	2,2842	**Average measured value [mm]**
0,0134	0,0828	0,0123	**Standard Deviation over 10 repetitions [mm]**

0,469	**0,041**	**-0,214**	**Average error respect to the nominal value**
4,3746	0,1527	-8,6202	***Relative Error %***

Table 11 3D comparison and feature analysis on FDM-G artefact with the CAD model.

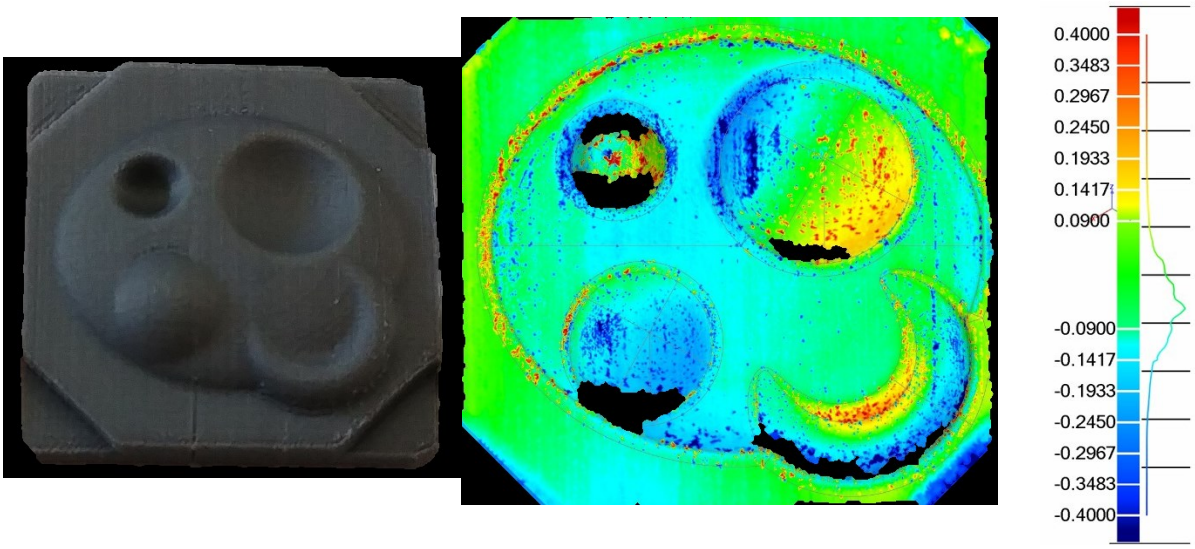

Sphere 5	**Sphere 6**	**Sphere 7**	
10,624	8,124	2,499	**Nominal value [mm]**
10,4324	8,2028	2,4943	**Average measured value [mm]**
0,0145	0,0158	0,0173	**Standard Deviation over 10 repetitions [mm]**
-0,1915	**0,0787**	**-0,0054**	**Average error respect to the nominal value**
-1,8028	0,9692	-0,2162	***Relative Error %***

The thermal expansion was also considered for ABS material. From the datasheet of the ABS supplier, the coefficient of thermal expansion (CTE) is 74×10^{-6} °C^{-1}. Considering a ΔT=5,4 °C, assuming the isotropic behaviour of the material (CTE equal in all the direction).

$$L = L_0 * \alpha \tag{7.1}$$

$$\alpha = CTE * \Delta T \tag{7.2}$$

$$\alpha\ (ABS) = CTE * \Delta T = 74 * 10^{-6} * 5{,}4 = 0{,}0004\ mm$$

with L_0 the initial length considered.

The artefacts realized by FDM registered lower errors respect to the CAD, if compared with the DLP, see *Table 10* and *Table 11*.
Due to the measuring principle of the optical profilometer, the acquisition of the vertical sides was very difficult. The structure obtained from the layer deposition, created a lack of data of few micrometres due to the typical FDM profile, see *Figure 48*.

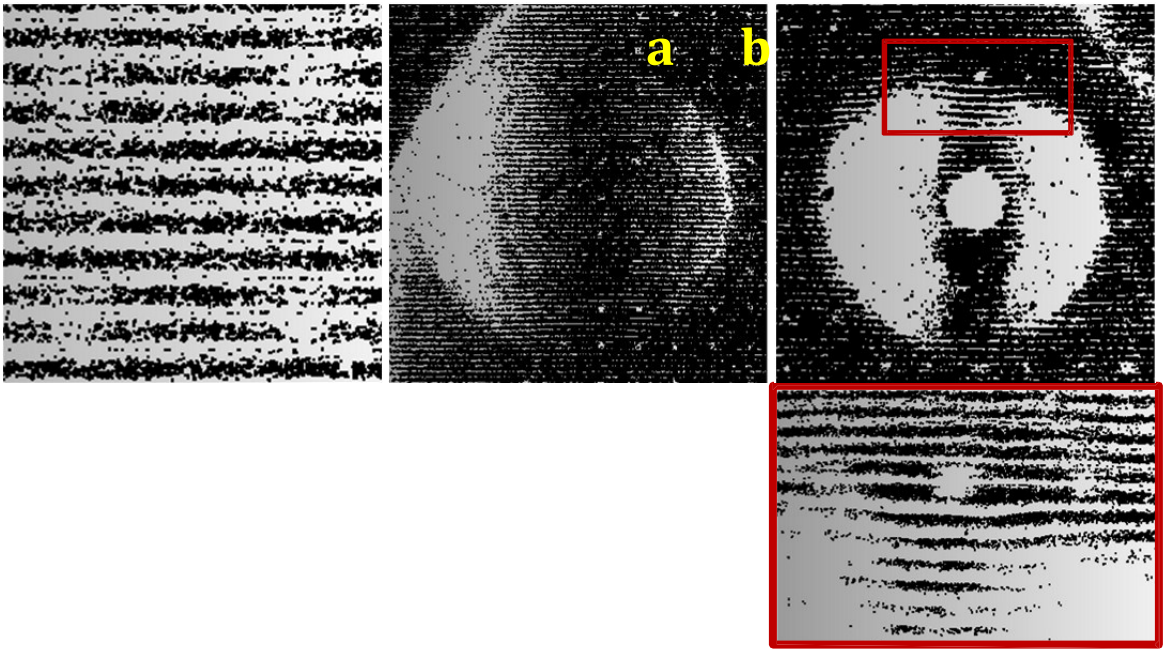

Figure 48 Close-up of the point cloud acquired with the optical profilometer in correspondence of the sphere 6(a) and 7(b).

7.1.4 Photogrammetric reconstruction of the artefacts

The photogrammetric reconstruction was carried out with the PSSRT [70]. In this case a Canon Eos 760D with a Canon EF 50 mm 1:1:8 II objective lens equipped with an extension tube of 36 mm, was used with a consequent ground resolution of 0,00545 mm/pixel. The sensor was tilted of 60° and 36 pictures were taken rotating the object with a step of 10°. In *Figure 49*, an example of the photogrammetric reconstruction of the FDM-G artefact is reported, with the computed external orientation. Five repetitions for each artefact were carried out.

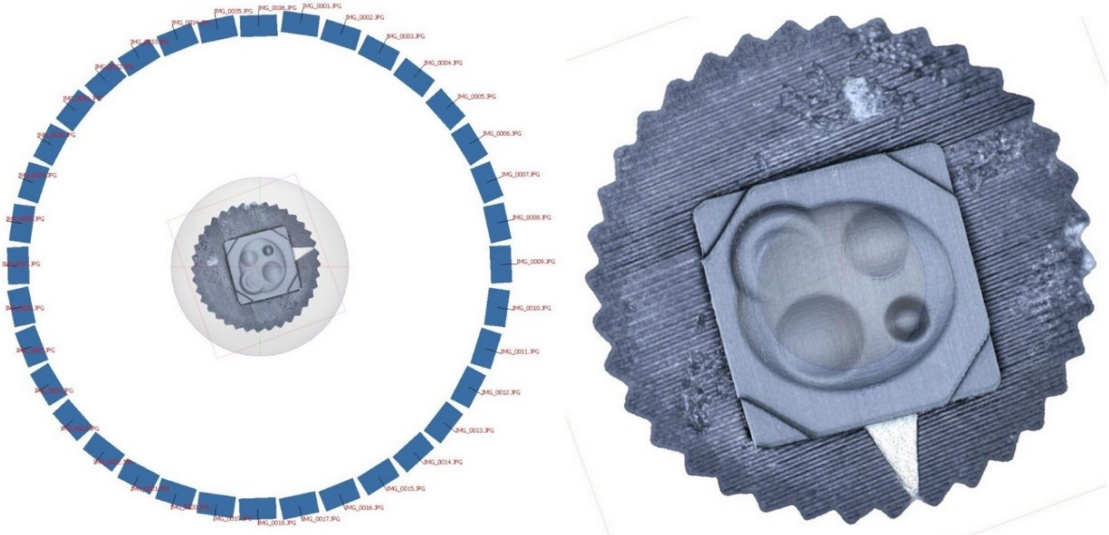

Figure 49 Photogrammetric reconstruction of the FDM-B artefact.

7.2 Results from 3D comparisons

In *Figure 50*, the 3D comparison between the photogrammetric reconstructions and the reference model are reported for the artefact made through DLP. From the coloured map obtained for the DLP artefact, the average error was found to be in the order of 0,01 mm, with a standard deviation of 0,006 mm. The higher errors were in correspondence of the steeper areas and they reached the 0,03 mm. Although, those areas are more critical for the optical profilometer chosen as reference instrument, rather than the photogrammetry.

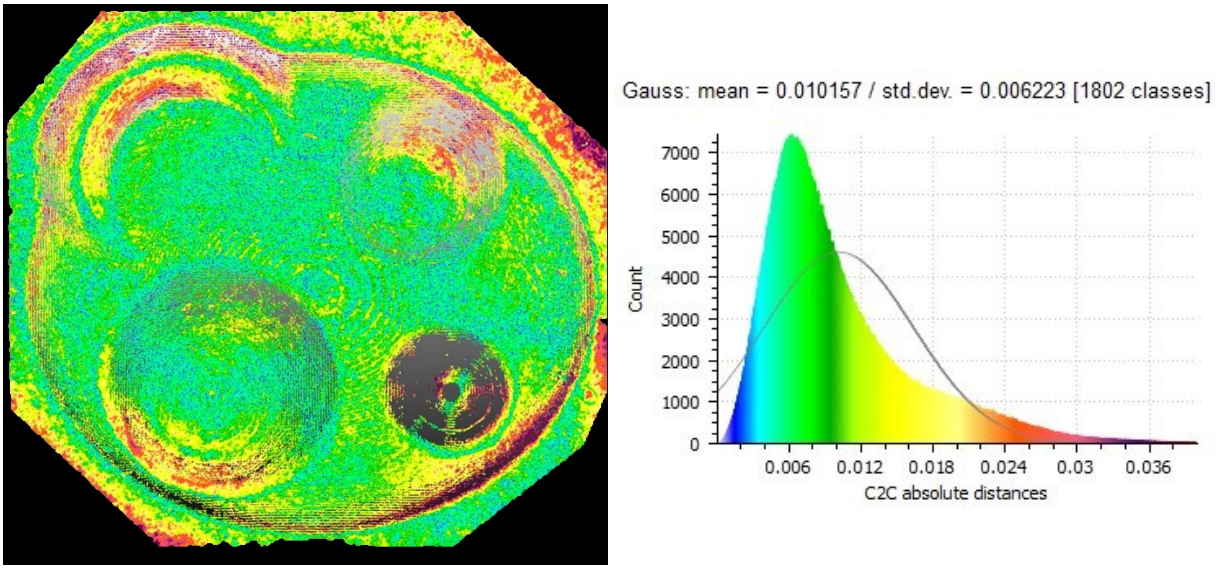

Report DLP	Average evaluated over 5 repetitions	Standard Dev.[mm]
Errors	0,0105	0,0062
Dev.Std.C	0,0001	-

Figure 50 3D comparison between the PH point cloud and the reference. Test object: DLP artefact.

Regarding the reconstruction of the artefacts made through FDM, see *Table 12*, errors in the order of 0,03 mm were registered for the FDM-B, while for the FDM-G much higher errors were registered. The average value was 0,112 mm with a standard deviation of 0,0843 mm. The reasons could be attributable to the difficulty of the reference instrument to acquire the surface, with lack of points, as well as, difficulty when registering the two point clouds for the comparison.

Table 12 Numerical results of the 3D comparisons. Test objects: FDM-B and FDM-G.

Report FDM-B	Average (5 repetitions)	Standard Dev.
Errors [mm]	0,03275	0,030738
Dev. Standard [mm]	0,03275	-
Report FDM-G	**Average (5 repetitions)**	**Standard Dev.**
Errors [mm]	0,11068	0,0843118
Dev.Std.C [mm]	0,00273	-

7.3 Feature Analysis

The feature analysis was conducted in two ways:

- the RANSAC algorithm for shape detection embedded in Cloud Compare [96];
- the best fit algorithm embedded in Geomagic Control software [97].

Firstly, a RANSAC analysis was carried out. The RANdom SAmple Consensus (RANSAC) algorithm, proposed by Fischler and Bolles [98], is a general approach very useful for extracting information from a very huge set of input data, with a large proportion of outliers. Indeed, due to the increasing size and complexity of digitized geometry acquired with optical techniques there is an ever-growing demand for concise and meaningful algorithms for analysing this data. RANSAC, developed within the computer vision community, is a resampling technique that generates candidate solutions by using the minimum number observations (data points) required to estimate the underlying model parameters. Unlike conventional sampling techniques, that use the maximum amount of data available to obtain an initial solution and then proceed to eliminate outliers, RANSAC uses the smallest set possible and proceeds to enlarge this set with consistent data points.

In *Figure 51*, an example of feature extraction on the customized NPL artefact is proposed.

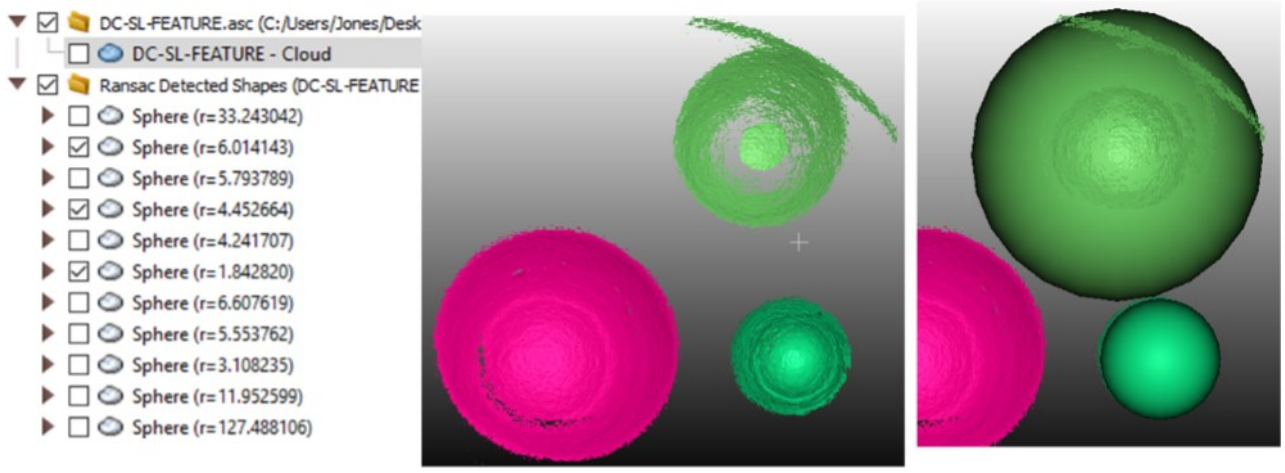

Figure 51 Example of feature detection with RANSAC in Cloud Compare.

7.3.1 Results with RANSAC

Results obtained with RANSAC referred to the DLP, see *Table 13* artefact and the FDM-G, see *Table 14*. A correct analysis on the FDM-B was not possible due to the lack of data in the reference point cloud, which made impossible the success of the shape detection algorithm RANSAC.

Table 13 Ransac analysis results on DLP artefact.

	ØS5 [mm]	ØS6 [mm]	ØS7 [mm]
PSSRT	11,954	7,274	2,511
TH	11,923	7,296	2,515

Error [mm]	0,031	-0,022	-0,004
St, Dev [mm]	0,025	0,025	0,011

Table 14 Ransac analysis results on FDM-G artefact.

	ØS5 [mm]	**ØS6 [mm]**	**ØS7 [mm]**
PSSRT	10,466	8,223	2,494
TH	10,378	8,273	2,434
Error [mm]	0,088	-0,050	0,059
St. Dev [mm]	0,0332	0,0723	0,0768

7.3.2 Results from the best fit algorithm in Geomagic

Results obtained from the *best fit* feature analysis, carried out through Geomagic software, showed higher errors, if compared to the RANSAC method. This is due to the difficulty in using the best fitting methods on the acquired surfaces. The form error due to the additive manufacturing technologies used, played a fundamental role in the dimensional verification due to the high variability of results. The form error, evaluated during the sphere fitting process, was in the order of 0,1 mm, see *Figure 52****Errore. L'origine riferimento non è stata trovata.***. The lowest value was registered for the DLP test object and it overcame 0,2 mm. These values made the dimensional analysis very difficult. Moreover, the optical profilometer used as reference did not reconstruct completely the objects surface due to the typical profiles obtained with FDM and DLP.

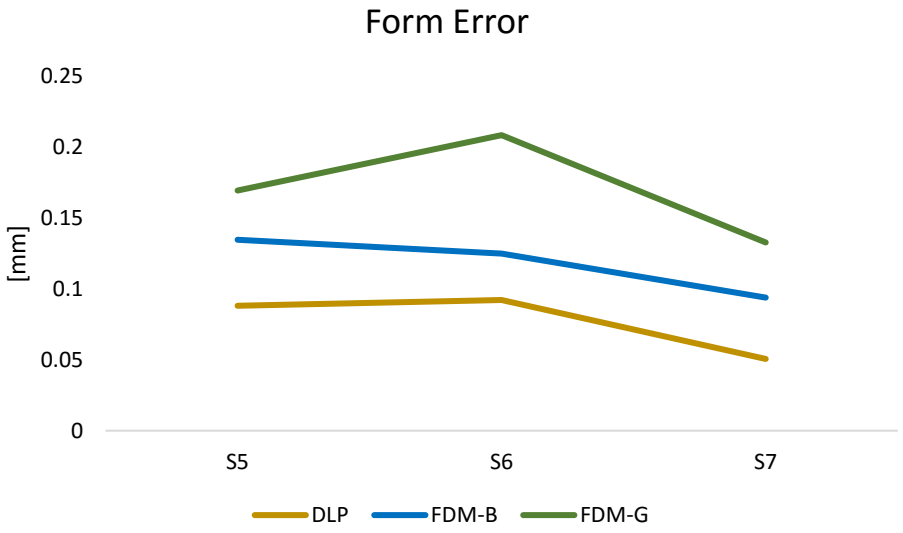

Figure 52 Form Deviation evaluated on reference model.

Figure 53, Figure 54 and Figure 55 show results obtained from the dimensional analysis on the spheres diameters and errors evaluated respect to the reference model are reported. Errors were in the order of 0,1 mm and they were mainly due to the fitting process and the variability due to the surface texture of the artefacts. Surface texture is one of the main drawbacks of the additive manufacturing technology. It affects differently every measuring instrument, contact

and non-contact, with a systematic and random effects, which need to be better understood and quantified [99].

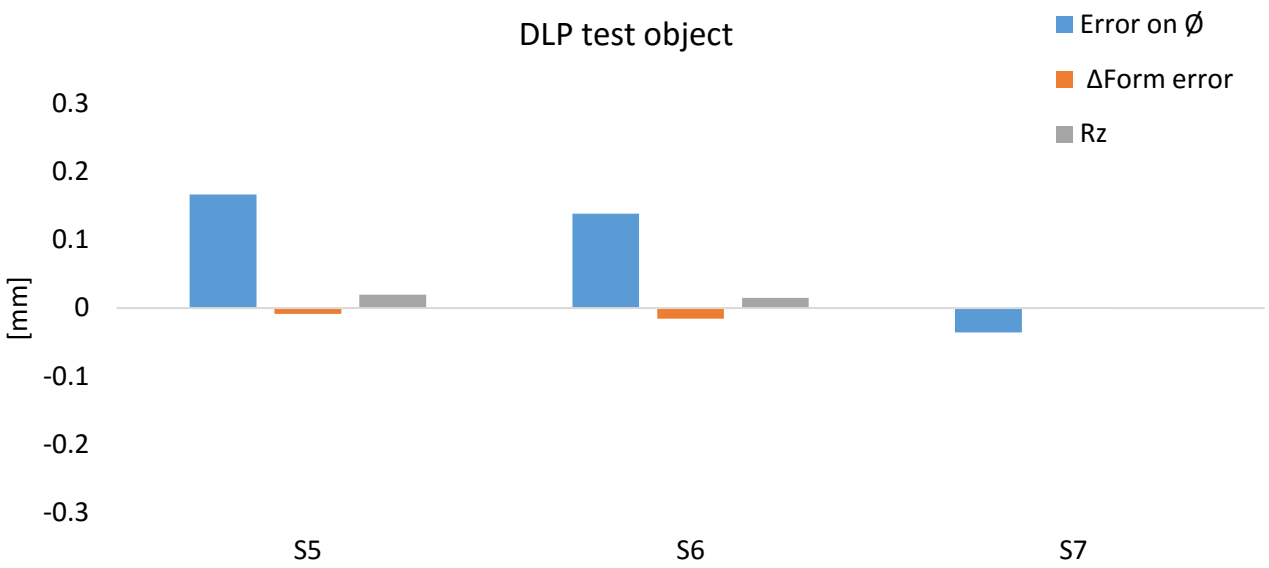

Figure 53 Errors evaluated on DLP test object.

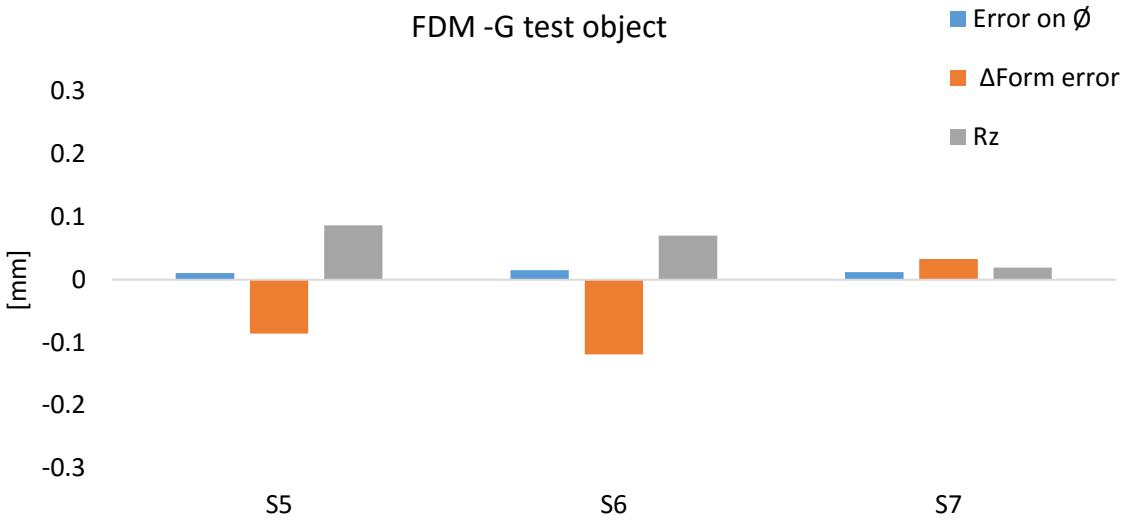

Figure 54 Errors evaluated on FDM-G test object.

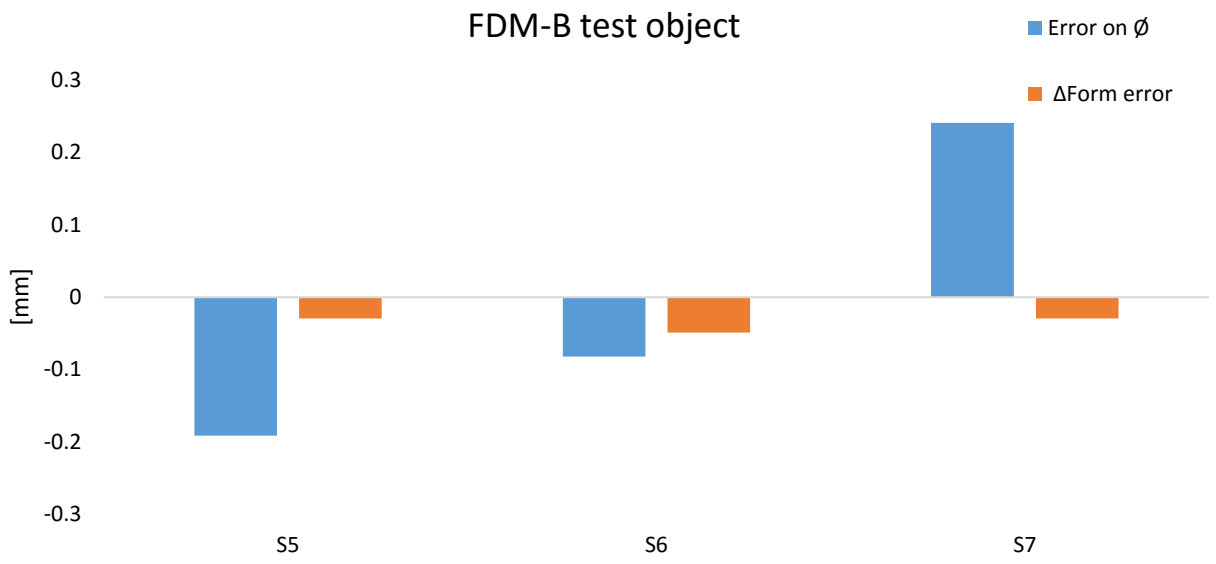

Figure 55 Errors evaluated on FDM-B test object.

7.4 Conclusion

In this chapter, preliminary tests were conducted for evaluating the capability of the PSSRT to acquire free form surfaces, through the use of a customized NPL free form artefact. The customization was necessary to resize the artefact and adapt it to the field of view of the optical equipment used in this investigation. For the purpose, additive manufacturing technologies were used, DLP and FDM. Results obtained from 3D point clouds comparisons were quite reliable with 0,01 mm of average error, while results obtained from the feature analysis, conducted with RANSAC and the best fit algorithm embedded in Geomagic, were compromised by the high form errors, which made impossible a reproducible dimensional verification. Generally, errors registered on DLP artefact were lower than errors registered on FDM artefacts, in the order of 0,01 mm. One of the main drawbacks of using additive manufactured parts is the difficulty in finding a reference model. The optical profilometer showed lack of points in many areas of the artefacts, especially the ones produced with FDM. Although, as preliminary tests, and considering the impossibility to have reliable reference models for the 3D comparison, results are promising for proceeding to the fabrication of the same reference artefact with micro-milling of Aluminium material.

Chapter 8 – Measurement of additive manufactured biomedical devices

Additive manufacturing techniques are becoming ever more present in many fields, especially the biomedical thanks to its advantages and the geometrical complexity they can reach, e.g. scaffolds for tissue engineering, dental models and 3D models to improve surgical planning.
In this chapter, the dimensional verification of microfluidic devices manufactured with additive manufacturing techniques, was conducted. The main challenge was represented by the surface texture, *visual* and *tactile*, which characterizes additive manufactured products and strongly affects the effectiveness of most of currently available 3D optical measuring instruments.
The PSSRT was used as non-destructive and low-cost technique for the reconstruction and the measurement of four 3D printed microfluidic devices. They were manufactured with Stereolitography (SLA), Fused Deposition Modelling (FDM) and Polyjet.

8.1 Materials and Method

8.1.1 Test object description

The device under exam was a micro-mixer consisting of two inlets, one outlet and a 18 channels serpentine, that are able to mix two fluids in a laminar flow to achieve mixing by diffusion, see *Figure 56*. The complexity of the micro-channels' geometry is represented by the width and depth of the single channel (0,6 mm x 0,6 mm). A concave geometry needs more light to be acquired with an image-based system but the width is small enough to complicate this task.

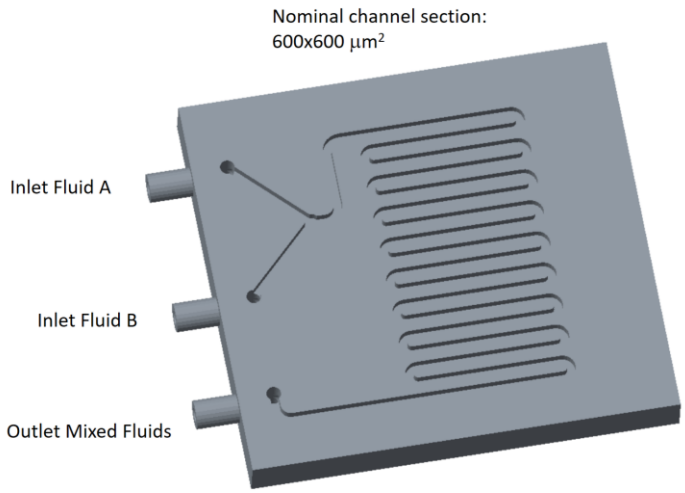

3D printer model	Printing method	Layer height (mm)	Laser spot size or nozzle diameter (mm) or resolution (DPI)	Filling or etching strategy	Type of material
Formlabs Form 2	SLA, Stereolithography	0,025	0,14	solid	Clear Form V2 UV Photopolymer Resin
Stratasys F370	FDM, Fused Deposition Modeling	0,127	0,36	raster	Stratasys ABS
Ultimaker 3	FDM-FFF, Filament Fused Fabrication	0,090	0,40	raster	Ultimaker grey PLA
Stratasys Objet 30	Polyjet process	0,028	600 DPI (X and Y axes) 900 DPI(Z axis)	solid, glossy finishing	Vero White Plus UV Photopolymeric Resin

Figure 56 3D printers, process parameters and materials used for the fabrication of the micro-fluidic devices. The analyzed AM microdevice (courtesy of Prof. Filippini).

The three technologies used for fabricating the devices, show very interesting superficial textures. In *Figure 57*, the surface of each device is shown, captured with a Hirox RH2000 digital microscope, equipped with MXB 5040RZ optics, set up to a magnification 150 x.
These images, see *Figure 57,* show the different aspect of AM surfaces, SLA is not reflective but semi-transparent, FDM is reflective (white ABS more than grey PLA), and characterized by well evident beads while Polyjet is reflective and with no evident beads.

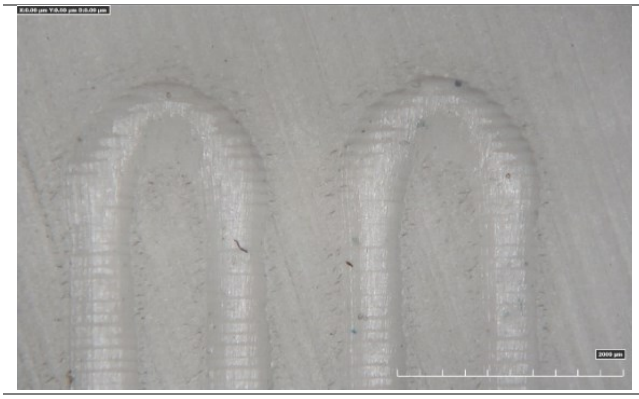

Figure 57a: Detail of the SLA device

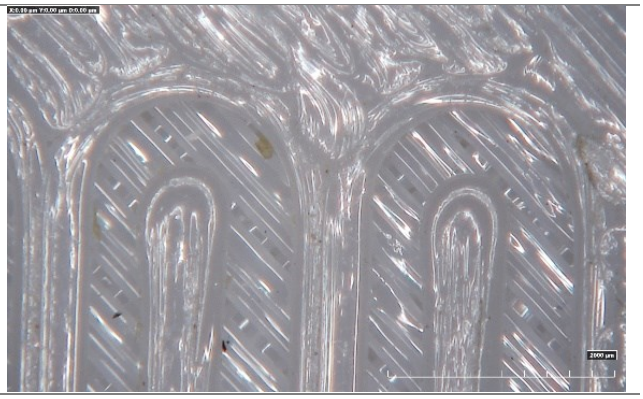

Figure 57b: Detail of the ABS-FDM device

Figure 57c: Detail of the PLA-FDM device

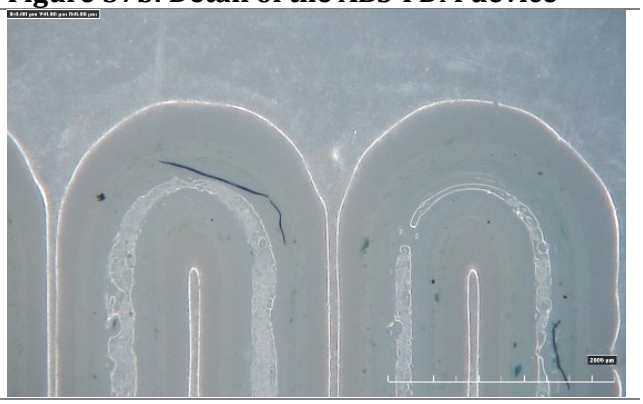

Figure 57d: Detail of the Polyjet device

Figure 57 Images captured with a digital microscope [100].

8.1.2 Measuring system set-up

The experimental phase was conducted using a full frame digital reflex camera Canon Eos 6D with a 20.2 Megapixel resolution (5472 x 3648 pixel^2) and a Full Frame CMOS sensor (36 x 24 mm^2). A Canon EF 100mm f/2,8 macro lens, with the focus distance set to its minimum value, was used with magnification ratio equal to 1:1. This set-up has an optical ground resolution of 0,0065 mm/pixel and a depth resolution of 0,0132 mm/pixel. The rotation angle of the table was set at 5°; in fact, the smoothed surfaces of the micro-mixers forced to use a high number of images with the aim to increase the number of tie points recognized in the images and then to allow the alignment and the whole reconstruction process. Finally, the camera was tilted respect to the table at 60°. This choice derived from previous experiences [70]. The smooth and reflective surfaces of at least two of the four devices represented a big challenge for the PSSRT under test. To overcome this criticality, attention was paid on the lighting conditions, considering that no projected pattern was used to create an artificial texture. With this aim, a led strip that rotates together with the turning table and the object, was chosen, so that variations of shadows and other light effects were minimized during the acquisition. In addition, and in order to avoid the influence from the environmental illumination, another white led source was placed above the camera. Moreover, each sample was scanned with a different exposure time according to its characteristics. The exposure time resulted to be a very important parameter: PLA-FDM, grey coloured, represented a challenge because the top surface and the microchannel bottom surface (darker than the top surface due to the microchannel depth) required a different amount of light and then a different exposure time. This effect was not encountered for the other samples due to the more diffusive appearance, suffering issues mostly related to reflectivity.

For the investigation, three acquisitions for each device were carried out to evaluate the statistical uncertainty due to the measuring procedure. This parameter is of great interest, mostly in this case, due to the dependence of a photogrammetric scanning system, as an optical instrument, on the environmental lighting conditions, which, together with the exposure time and the f/stop parameters, determine the quality of the final acquired image. The photogrammetric point cloud was obtained using Agisoft Photoscan Pro version 1.2.6 [87].

8.1.3 Scale Adjustment

One of the most important problems of the photogrammetric technique is the attribution of the scale to reconstructed point clouds due to an inherent limitation of the technique. In this investigation, the scaling method described in [101] was employed.
The scaling method proposed in that paper involved two parameters: the magnification level M, which is the ratio between the size of an object in the image and its true size; and the pixel size, which is a specification of the sensor used. The procedure consists of a series of subsequent steps. Firstly, two sets of photos of the workpiece must be captured, each of which, with a different diaphragm aperture. Diaphragm aperture is the parameter described by the f/stop value and it strongly affects the depth of field of the image captured. In this case, one aperture must be set to the largest value, f/2,8: a larger aperture allows for easy recognition of the area most in focus in the image. The other aperture value must be set smaller. The latter value represents the best compromise between depth of field and diffraction and it has been set to 20. Starting from at least one image obtained with the largest aperture, two markers located in the most focused area have been identified and the pixel distance measured, see *Figure 58*.
The distance in pixels is converted into millimeters through the magnification ratio M and the pixel size, according to the equations (8.1-8.5).

$$x_1[mm] = x_1[pixel] \cdot pixel\ size \tag{8.1}$$

$$y_1[mm] = y_1[pixel] \cdot pixel\ size \tag{8.2}$$

$$x_2[mm] = x_2[pixel] \cdot pixel\ size \tag{8.3}$$

$$y_2[mm] = y_2[pixel] \cdot pixel\ size \tag{8.4}$$

$$D_{12} = \frac{\sqrt{(\mathrm{x}_2 - \mathrm{x}_1)^2 + (\mathrm{y}_2 - \mathrm{y}_1)^2}}{M} \tag{8.5}$$

Where,

(x_1, y_1) are the coordinates of marker 1;

(x_2, y_2) are the coordinates of marker 2.

The pixel size refers to the lateral side of each pixel, being a specification provided by the supplier and expressed in mm/pixel; D_{12} is the Euclidean distance, expressed in millimeters, between two points indicated with number 1 and 2; M is the magnification level experimentally estimated; in square brackets the measuring units are expressed.

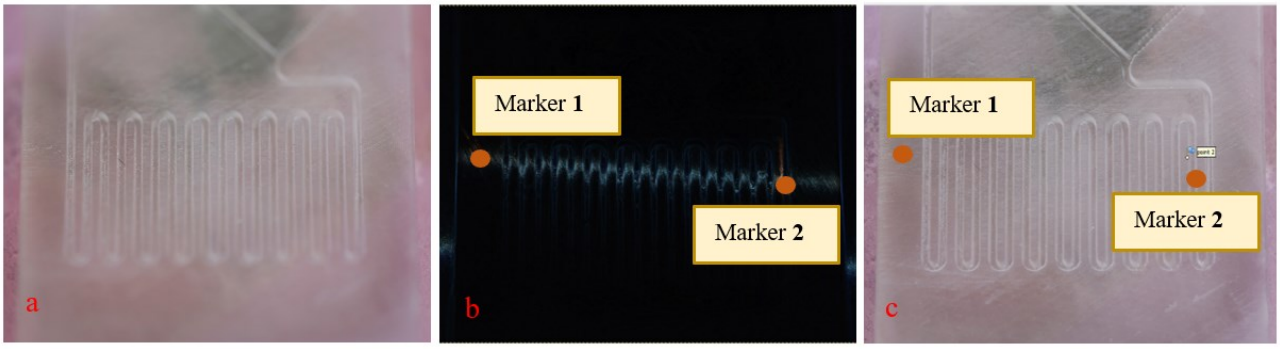

Figure 58 Scale procedure with two markers. a) image taken with f/2.8; b) image filtered to easily recognize the most focused part; c) image taken with f/20 used for the 3D reconstruction [100].

After this computation, the distance in mm were imported in the set of photographs with the smallest aperture value, which is the set of photographs that will be processed to obtain the final 3D model. This step allowed to obtain a real scaled 3D model.

8.2 Results

In *Figure 59*, the photogrammetric reconstruction of the micro-mixers realized respectively with SLA, FDM-FFF, and Polyjet is reported.
Photogrammetric measurements were compared to the point clouds obtained with the optical profilometer CCI-MP-HS TAYLOR HOBSON (TH) with a 20x magnification lens, field of view 0,8x0,8 mm^2, a resolution of 0,001 mm and a maximum slope of 17°. The global scanning time was approximately equal to 10 hours for each device. Interferometry is one of the most used techniques for the micro-channels measurement due to its capability to measure reflective and transparent objects. Although, it does not allow one to reconstruct vertical sides and the reconstructed part, after the outliers removing, has a number of points lower than photogrammetry.

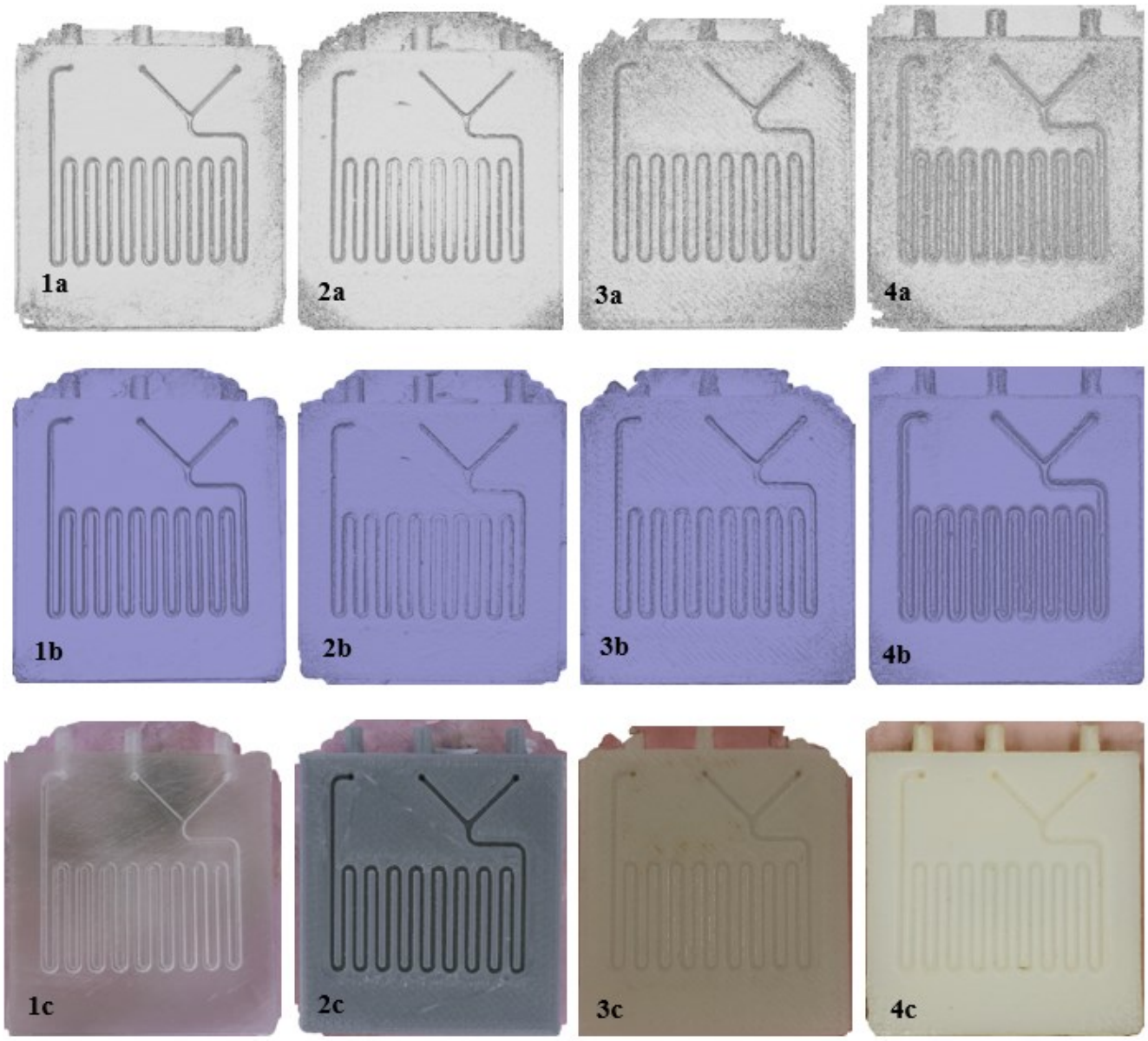

Figure 59 Devices reconstructed with photogrammetry. a) point cloud, b) mesh c) texturized mesh; SLA (1), PLA-FDM/FFF (2), ABS-FDM (3), Polyjet (4) [100].

8.2.1 Point cloud comparisons

Point cloud comparisons were carried out with open source Cloud Compare software (http://cloudcompare.org/). Comparing point clouds, which are the first output of any optical instrument, allows to avoid errors due to the approximation of mesh and to provide more accurate results. The average number of points reconstructed through the photogrammetric system depended on the sample reconstructed. The SLA and PLA-FDM registered the highest number of points equal to about 4,5 millions; while the ABS-FDM and Polyjet registered a lower number of points approximately equal to 3 millions. This is due to the smoother surface of the latter. Indeed, the number of points forming the dense cloud, is directly affected by the number of points identified during the recognition phase. In *Figure 60*, results from the 3D comparisons between the photogrammetric and the reference model (TH model) are reported in terms of

average value of absolute distances between homologous points and in terms of standard deviation (σ) evaluated over three repetitions. These results provided evidence of a lower variability of SLA measurements when compared to FDM and Polyjet. Moreover, the average deviation must be discussed: the best performance was obtained with SLA, with a low reflectivity, while the most reflective, the Polyjet had the poorest performance, although lower than 0,050mm. Reflectivity affected the difference in FDM artefacts since the grey-PLA sample is much better performing than ABS white. In every case, the performance of the photogrammetric technique, with a passive approach, is included into the interval 0,017–0,033 mm. Considering that Formlabs (SLA) declares a laser spot size equal to 140 μm, the technique demonstrated a good performance. SLA and PLA-FDM were the best candidates for dimensional verification by means of photogrammetry.

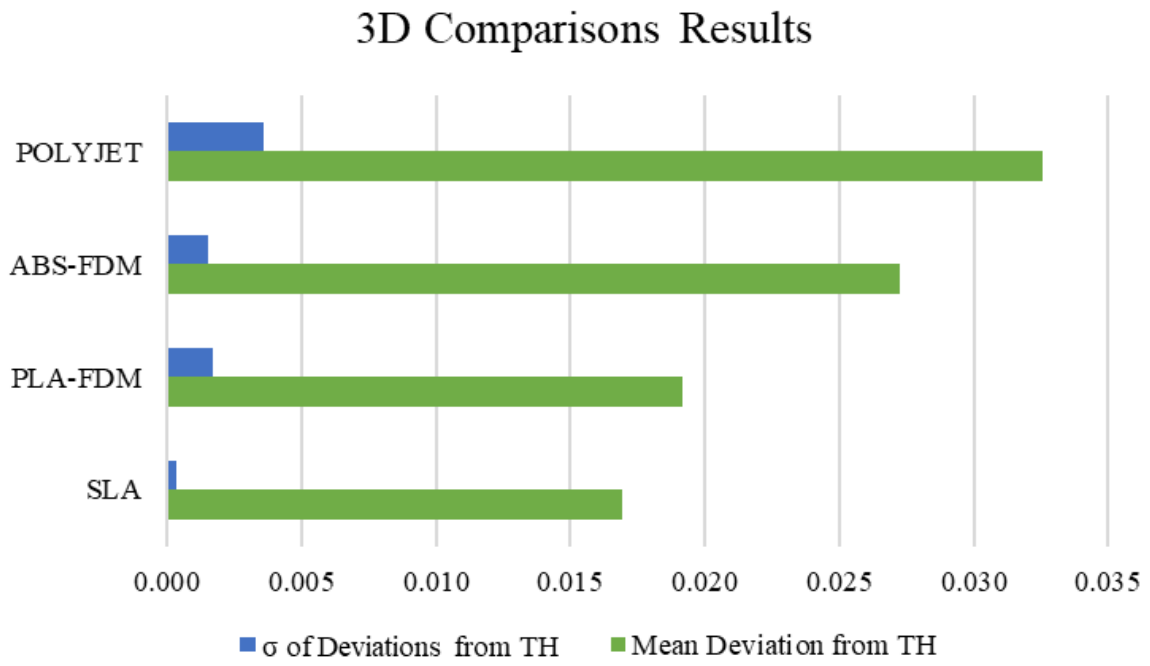

Figure 60 Point Clouds comparisons results using optical profilometer (TH) [100]. *Results are expressed in mm.*

Results obtained from the 3D comparisons between point clouds put in evidence benefits and problems related to exploiting an optical technique like passive photogrammetry, to reconstruct transparent and reflective materials typical of some polymeric 3D printing.
The main advantage of a photogrammetric scanning system, which can be exploited for these kinds of measuring tasks, is its capability to reconstruct the whole model of the object, including the vertical sides, which represent a critical issue for most consolidated optical techniques.
Moreover, the texture-less surfaces and the criticalities due to the reflection effect can be reduced by properly setting the lighting conditions in a way that allows the recognition of common points on subsequent images. *Figure 61* reports the distribution of the deviation between homologous points on photogrammetric models and the one obtained with the TH profilometer. These graphs show that the 95% of PH points was characterized by an absolute distance from the homologous TH points lower than 0,040 mm for SLA and PLA-FDM, 0,080 mm for ABS FDM, and 0,1 mm for the device realized with Polyjet.
3D models for the micro-mixer realized through SLA and the other realized with FDM with grey PLA presented the minimum absolute distances (0,015 and 0,020 mm, respectively) when

compared to the reference model with more than 50% of points within the range from 0 to 10 µm.
The Polyjet micro device was characterized by the maximum values of absolute distance evaluated respect to the reference model (up to 0,1 mm) in correspondence with the micro-channels depths. Moreover, the comparison was complicated due to the low number of points measured with the optical profilometer, which makes it difficult to evaluate channels depths in a reliable way.

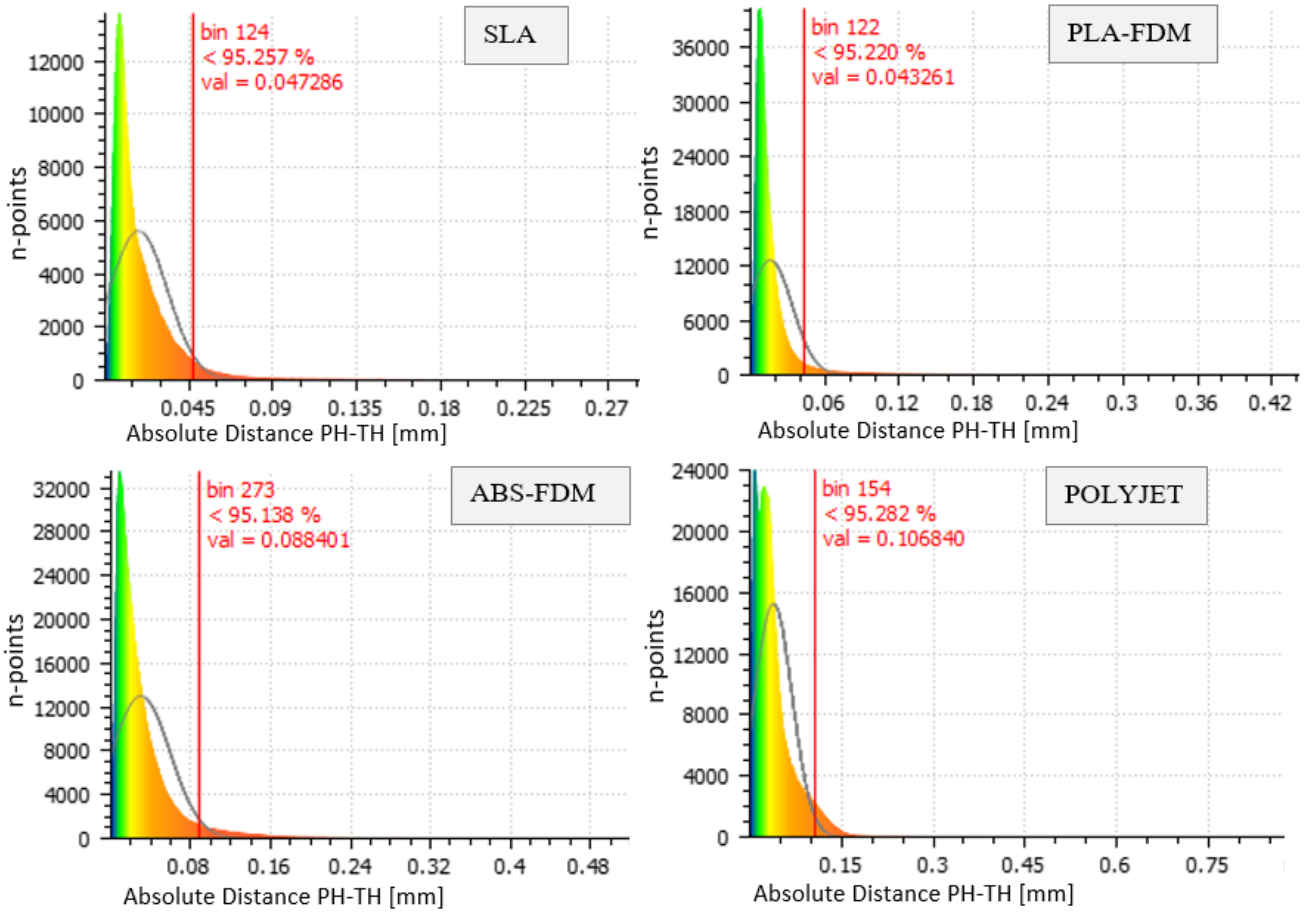

Figure 61 Histograms showing the points distributions respect to the absolute distance between the homologous points on the photogrammetric model and on the reference one [100].

8.2.2 2D analysis results

Subsequently a more detailed 2D analysis was conducted to provide the measure of depth for each of the18 channels. A profile series (100 profiles) was extracted for each model considered and the medium profile analysed with TalyMap software to obtain the channels depth values. Figures from 62 to 65 show the results of measures carried out using photogrammetry (PH) and the optical profilometer (TH), which is considered the reference instrument, with 1 µm of optical resolution. On the *x* axis, the 18 channels of each device are identified with a progressive number. Results showed differences in the order of 0,05 mm for the SLA and slightly higher for the FDM-PLA grey. While the ABS-FDM and the Polyjet overcame the 0,050 mm. Furthermore, all the PH measures were smaller than the TH ones. This behaviour can be explained as a possible scale error related to user-dependency for the scaling method adopted and the difficulty of focusing

on objects due to their smoother and uniform textures. Another consideration should be done regarding the object dimensions and the magnification level chosen. The results showed a data trend leading to lower differences between the photogrammetric model and the reference model in correspondence to the channels located in the object centre. This area represented the most focused part of the object. Indeed, the overall dimensions of the devices (about 33 x 28 x 3 mm^3) are about 50 times the channel depths values (0,6 mm), which means that the micro channels require a magnification level higher than the one used for the entire object. Moreover, the samples were not scanned in a thermally-controlled environment. Temperature variations are directly linked to the systematic deviations that affect the measures. Polymeric materials have thermal expansion coefficients higher than metals (in the order of 70-150 $*10^{-6}$ $K^{-1}$for ABS, 85-100 $*10^{-6}$ $K^{-1}$for PLA).

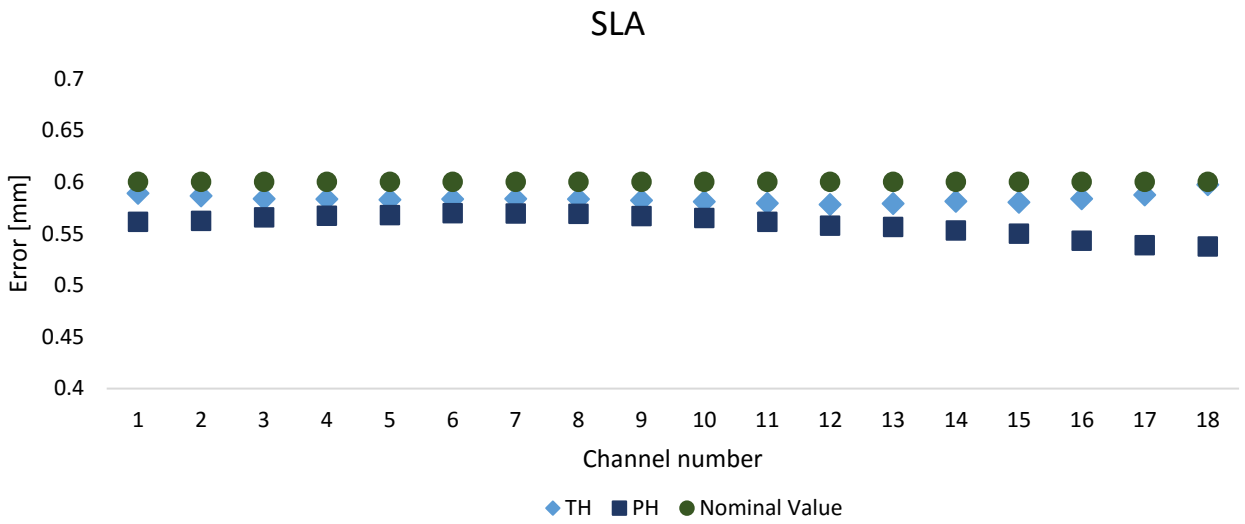

Figure 62 3D model measured depth values of SLA device evaluated with Photogrammetry (PH) and optical profilometer (TH) [100].

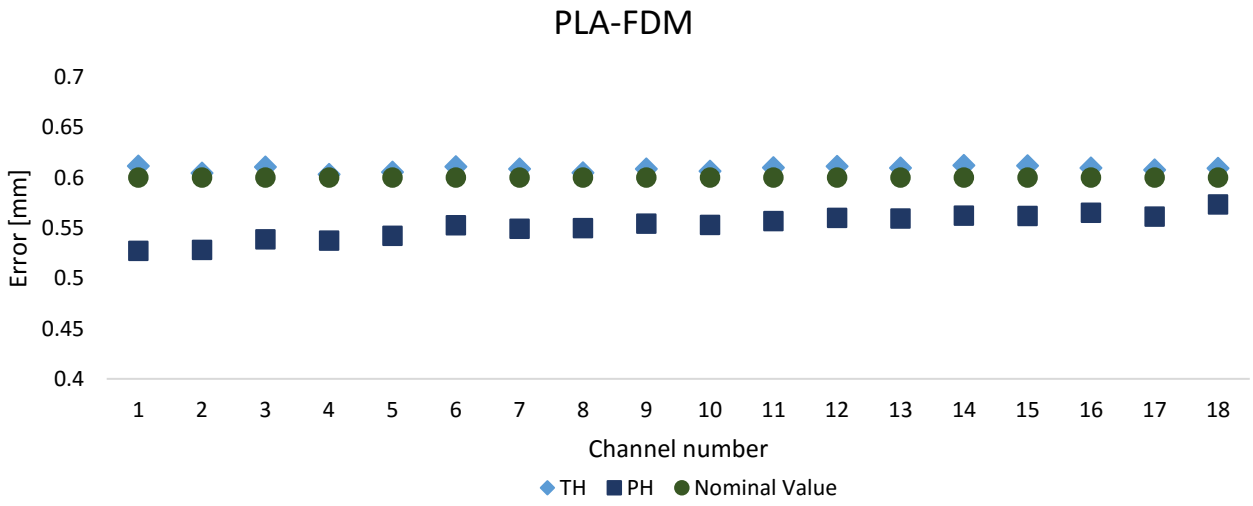

Figure 63 3D model measured depth values of PLA-FDM device evaluated with Photogrammetry (PH) and optical profilometer (TH)[100].

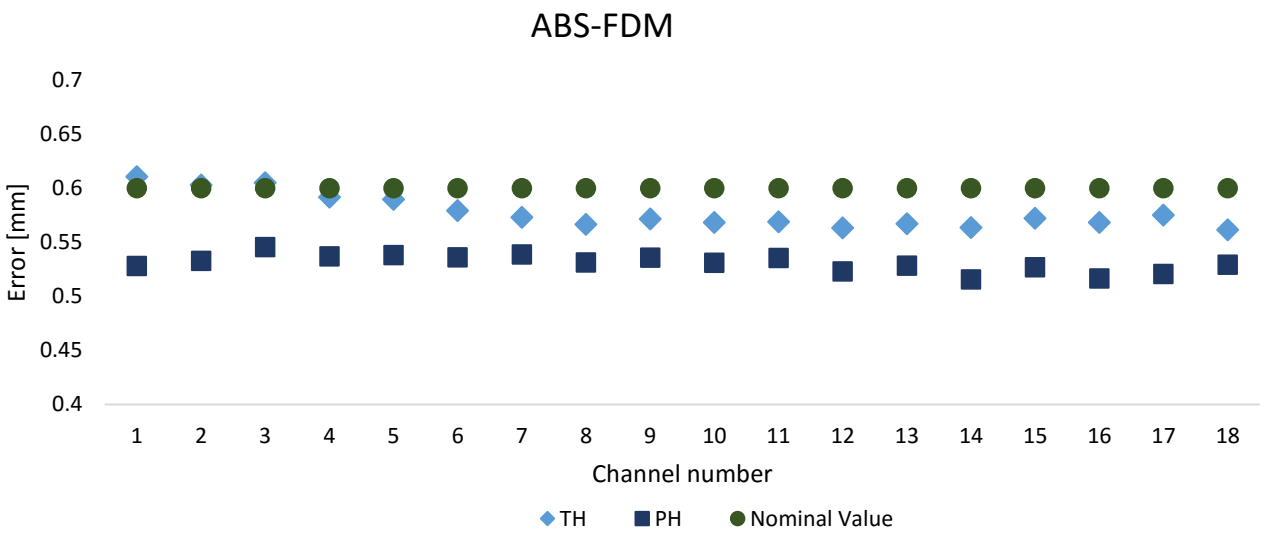

Figure 64 3D model measured depth values of ABS-FDM device evaluated with Photogrammetry (PH) and optical profilometer (TH) [100].

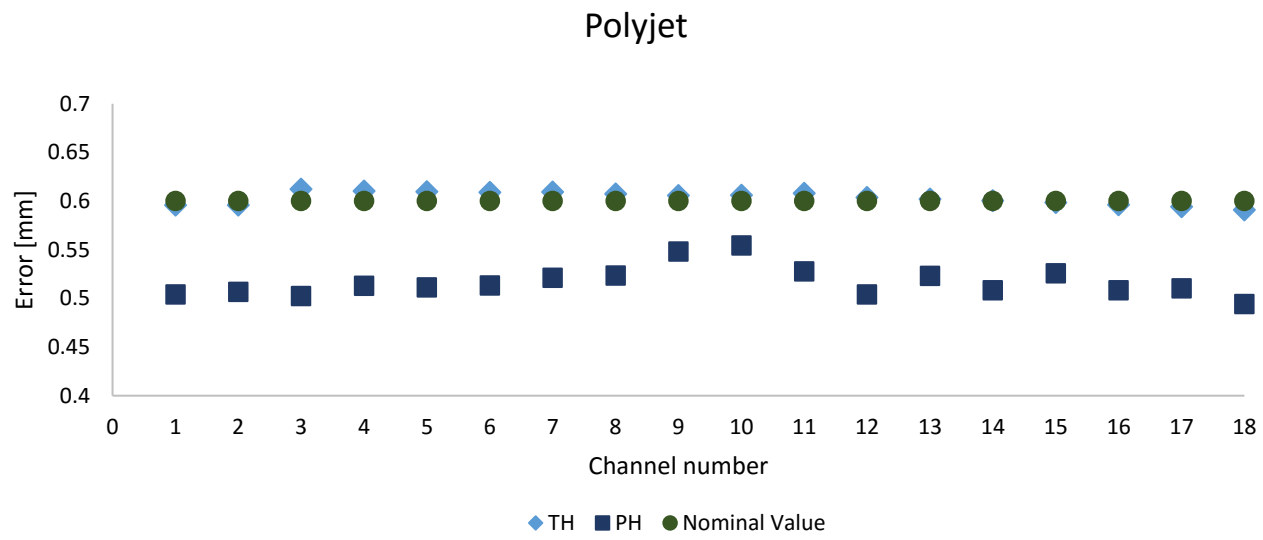

Figure 65 3D model measured depth values of Polyjet device evaluated with Photogrammetry (PH) and optical profilometer (TH) [100].

For each depth measure, the uncertainty component due to the measuring procedure was computed starting from the standard deviation obtained from the three scans repetitions.

$$u_p = \frac{S_x}{\sqrt{n}} \qquad (8.6)$$

Where:
S_x is the experimental standard deviation calculated as the square root of the variance;
n is the number of observations.

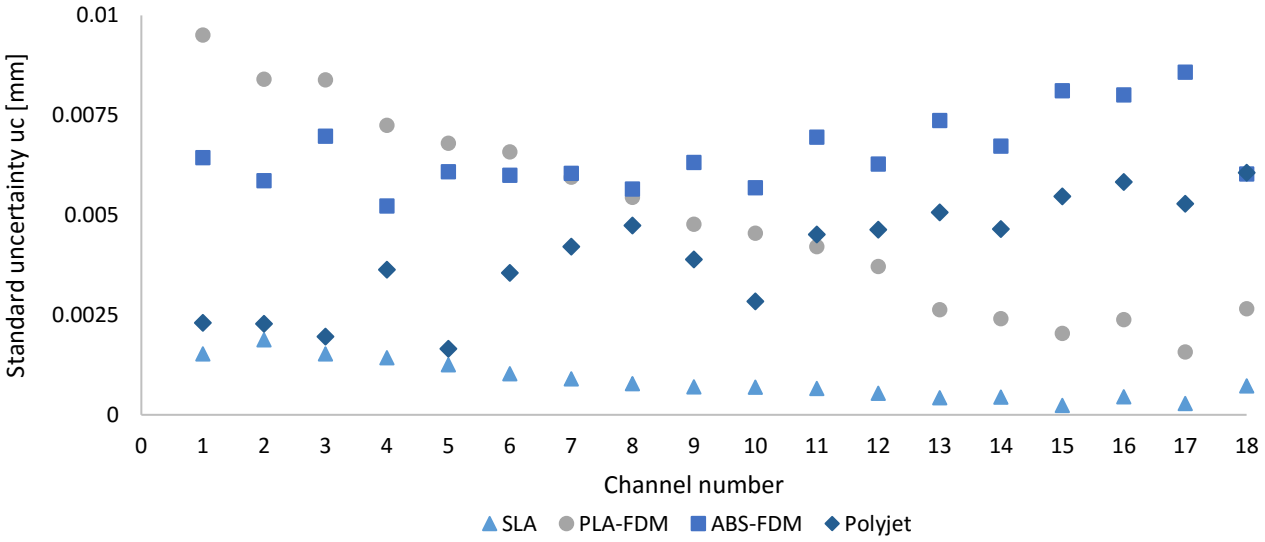

Figure 66 Uncertainty component due to the measurement procedure [100].

Figure 66 shows that the standard uncertainty, considering all the 18 channels, was below 2 μm for the SLA and below 10 μm for all the devices, when measuring channel sections equal to 0,6x0,6 mm^2. The reason of different uncertainty value on different channels could be partially attributable to the variation of lighting conditions between subsequent sets of photographic images as well as the low number of points reconstructed after the alignment phase, which increases the uncertainty component due to the repeatability of the software.

8.3 Conclusion

Despite the unfavourable conditions due to reflectance and transparency of the devices, photogrammetry provided promising results. In particular, the device realized with SLA, registered the minimum deviations in the order of 0,01 mm with a standard uncertainty of 0,001 mm. Results seemed to be mostly affected by material reflectance (ABS-FDM and Polyjet), rather than material transparency (SLA). This makes this technique particularly suitable for dimensional verification of samples made via SLA; the grey PLA led to promising results too. In addition, the location of the channels respect to the object centre, which is the most focused area, seemed to affect the amount of the deviation registered in respect to the TH models.

Chapter 9 - Performance verification through a miniature step gauge and comparison with other measuring techniques

In this chapter, the implementation of a miniature step gauge made of black Polyphenylene sulfide (PPS), as reference object, is reported. The step gauge was reconstructed by non-contact scanning systems, optical and x-ray-based scanners. A comparison was then carried out respect to measures of the reference step gauge already calibrated with a CMM. The geometrical characteristics of the sample are suitable for investigating different aspects of non-contact measuring instruments.

9.1 Materials and Methods

With the purpose, four technologies were involved and they are respectively, the photogrammetry-based system, PSSRT, a laser scanner, structured light scanner and a CT scanner.

9.1.1 Step gauge artefact

Step gauges are typically obtained by assembling typical gauge blocks made of steel or ceramic. Although, these kinds of materials are very difficult to acquire with an optical-based system due to the reflectivity, or, as well, with a CT scanner due to the high density. Polymers represent a good alternative even if they present well known drawbacks, in terms of stability over time and machinability with sufficient accuracy and surface quality[40]. Step gauge artefacts were originally designed in [102] and subsequently adopted to characterize and correct systematic errors in a CT scanning system[41,44,45]. They feature both unidirectional and bidirectional lengths allowing the investigation of problems related to the scale factor, other errors and depth of field limitation. Regarding the latter, characteristic of some optical-based scanners such as photogrammetry-based and structured light scanners, the smaller the field of view, the better the resolution, but lower the depth of field. Thus, along the overall working volume, there is a

more focused area and a less focused area. The step gauge geometry, structured in several and equal steps, allows to observe this effect.
Studies about material were carried out taking into account material density, thermal stability and form errors. From these studies, PPS material with 40% of glass resulted to be a good compromise between form errors similar to the ones of aluminium and steel, a good thermal stability, and a lower density, ensuring a better X-ray penetration.
The overall dimensions of the step gauge, see *Figure 67*, are 58x8x7 mm^3 and it is structured with 11 grooves with 2 mm of depth and width.

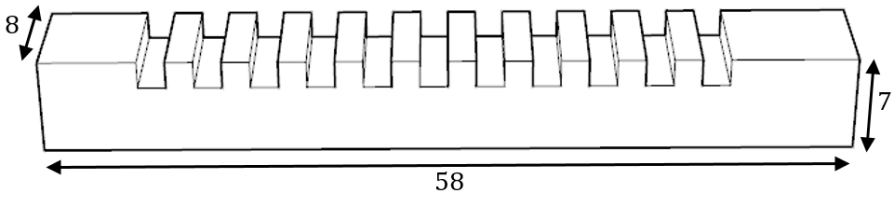

Material	PPS
Grade	PPS GF 40
Thermal Expansion *Coefficient*	30 [10-6 * K-1]

Figure 67 Step gauge: overall dimensions and material properties, dimensions are expressed in mm.

The measuring protocol involved several steps with the aim to obtain both unidirectional and bidirectional lengths, see *Figure 68*.

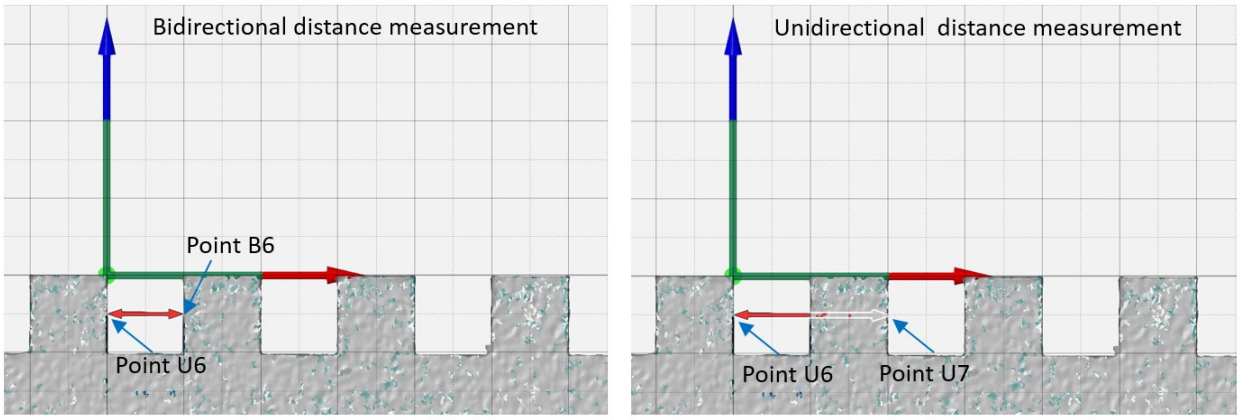

Figure 68 Unidirectional and bidirectional lengths definition.

The lengths are measured starting from the sides located in the centre of the step gauges up to cover the entire length of the step gauge, which is, nominally 42 mm, for a total of five unidirectional lengths and six bidirectional lengths, see *Figure 69*.

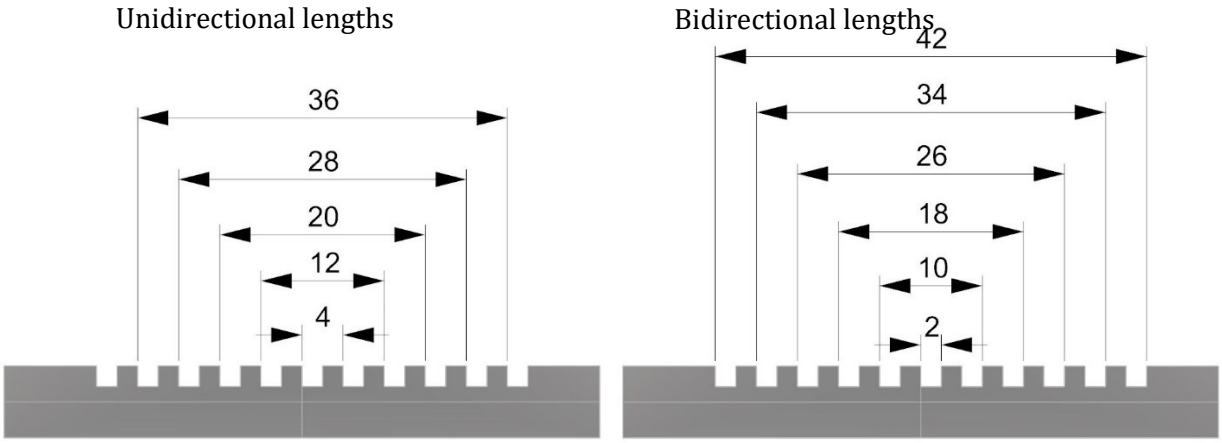

Figure 69 Unidirectional and bidirectional lengths selected for the evaluation. Values are expressed in mm.

Following this procedure, a plane is fitted for each groove side, both left and right sides.
Each plane of the step gauge was computed in the CMM software Calypso from eight points probed, *Figure 70*-A, while the least square fitted method with 3-sigma number of points was adopted in the plane computation for all non-contact scanning instruments, as reported in *Figure 70*-B.

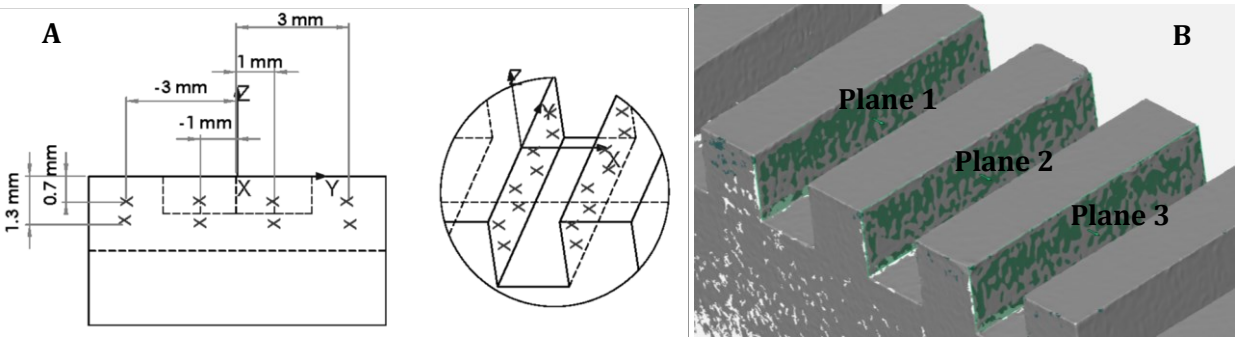

Figure 70 CMM probing strategy (A), least square fitting procedure on acquired data with non-contact instruments (B).

With the aim to compute distances, the intersection points between fitted planes and a central line, were considered.
The step gauge was measured with a CMM Zeiss OMC 850, with a maximum permissible error of 2,5+L/300 µm, equipped with a probe with 0,8 mm of diameter. Measures are reported in *Table 15* with the associate expanded uncertainty, computed according to the PUMA method and the Eq. (9.1).

Table 15 Step gauge calibrated lengths.

	Bidirectional Lengths			**Unidirectional Lengths**	
	Length [mm]	U [mm]		Length [mm]	U [mm]
B1	1,997	0,0008	**U1**	3,999	0,0020
B2	9,999	0,0008	**U2**	11,997	0,0011
B3	17,999	0,0012	**U3**	19,995	0,0013
B4	25,996	0,0019	**U4**	27,994	0,0019
B5	33,996	0,0022	**U5**	35,994	0,0022
B6	41,998	0,0026			

9.1.2 Scanning parameters

Scanning parameters and strategies were defined for each instrument involved.

9.1.2.1 Structured light scanner

The structured light scanner is an ATOS III scan, see *Figure 71*, a blue light structured scanner with two cameras and a projector, equipped with 90 mm lenses, which allows to measure a working volume of 60x45x30 mm^3 with a structural resolution of 0,017 mm. The scanning strategy adopted is the following. With the aim to acquire the reference object entirely, the latter was positioned at the centre of rotary table and a series of scans have been carried out every 22,5°, for a total number of 16 scans, while the sensor was tilted of 45° respect to the rotary table (xy plane). The structured light scanner will be renamed as SLS in the section dedicated to the results.

Figure 71 ATOS III scan used for the reconstruction.

9.1.2.2 Laser based scanner

The laser scanner used was a 3SHAPE D800, see *Figure 72*, a line laser with a tilting and rotating table and resolution of 0,02 mm. The scanning strategy adopted was a result from an optimization problem between quality of results (minimum error respect to the CMM values and minimum scanning time). The configuration was then, a tilt angle of 45° and a rotary stage of 36°, which means 10 projections. The structured light scanner will be renamed as LLS in the section dedicated to the results.

Figure 72 Laser scanner 3SHAPE D800, used for the reconstruction.

9.1.2.3 Photogrammetry based scanner

The PSSRT, see *Figure 73*, was equipped a Canon Eos 760D with a Canon EF 50 mm 1:1:8 II objective lens equipped with an extension tube of 20 mm, with a consequent ground resolution of 0,012 mm/pixel. The sensor was tilted of 45° and 72 pictures were taken rotating the object with a step of 5°.

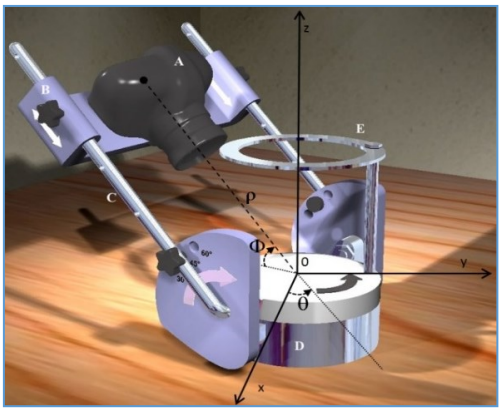

Figure 73 The PSSRT used for the photogrammetric reconstruction.

9.1.2.4 CT scanner

The CT scanning system was a Nikon Metrology NCT 225 scanner, see *Figure 74*, and the scanning parameters are reported in *Table 16*.

Figure 74 CT scanner used for the reconstruction.

Table 16 CT scanning parameters.

Voltage [KV]	Power [W]	Current Intensity [μA]	Magnification level m	Voxel size s [mm]	Exposure time [sec]	N projections	N frames/ projection
60	14,2	236	6	0,033	1,4	1500	8

Before reporting the results obtained with the three instruments involved, it is important to underline the necessity for the CT results to be corrected for systematic errors. Firstly, a temperature compensation is needed. Once this was done, results were still affected by a systematic effect, which is proportional to the length and it is due to a scale error. The data trend was then described by a linear function, *Figure 75*, for both unidirectional and bidirectional lengths. The correction of the scale error is usually done through the unidirectional lengths. The

step gauge is very suitable for this task and allows the analysis of both, threshold dependent and threshold independent errors.

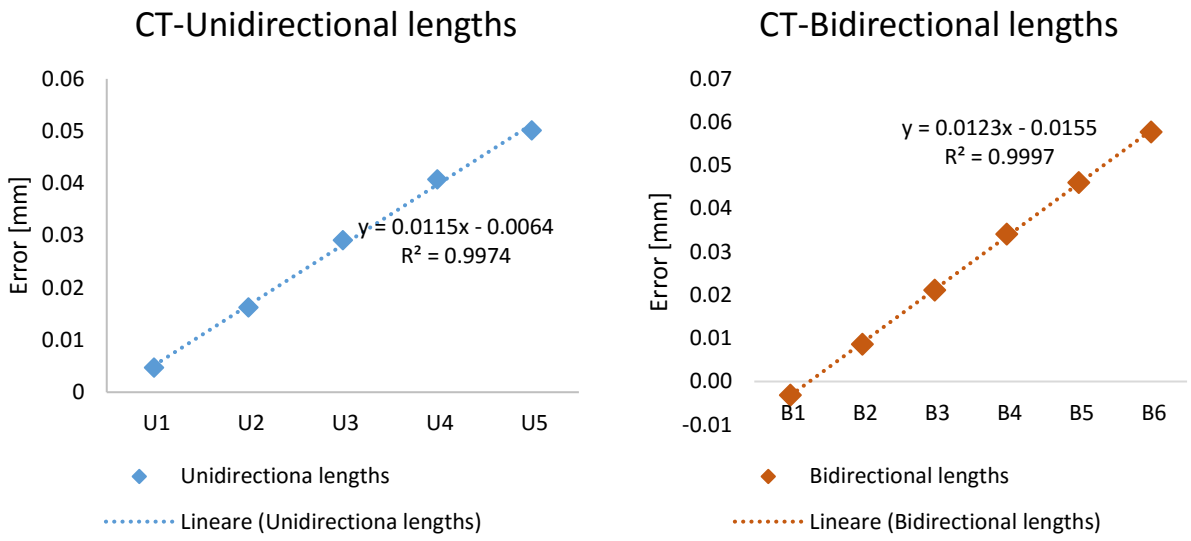

Figure 75 CT Results: Unidirectional and Bidirectional lengths - without correction of the scale error

Results obtained after the correction of the systematic effect due to the scale error are shown in *Figure 76*. Errors on bidirectional lengths and then, threshold dependent errors are still high and they could be approximately estimated as the difference between the intercepts of the linear trends reported in *Figure 75*. Indeed, the slopes of the linear functions were very similar, but the line interceptions were different of about 9 micrometres.

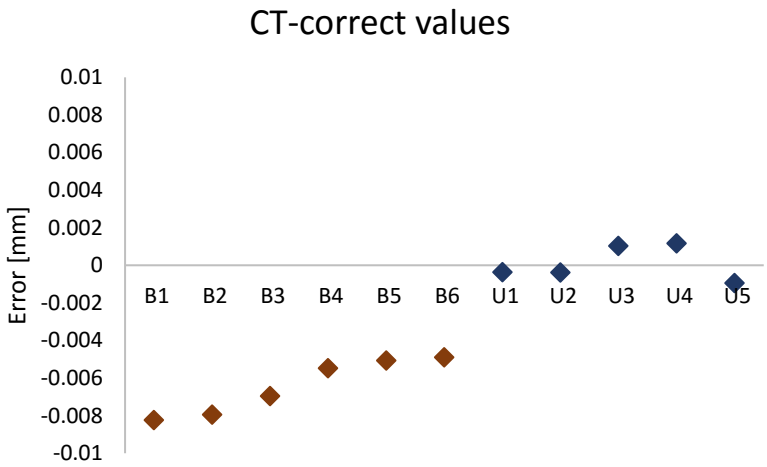

Figure 76 CT Results: unidirectional and bidirectional lengths after scale correction.

9.1.3 Uncertainty assessment

The uncertainty evaluation was conducted according to the PUMA method (ISO 14253-2). The confidence level is set to 95% to which a coverage factor equal to 2 corresponds.
The general equation is reported below, Eq. (9.1) and the uncertainty components are reported in

Table 17.

$$U = \sqrt{u_r^2 + u_m^2 + u_e^2 + u_w^2 + u_p^2} \quad (9.1)$$

Table 17 Uncertainty assessment.

Uncertainty component	Symbol	Type	Estimation	SLS	LLS	PPSRT	CT
Reference	u_r	-	Step gauge is itself a reference object	-	-	-	-
Instrument	u_m	-		-	-	-	-
Workpiece	u_w	A	Form error	ΔFlatness	ΔFlatness	ΔFlatness	ΔFlatness
Temperature	u_e	B	Temperature variation	±1° C	±1.5° C	±2° C	±3° C
Procedure	u_p	A	Repeated measurements	σ_y	σ_y	σ_y	σ_y

9.2 Results

Results obtained with SLS showed a kind of trend for both unidirectional and bidirectional lengths, *Figure 77*. The error registered respect to the CMM value is increasing from the U1 to the U5, and from B1 to B6.
The reason could be due to the depth of field limitation of this instrument. Distances are structured as reported in *Figure 69* and so distances involving more central sides are characterized by lower errors than distances involving sides farther from the focusing point.

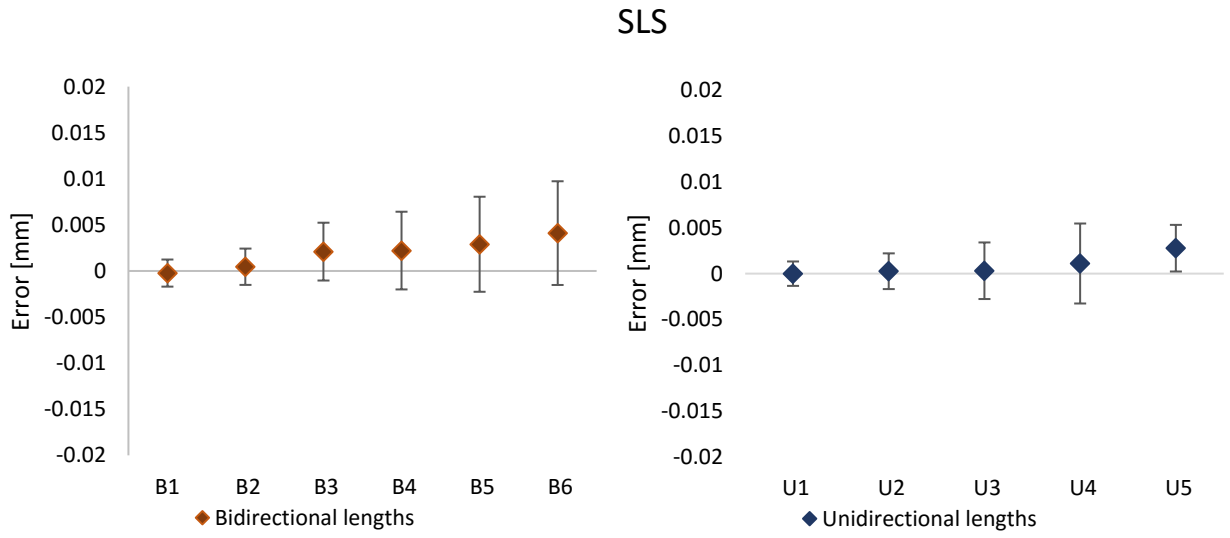

Figure 77 Results obtained with SLS on Unidirectional and Bidirectional lengths.

The laser line scanner did not show any detectable trends or systematic effect on unidirectional lengths, with errors less than 0,005 mm for all the measurands. Bidirectional lengths present higher errors, up to 0,010 mm, *Figure 78*.

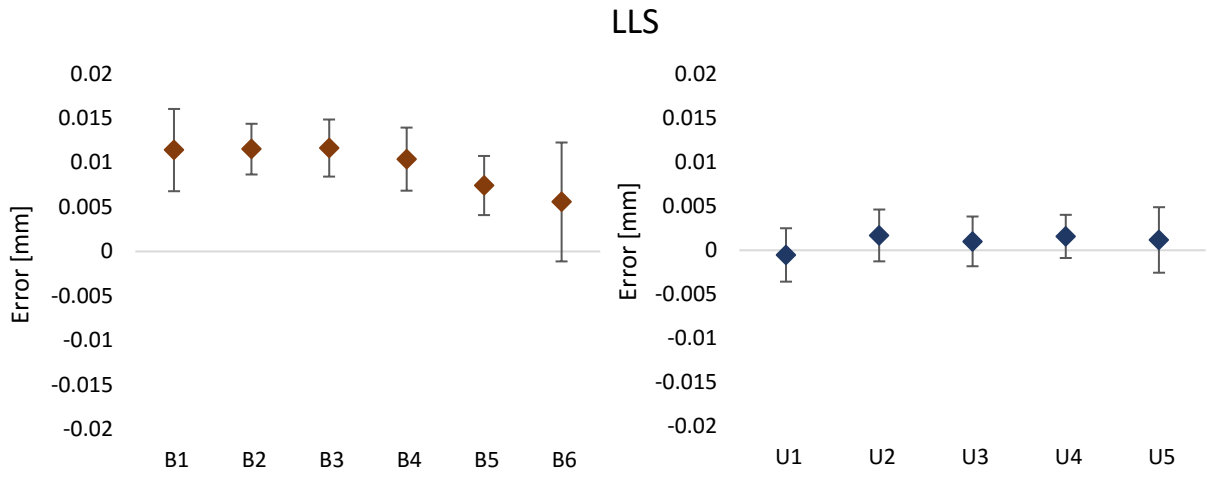

Figure 78 Results obtained with LLS on Unidirectional and Bidirectional lengths.

The PSSRT after the scale error correction by means of unidirectional lengths, showed errors on unidirectional length up to 0,0025 mm and errors on bidirectional lengths up to 0,009 mm, see *Figure 79*.

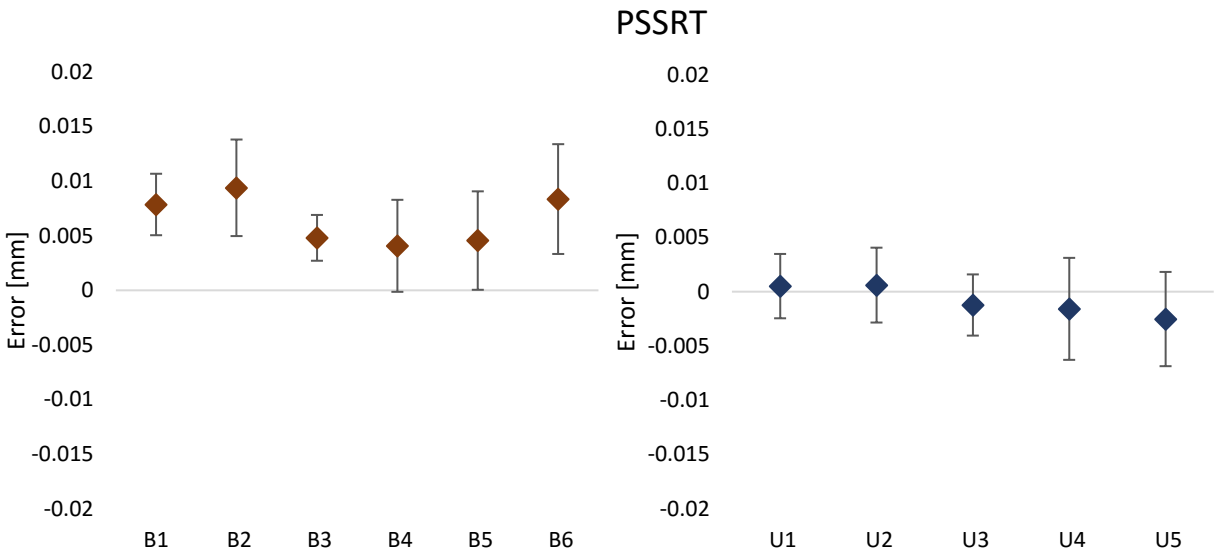

Figure 79 Results obtained with PSSRT on Unidirectional and Bidirectional lengths.

Results obtained with the CT scanner after the scale error correction were in the same order of the other instruments, with unidirectional lengths characterized by errors less than 0,005 mm and bidirectional lengths characterized by errors up to 0,009 mm, see *Figure 80*.

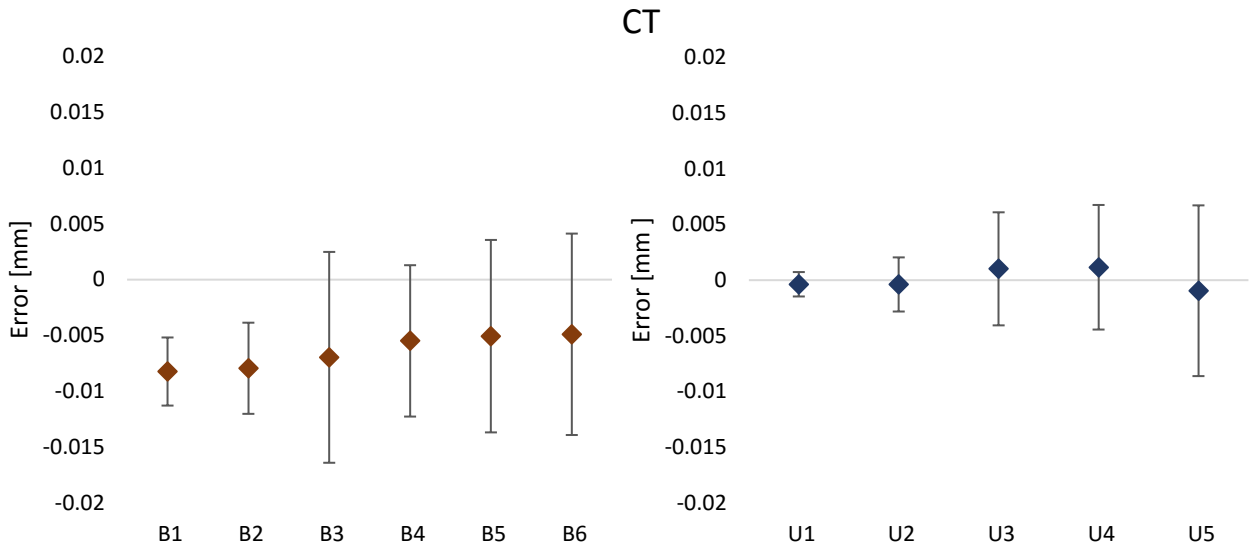

Figure 80 Results obtained (after correction) with CT on Unidirectional and Bidirectional lengths.

Uncertainties computed with the proposed method, resulted to be higher for the non-contact measuring instruments, respect to the CMM and the most affecting components are related to the form error influence and the procedure. An overview of the results obtained for each instruments is reported in *Figure 81*. From errors registered on bidirectional lengths it is possible to observe two trends, SLS and CT, with the same slope and different intercepts.

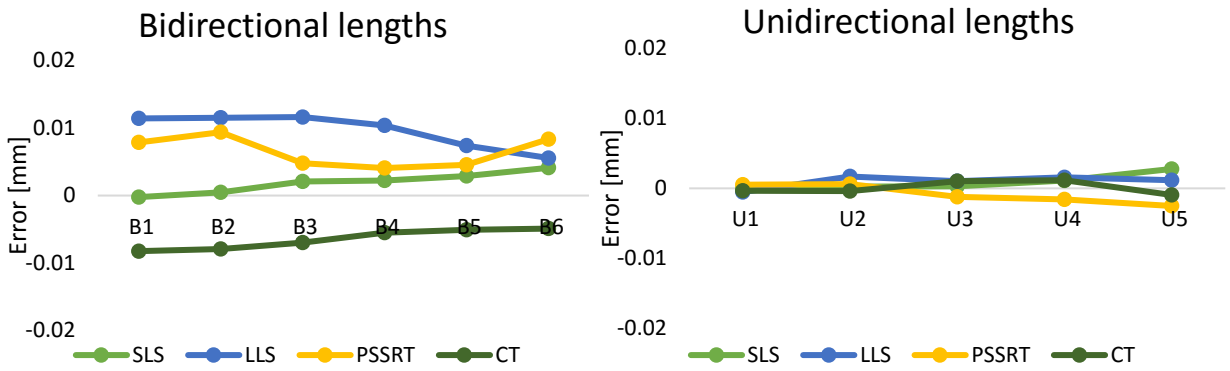

Figure 81 Errors estimated on bidirectional and unidirectional lengths.

9.2.1 Form error effect on total uncertainty

Form error is considered as a source of uncertainty coming from the workpiece, in terms of errors due to the machining process or the machinability of the material used. In this case, distances between planes were considered as measurands and the form error should be considered on planes computed for each acquisition system. Typical form errors involved in the computation of distances between planes are flatness, angularity, parallelism, etc…. In this case, distances between planes are computed as distances between points, and only flatness was considered in the uncertainty budget. Flatness is strictly related to the surface texture, since it should contain the entire surface and, then, the maximum peak and the minimum valley. Thus, primary profiles were collected using a stylus profilometer Taylor-Hobson RTH Talysurf 5-120

with Z resolution of 0.001 µm. Measurements were carried out on the left side of groove 1 and 6, and on the right side of groove 6 and 11, *Table 18*.

Table 18 Flatness and Primary profile parameters.

	Processing software	**Groove 1 (L)**	**Groove 6 (L)**	**Groove 1 (R)**	**Groove 11 (R)**
Pz [µm]	Sursam	7,243	9,137	11,318	10,773
Pa [µm]	-	1,746	1,400	2,431	2,599
Flatness[µm] CMM	Calypso	1,839	1,393	1,236	3,9133
Flatness [µm] SLS	GOM Inspect	23,530	18,392	34,568	39,276
Flatness [µm] LLS	Convince	59,928	49,938	44,762	58,062
Flatness [µm] PSSRT	GOM Inspect	58,240	35,341	51,442	46,336
Flatness [µm] CT	GOM Inspect	16,420	22,712	18,989	26,328

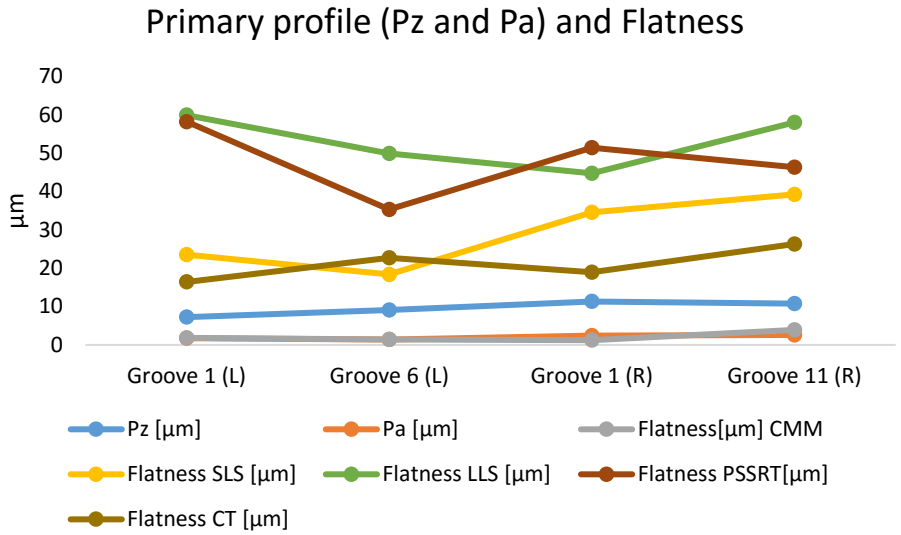

Figure 82 Flatness evaluated with every instrument involved in the comparison compared with Pz value evaluated on Groove 1(L,R), 6 (L) and 11(R).

It is possible to observe from the graph, *Figure 82*, an underestimation of flatness measured with the CMM and, on the other hand, an overestimation for all the non-contact instruments. Surface quality (Pz) affects the form error (flatness) in a way strictly dependent on the "sensitivity" of the instrument. It is well known that a CMM contact probe acts like a mechanical filter (a low-pass filter) on surfaces and it is more sensitive to the peaks of the profile rather than valleys. The "filter" resulted depends on the probe diameter, higher the diameter higher the filter applied, *Figure 83*. Optical instruments and CT-scanners are more sensitive to surface texture, because generally the resolution of those instruments is far better than a probe diameter. A first consequence is that the form error evaluated with a CMM is less than the form error evaluated with an optical, or generally, with a non-contact instrument.

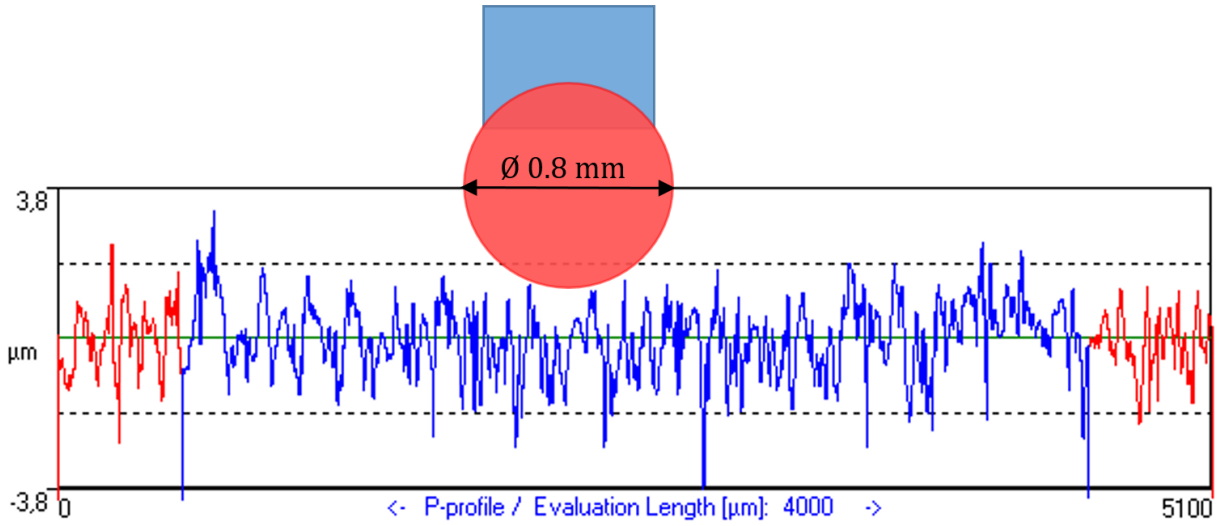

Figure 83 Primary profile groove 1L.

A way to evaluate the effect of the surface texture on the measurements obtained could be to consider the variability of the flatness evaluated over the repetitions. Looking at those data will allow to detect, firstly, if there are any systematic errors (e.g. due to the probing force for the CMM), while the random part will be the effect due to the surface profile on the uncertainty of the results. This is a way to comprise the form error in the uncertainty budget without the usual overestimation of the effect of the form error, but at the same time, this method considers not just the form error quantified through the reference instrument (CMM in this case) but it is function of the different sensitivity of the instruments.
There are in fact two effect of surface texture (tactile texture). First of all, greater the Pz, the maximum distance between peaks and valleys evaluated on the primary profile, greater the interval in which a point can be. If the resolution of the instrument is numerically higher than the spacing between two adjacent peaks and valleys, Psm, there is a bias due to the shifting of the probed point towards the peaks of the surface.
The other effect is to increase the uncertainty of the measurements due to a randomic effect. Thus, in a CMM, the primary profile has a little effect as uncertainty component, but it should be considered as bias. Regarding optical and, generally, non-contact instruments, they could be affected by a bias and uncertainty, but generally, being the resolution of the optical instruments numerically lower than probe diameters and Psm value, the bias effect will be minimum, but the prevalent effect will be on the uncertainty of the results.
From data reported in *Table 18*, it is possible to observe that the CMM estimation of the flatness is comparable with the Pa parameter, while all the other instruments present a very high overestimation of that form error. One reason is attributable to the mesh approximation. The minimum edge of the polygonal meshes varies from 0,01 mm for the SLS to 0,1 mm for the LLS. This means that, even if the resolution of the system is better than the Psm value (it would be expected a flatness value very close to the Pz), there is a contaminant effect due to the meshing approximation, which increases the uncertainty of the optical measures.
In this case, the meshing process was carried out with different softwares. For the LLS, the mesh reconstruction (through the software Convince) is part of the reconstruction routine and there is no way to change setting parameters, while outputs from SLS and CT were managed with GOM Inspect software and, finally, for the CMM, Calypso was used. This aspect has a great importance

since the meshing process, even if very accurate, is still an approximation of the real surface acquired.
Including the variability of the form error in the uncertainty budget, allows to consider contemporary the effect due to the different sensitivity of the instruments and the uncertainty coming from the meshing process, which can vary according to different software and processing parameters.

9.2.2 Depth of field limitation

Another effect, already observed on bidirectional and unidirectional lengths errors, is related to the depth of field limitation. Starting from the assumption that the focusing point is located in correspondence of the groove 6, it is predictable that the reconstruction of the groove sides is better near the focusing point and worse as long as the distances involve groove sides far from that point.
It is pretty clear the difference between a depth of field limited instrument (SLS) and a CMM, *Figure 84*.

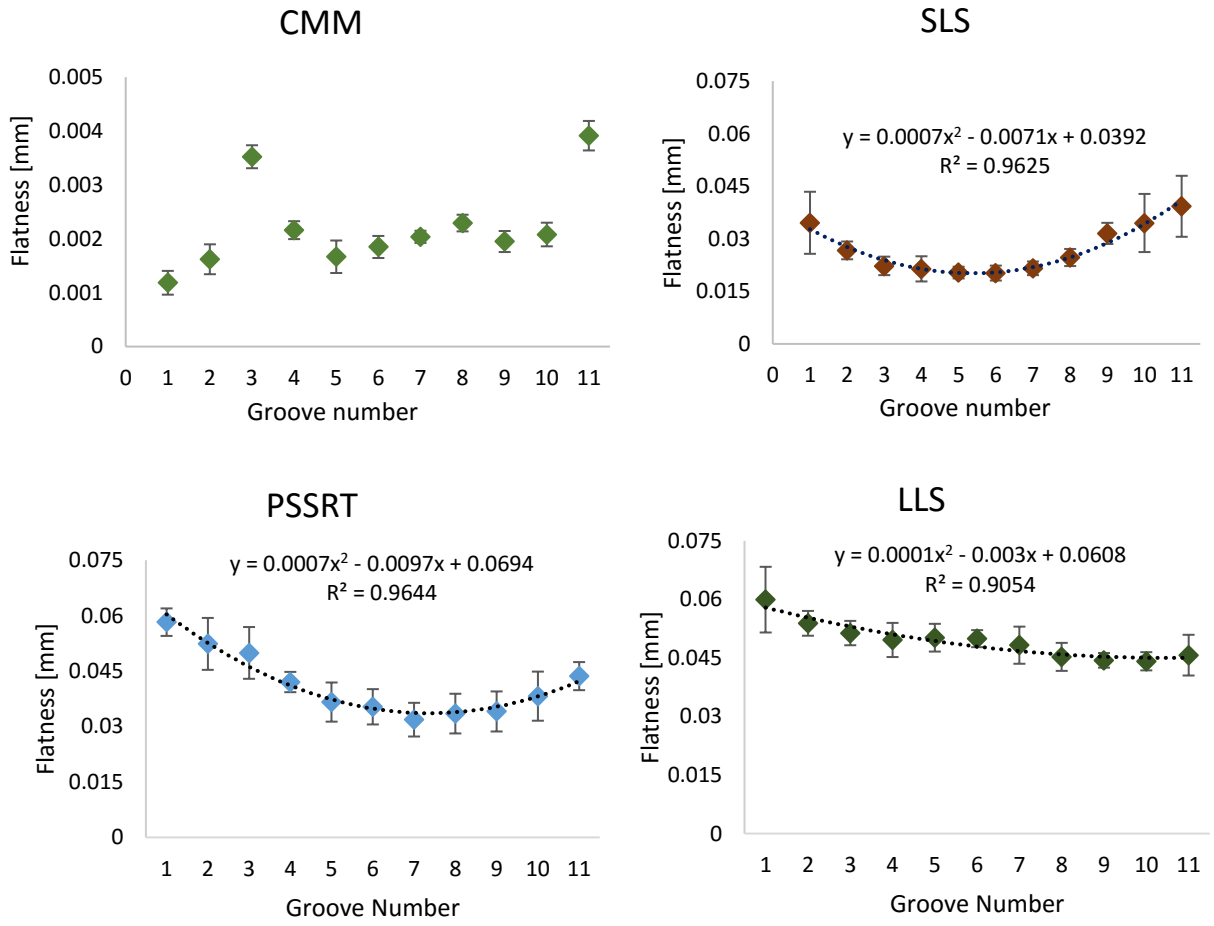

Figure 84 Flatness evaluated on CMM results and on SLS, LLS and PSSRT results.

As it is possible to observe on the graph, flatness values and their relative standard deviations are randomly distributed for a CMM, while an optical instrument is clearly affected by the position of the measurand in the sample. Analysing results obtained with SLS and PSSRT it is

possible to observe a kind of tendency, with the minimum value of flatness in correspondence of the grooves 5, 6 and 7, approximately the location of the focusing point and increased values at the extremes.
A structured light scanner has a specific working volume, but within the working volume the number of points acquired, and the quality of these points can differ depending on how far the measured point is from the focusing point (which corresponds to the centre of the working volume).
It is possible to detect the same tendency for the PSSRT system: increasing the magnification level means decreasing the depth of field value. The parabolas are not perfectly symmetric respect to the symmetry axis and it is probably due to problems in the centring of the sample on the rotary table.
LLS system seemed to be not affected by the same trend, with an R value of approximately 0,9, instead of 0,96 for the other two instruments.
The step gauge resulted to be very suitable for detecting and quantifying this effect due to the step structure and further works will be conducted to evaluate the depth of field limitation affecting most of optical instruments.

9.3 Conclusion

In this chapter, the miniature step gauge reference object was introduced for the performance verification of optical instruments, in the small range. In particular, the PSSRT was compared with other two optical measuring instruments, a structured light scanner (SLS) and a laser line scanner (LLS), and an x-ray based instrument (CT). Unidirectional and bidirectional lengths were retrieved up to a maximum of 42 mm and CMM measurements of the step gauge were used as reference.
Results showed errors less than 0,003 mm for unidirectional lengths, with uncertainties of ±3,5 μm for SLS and LLS, while uncertainty for PSSRT and CT were higher, up to 0,012 mm. Bidirectional lengths were instead still low for the SLS (up to 4 μm) with uncertainties up to10 μm, but higher for LLS (up to 12 μm with uncertainties up to 15 μm), for PSSRT (8 μm with uncertainties up to 15 μm) and for CT (up to 9 μm with uncertainties up to 20μm). The LLS, PSSRT ad CT resulted to have higher errors on bidirectional lengths, due to the sub-scattering effect or the threshold definition for the CT.
Through the comparison with the CMM, it was also possible to detect some aspects strictly connected to the use of optical instruments and consider them in the uncertainty assessment. In this context, the form error effect was considered not as flatness itself but as variability of flatness in order not to overestimate its effect in the uncertainty budget and it was evaluated for each instrument involved, in order to consider the different sensitivity of the instruments, due to the different resolutions and also the approximation due to the meshing process which increased the total uncertainty especially for LLS, PSSRT and CT. On the other hand, SLS and PSSRT presented another detectable effect due to the depth of field limitation, recognizable from the unidirectional and bidirectional errors trends and from the flatness tendency.

Chapter 10 - Material and colour investigation involving optical based 3D scanners

In this chapter, an investigation on the influence of object material and colours was conducted. For the purpose, five miniature step gauges made of different polymers and different colours were scanned with the PSSRT and two other optical instruments and the effects due to their different optical properties, investigated through the evaluation of the errors respect to the values calibrated with a contact CMM.

10.1 Materials and methods

The optical properties of an object's surface are known to affect 3D optical scanner measurements. Lambertian surfaces are called those surfaces, which diffusely reflect projected light and they are ideal for 3D optical scanner measurements. But reality is full of translucent and reflective surfaces and generally little useful data may be recorded since the laser beam, the projected pattern or, more generally, the light, is reflected away. Surface colour has also been shown to affect the data that a 3D optical scanner is able to record [35].

10.1.1 3D scanners used in this investigation

In this investigation, five step gauges, made of different materials and colours were scanned with different optical instruments, the first two are from the DTU metrology laboratory, while the photogrammetric scanner is placed at Polytechnic of Bari in the mechanical engineering department and used in the previous chapters.

- ATOS III scan Rev. 2, equipped with 90 mm lenses, which allow to measure a working volume of 60x45x30 mm^3 with a resolution of 0,017 mm. The scanning strategy adopted was a polar scan, with the step gauge positioned at the centre of rotary table and 8 acquisitions were carried out every 45°, while the sensor was tilted of 45° respect to the rotary table (xy plane). This scanner is recognized in the chapter as SLS.

- 3SHAPE D800, a laser line scanner with a tilting and rotating table and resolution of 0,02 mm. The scanning strategy adopted was a tilt angle of 45° and a rotary stage of 36°, which means 10 acquisitions. This scanner is recognized in the chapter as LLS.

- PSSRT equipped with a Canon Eos 760D, a Canon EF 50 mm 1:1:8 II objective lens and an extension tube of 20 mm, which determines a consequent ground resolution of 0,012 mm/pixel. The sensor was tilted of 45° and 72 pictures were taken rotating the object with a step of 5°.

10.1.2 Step gauges description

The five step gauges have the same nominal dimensions and are made of different materials and colours. The same step gauges were scanned and analysed in [103] using a structured light scanner developed at the department of Compute at the Denmark Technical University. The aim of this research was to better understand the interactions between a 3D optical scanner and different materials and colours, investigation the so called, sub scattering effect. The same effect is investigating in this chapter, using three different 3D optical scanners, exploiting three different measuring principles.

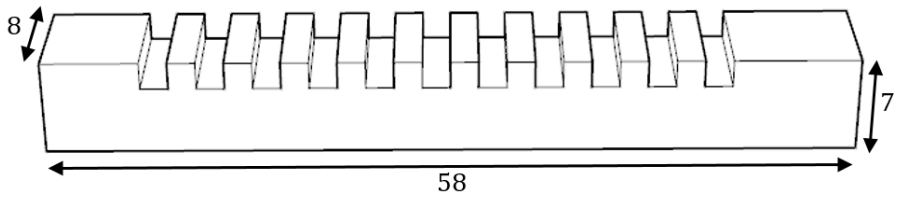

Figure 85 Step gauge main dimensions [mm].

The materials are polymers and more detailed information are reported in *Table 19*.

Table 19 Step gauges used for the investigation.

	Step gauge	Material	Colour	Coefficient of Thermal Expansion (CTE) [10^{-6}*K^{-1}]
	POM-C#1	POM	Colourless	120
	ABS-G#1	ABS	Grey	90
	PPS-N#7	PPS	Black	30
	POM-B#1	POM	Blue	90

	PK-B#1	PEEK	Beige	50

The step gauge geometry features unidirectional and bidirectional lengths. The former are suitable to detect scale errors, while the latter allow to detect the errors due to the sub-scattering effect etc… .
Materials and colours effects on the acquired surfaces are determined through the bidirectional lengths measurements, see *Figure 86* .

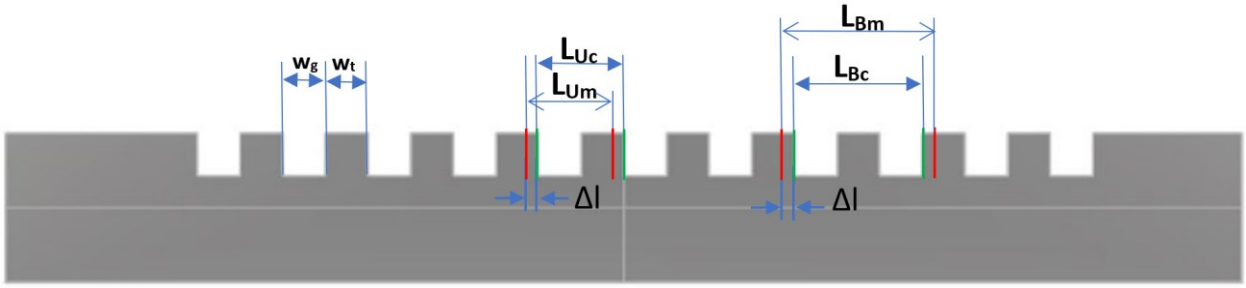

Figure 86 Step gauge, unidirectional and bidirectional lengths definitions.

$$L_{Um} = w_g + w_t - \Delta l + \Delta l \quad (10.1)$$

$$L_{Bm} = w_g + w_t + w_g + \Delta l + \Delta l \quad (10.2)$$

Where,

L_{Bm} is the measured bidirectional length;

L_{Bc} is the calibrated bidirectional length with a contact probe;

L_{Um} is the measured unidirectional length;

L_{Uc} is the calibrated unidirectional length with a contact probe;

w_g is the groove width;

w_t is the tooth width;

Δl is the offset respect to the real surface of the object;

The step gauges were scanned five times for each instrument involved in the analysis.

10.2 Results

Before reporting the results obtained, in *Table 20*, the summary of results in terms of success or failure of the step gauges acquisition is shown. Results are divided in cooperative and non-cooperative, reminding to the description of the surface characteristics, typical of 3D optical scanning systems, where cooperative surfaces are those characterized by Lambertian reflectance, while non-cooperative are those surfaces characterized by reflective or translucent properties. As it is possible to observe from the data reported in *Table 20*, the colour-less step gauge resulted to be not cooperative with all the instruments involved.

Table 20 Summary of results in terms of success or failure of the step gauges acquisition.

3D scanner / Step gauge	SLS	LLS	PSSRT
POM-C#1	NOT COOPERATIVE	NOT COOPERATIVE	NOT COOPERATIVE
ABS-G#1	COOPERATIVE	COOPERATIVE	NOT COOPERATIVE
PPS-N#7	COOPERATIVE	COOPERATIVE	COOPERATIVE
POM-B#1	NOT COOPERATIVE	NOT COOPERATIVE	NOT COOPERATIVE
PK-B#1	COOPERATIVE	COOPERATIVE	NOT COOPERATIVE

The analysis of the acquired surfaces, in the form of polygonised mesh, were analysed with the GOM inspect software, and the distances between the groove sides were computed as distances between corresponding points on each groove side.
Before computing the resulting errors, temperature compensation must be done for the LLS and PSSRT scanners. Indeed, temperatures registered were, respectively, 23,5° and 21,5°. While during the scan with SLS the temperature was stable to 20°. Humidity was also registered and it was ranging within 48-50% for the SLS, while it was not detectable for the LLS and PSSRT, although, a humidity compensation was not carried out in this investigation, due to the unknown behaviour of those materials respect to the humidity.
Results obtained considering the error evaluated on bidirectional lengths are reported for each step gauge in *Figure 89, Figure 88* and *Figure 87*. Errors are computed as difference between the average value measured over five repetitions, for each instrument, and the calibrated value, see Annex 2.

$$Error = \frac{\sum_i^n \bar{X}_J}{n} - \overline{X_{cal}} \qquad (10.3)$$

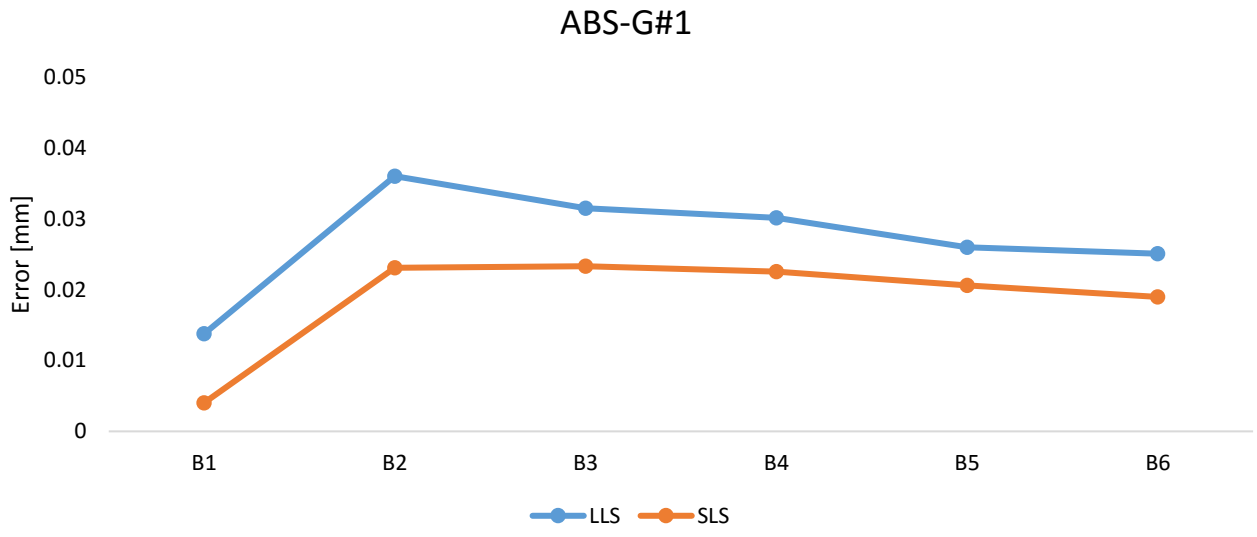

Figure 87 Results obtained for the ABS step gauge.

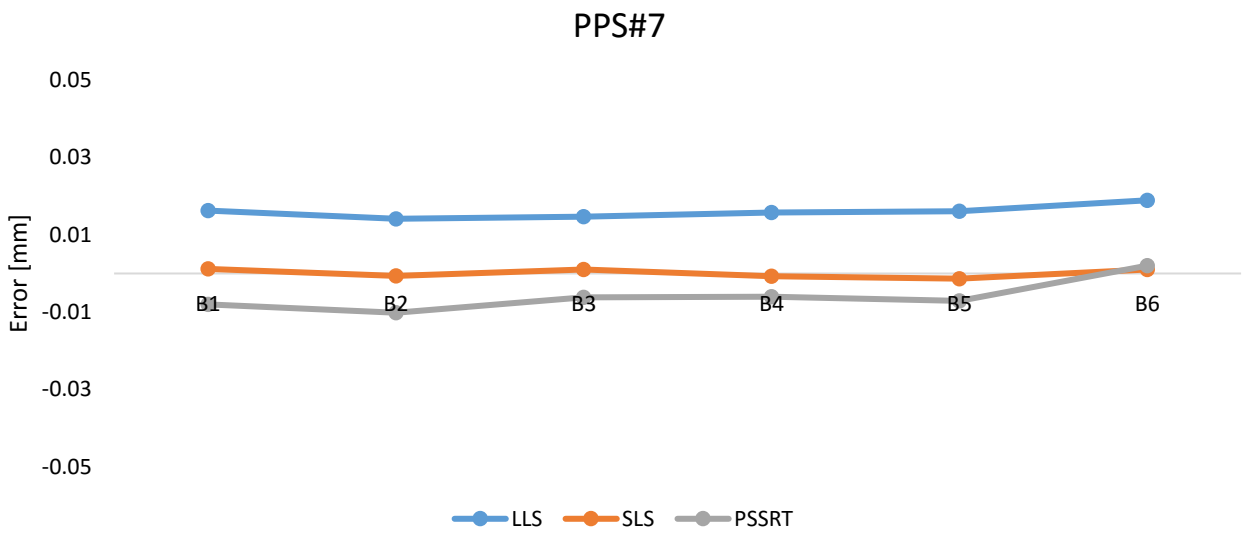

Figure 88 Results obtained for the PPS step gauge.

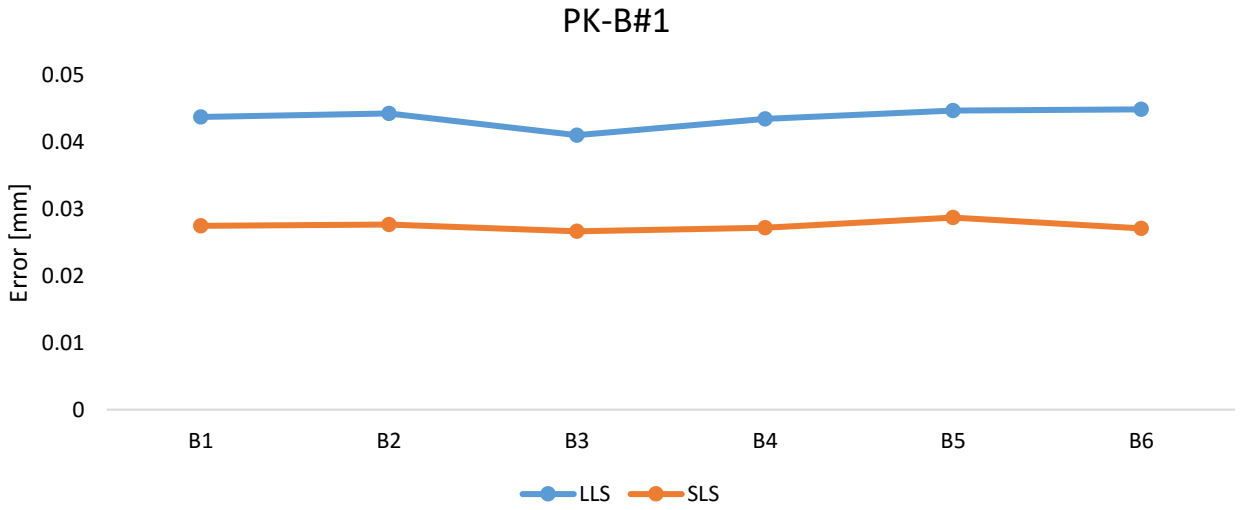

Figure 89 Results obtained for the PEEK step gauge.

From results obtained considering the bidirectional distances, it can be observed that SLS is less sensitive to the step gauge optical properties, with an offset of about 0,01 mm between SLS and LLS. PSSRT resulted to have an offset, which have opposite sign respect to the others. In this case, the optical effect seems to be the opposite of the light penetration.
Different are the errors registered on unidirectional lengths, see *Figure 90, Figure 91, Figure 92*, whose values are much lower, within ±0,005 mm, according to their definition, Eq. (10.1).

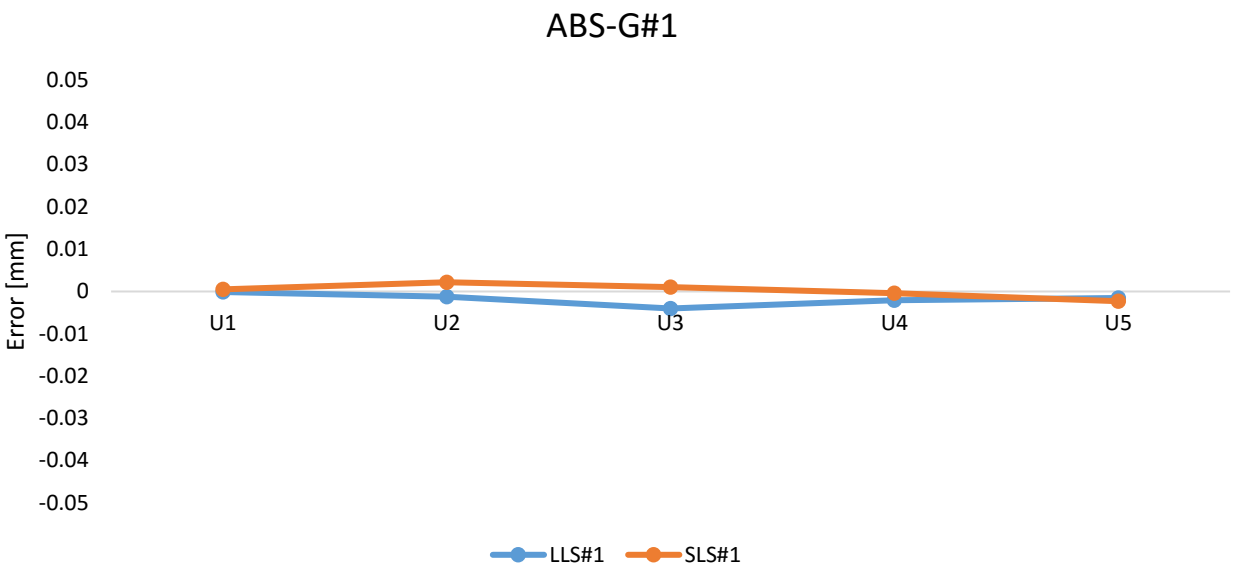

Figure 90 Errors on unidirectional lengths for the step gauge ABS-G#1.

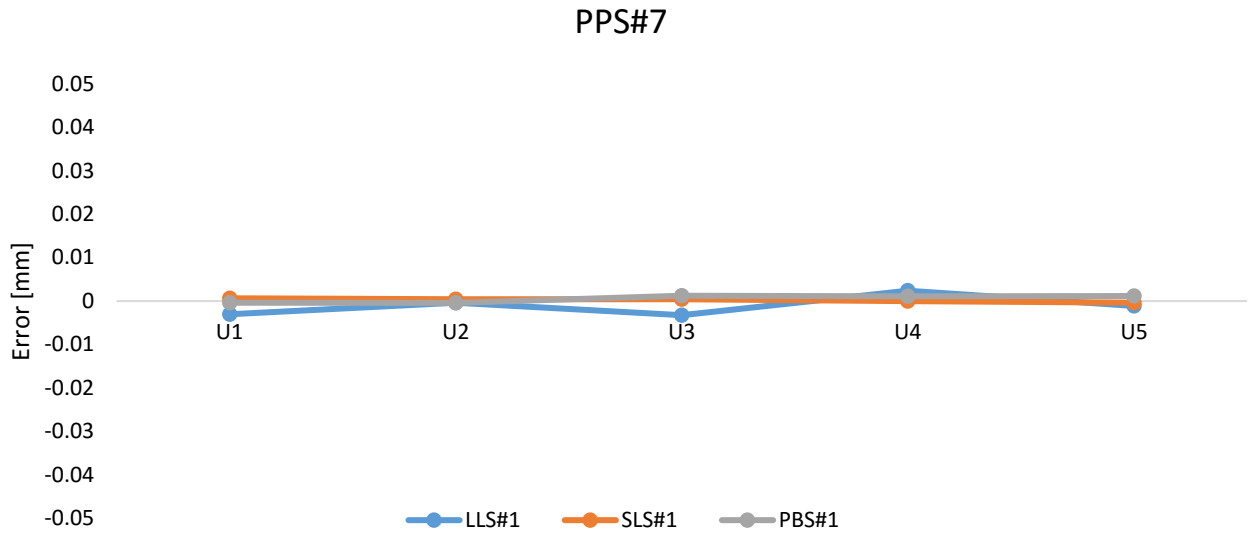

Figure 91 Errors on unidirectional lengths for the step gauge PPS#7.

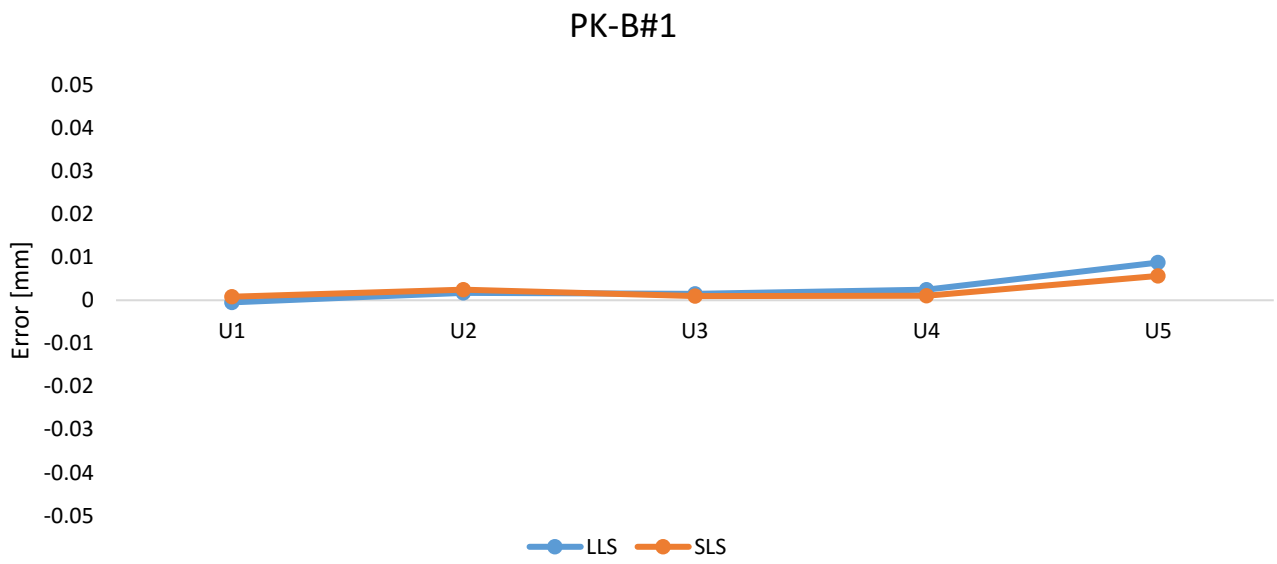

Figure 92 Errors on unidirectional lengths for the step gauge PK-B#1

10.3 Conclusion

In this chapter four step gauges, made of different materials and colours were scanned and measured with three different 3D optical scanners, with the aim to investigate their interactions. The latter were evaluated considering bidirectional lengths measured on the step gauges. Results put in evidence a sensitivity to the surface optical properties up to 0,045 mm for LLS, while for the SLS this value was up to maximum 0,025 mm. Different was the behaviour of the PSSRT, whose deviations had the opposite sign respect to the others and the value of the offset was up to 0,01 mm. The results obtained for the PSSRT refer just to one step gauge, the one made of PPS, all the others presented non-cooperative characteristics for that scanner.

Chapter 11 - Experimental Investigation on Camera Calibration with Magnifications up to 2.4x

In this chapter, photogrammetry was used at high magnification levels for measuring micro feature. Experiments were conducted with a 60 mm macro lens, equipped with the combination of three extension tubes, corresponding to 2,06, 2,23 and 2,4 magnification levels, respectively. Attention was paid to the internal orientation and experiments were carried out to test their robustness and their variability for each configuration. For this purpose, two artefacts with different geometrical complexity were measured and analyzed. Despite the differences in the calibration Reprojection Error (RE), the quality of the photogrammetric 3D reconstruction retrieved was stable and satisfying.

11.1 Materials and Methods

Photogrammetry can be used for the measurement of small objects with micro-feature, with good results and lower cost, compared to other established techniques such as interferometry, conoscopic holography, and 3D microscopy. Calibration is a critical step in photogrammetry and the classical pinhole camera model has been tested for magnifications lower than 2x. At higher magnification levels, because of the reduction of the Depth of Field (DOF), calibration data, even if they are characterized by low Reprojection errors, could lead to bad results in terms of 3D reconstruction. The investigation conducted in this chapter, verified the possibility of applying the camera model to magnifications higher than 2x.

11.1.1 Optical equipment

The experiment was conducted using a digital reflex camera Canon Eos 400D with a 10 Megapixel resolution (3888x2592 pixel^2) and a APS-C CMOS sensor (22,2x14,8 mm^2). A Canon EF-S 60 mm F2,8 macro lens, with the focus distance set to its minimum value, was used adding extension tubes to obtain 44 mm, 52 mm and 60 mm of total extension. The configurations obtained correspond to lateral resolutions of 2,9- 2,7-2,4 μm, vertical resolutions of 5,8 - 5,4 - 4,8 μm, and magnification levels (M) of 2,06x, 2,23x and 2,4x.

11.1.2 Calibration pattern

For the experiments, the open source software library Open CV, was used together with a symmetric calibration pattern with 22 columns and 18 rows of photoetched dots (chrome on glass) as shown in *Figure 93*. Preliminary studies [28] established that patterns with circular dots are preferable because they are less sensitive to blurring than calibration checkerboard, allowing the recognition of the dots when they are not in focus.

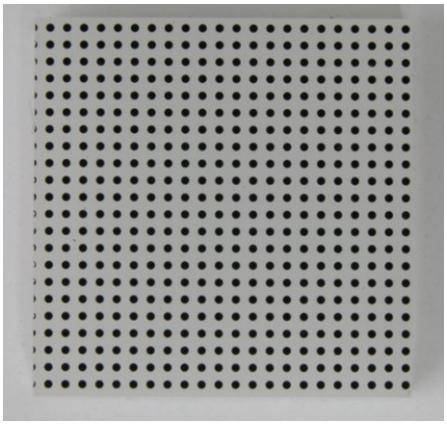

Figure 93 Symmetric pattern with dots of 0,25 mm and distances between centres of 0,5 mm.

Five sets of photographs were acquired for each configuration of macro lens and extension tubes and processed using the functions of the OpenCV library [29], version 2.4.11, for the estimation of the intrinsic parameters. Each calibration set consists of 24 images obtained by tilting the pattern gradually along the three axis, taking care to keep the centre in focus, according to [30]. OpenCV calibration tool runs an automatic dot recognition procedure. The recognition of dots is based on the well-known OpenCV BLOB- (Binary Large Object) detection method. This consists of calculating the centroids of the connected blob, with subpixel precision. In addition, blob-detection method allows filtration of returned blobs by colour, area, circularity, etc. The OpenCV source code was corrected in order to deal with higher resolution images.

11.1.3 Test objects

Test objects were selected to test the system under different conditions. Test object 1 was selected because of its sharp edges on a regular geometry and the micro etching on the top, while test object 2 was a gear wheel selected due to its concave geometry and the micro details. The manufacturing technology chosen was Electro Discharge Machining for its capability to generate textured surfaces-very appropriate for photogrammetry, *Table 21* .

Table 21 Test objects realized by µEDM.

Test objects	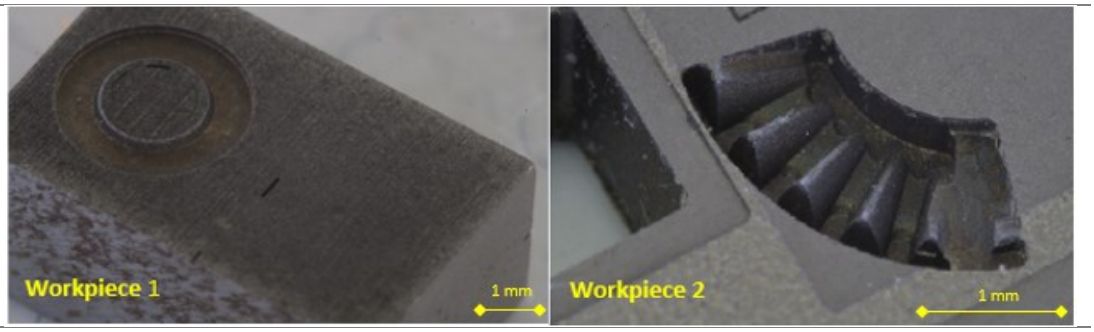

Manufacturing Process	Electro Discharge Machining	Electro Discharge Machining
Geometrical characteristic	geometrically regular feature with sharp edges and a micro etching on the top	concave geometry and micro details

A reference model of both test objects was retrieved using an optical profilometer Taylor Hobson CCI MP-HS, equipped 10x, which means an optical resolution of 1,3 µm. A stitching scan was necessary because the size along x and y axis exceeded the field of view of the single patch, *Figure 94* and *Figure 95*.

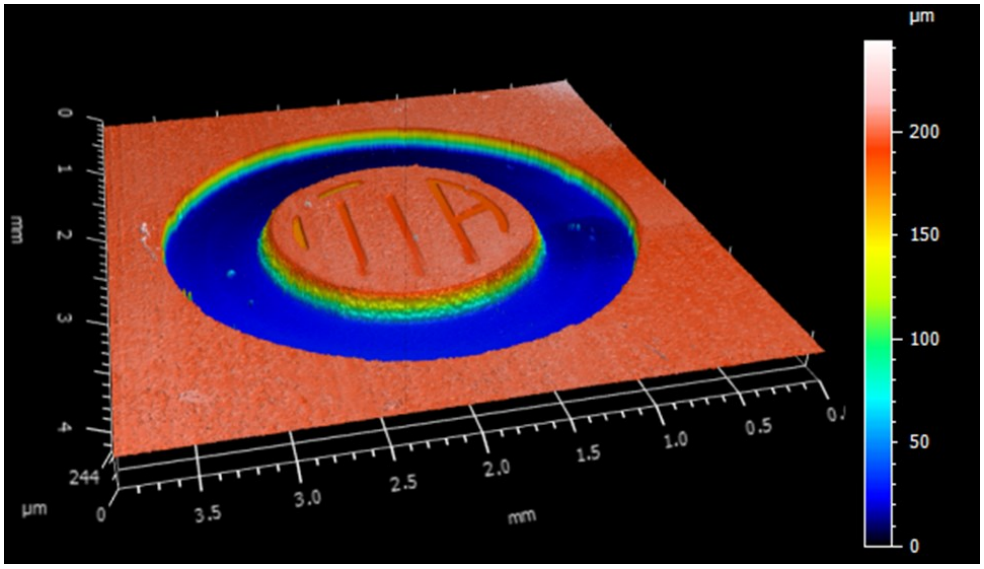

Figure 94 Test object 1 scanned with the reference instrument [104].

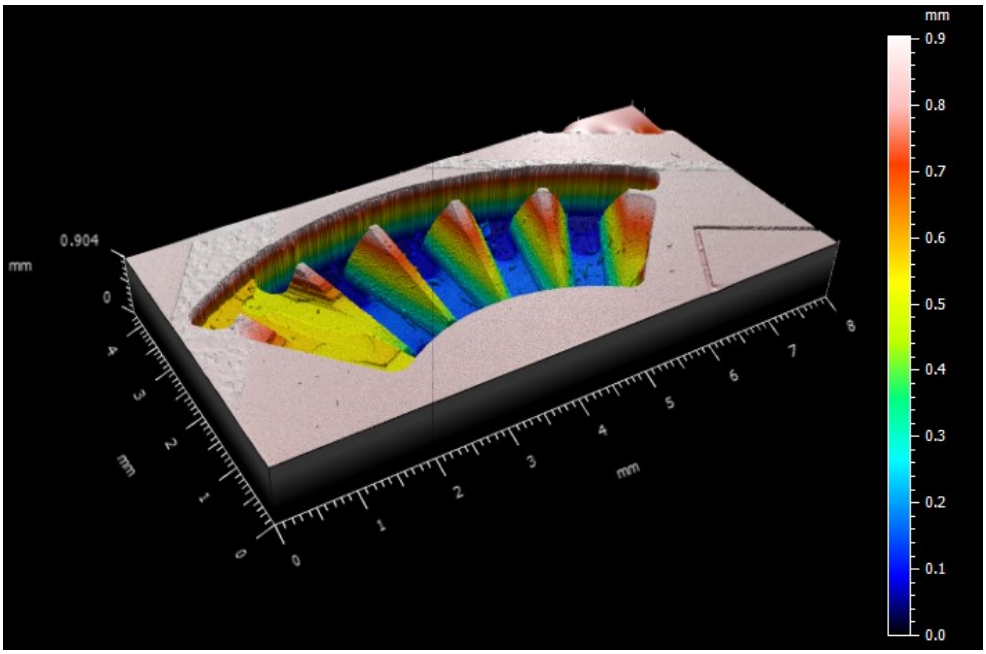

Figure 95 Test object 2 scanned with the reference instrument [104].

11.1.4 Scanning strategy

The test object was positioned at the centre of a rotary table ISEL-RFII, with an angular position resolution equal to 3°. A proper illumination was ensured by a white box illuminated from all sides with a led strip which rotates solidly with the rotary table. During the image acquisition, according to [31], the rotation angle of the table was set at 5° and the camera was tilted with respect to the table at 45°. This choice was the best trade-off for both objects, which are geometrically different.
Agisoft Photoscan, software version 1.1.6, was used for the image processing using the fixed internal calibration, pre-computed with the aid of the OpenCV library software.

11.2 Results

11.2.1 Camera calibration results

In the experimentation, five calibration certificates were realized for each configuration lens-extension tube to evaluate the repeatability of the methodology adopted.
The first configuration involves the use of a 44 mm extension, obtained as the sum of a 20 mm extension tube and two 12 mm extension tubes, see *Table 22*.

Table 22 Camera calibration parameters for M=2,06 x.

Camera calibration parameters with M=2,06x (lateral resolution 2,9 μm, vertical resolution 5,8 μm)										
Set	**R.E. (px)**	**F_x (px)**	**F_y(px)**	**C_x(px)**	**C_y(px)**	**k_1**	**k_2**	**k_3**	**p_1**	**p_2**
1	0,4263	65870,69	65880,77	2065,16	1307,12	1,595	360,74	0,496	0,001	0,004
2	0,4155	65564,57	65608,18	1961,60	1989,38	2,008	-173,12	-0,355	-0,002	-0,005
3	0,6427	65851,69	65839,04	1298,78	1369,82	1,578	185,36	0,254	0,002	-0,021
4	0,4838	65778,12	65804,27	1895,61	1837,24	2,284	-305,83	-0,593	0,018	-0,001
5	0,3214	65686,86	65712,28	1938,61	1811,21	2,112	-228,71	-0,392	0,018	0,001

The second and the third configurations, reported in *Table 23* and *Table 24*, are characterized by 52 mm and 60 mm respectively, with 32 mm plus 20 mm and 36 mm plus two 12 mm extension tubes.

Table 23 Camera calibration parameters for M=2,23 x.

Camera calibration parameters with M=2,23x (lateral resolution 2,7 μm, vertical resolution 5,4 μm)										
Set	**R.E. (px)**	**F_x (px)**	**F_y(px)**	**C_x(px)**	**C_y(px)**	**k_1**	**k_2**	**k_3**	**p_1**	**p_2**
1	0,4947	70223,93	70238,77	1375,52	1718,93	1,787	188,36	0,217	0,014	-0,016
2	0,2184	70599,25	70631,25	1791,18	1238,46	1,427	603,09	0,787	-0,002	-0,005
3	0,1739	70367,70	70402,56	1877,66	1281,65	1,518	474,45	0,607	0,001	-0,002
4	0,494	70391,10	70386,92	2311,47	1297,78	1,962	-32,24	-0,073	-0,002	-0,013
5	0,5621	70381,50	70380,16	2365,07	1308,94	1,979	-121,93	-0,181	0,003	0,014

Table 24 Camera calibration parameters for M=2,4 x.

Camera calibration parameters with M=2,4 x (lateral resolution 2,4 µm, vertical resolution 4,9 µm)										
Set	**R.E. (px)**	**F_x (px)**	**F_y(px)**	**C_x(px)**	**C_y(px)**	**k_1**	**k_2**	**k_3**	**p_1**	**p_2**
1	0,3451	77045,94	77037,73	1614,08	1430,8	1,950	120,69	0,1589	0,0042	-0,0079
2	0,7374	77888,89	77920,03	2138,93	1823,54	2,530	-467,31	-0,6368	0,0163	0,0069
3	0,6374	77804,52	77854,23	2109,72	2060,41	2,898	-744,12	0,0239	0,0239	0,0063
4	0,785	77133,61	77161,3	2243,69	1000,44	1,570	464,91	0,6688	-0,0108	0,0107
5	0,7201	77327,01	77337,6	1934,02	1643,74	2,055	-1,203	-0,0021	0,0092	0,0008

The data reported in *Figure 96* put in evidence the stability of the focal length parameters in all the conditions. The standard deviation computed over the five iterations resulted less than 0,2%, with a maximum value of 0,5% for the 60mm configuration. Conversely, the position of the principal point identified by Cx and Cy coordinates, highlighted higher variations since its correlation with the tangential distortion parameters, p1 and p2, is widely known [105].
This type of correlation is essentially caused by the polynomial representation of the calibration model, consisting of solving a hyper-linked equation system leading to a high sensitivity of the principal point coordinates values as the tangential distortion values change and vice versa. Moreover, it can be appreciated that when principal points in two different rows are similar, then the estimated radial and tangential distortions parameters are also similar.

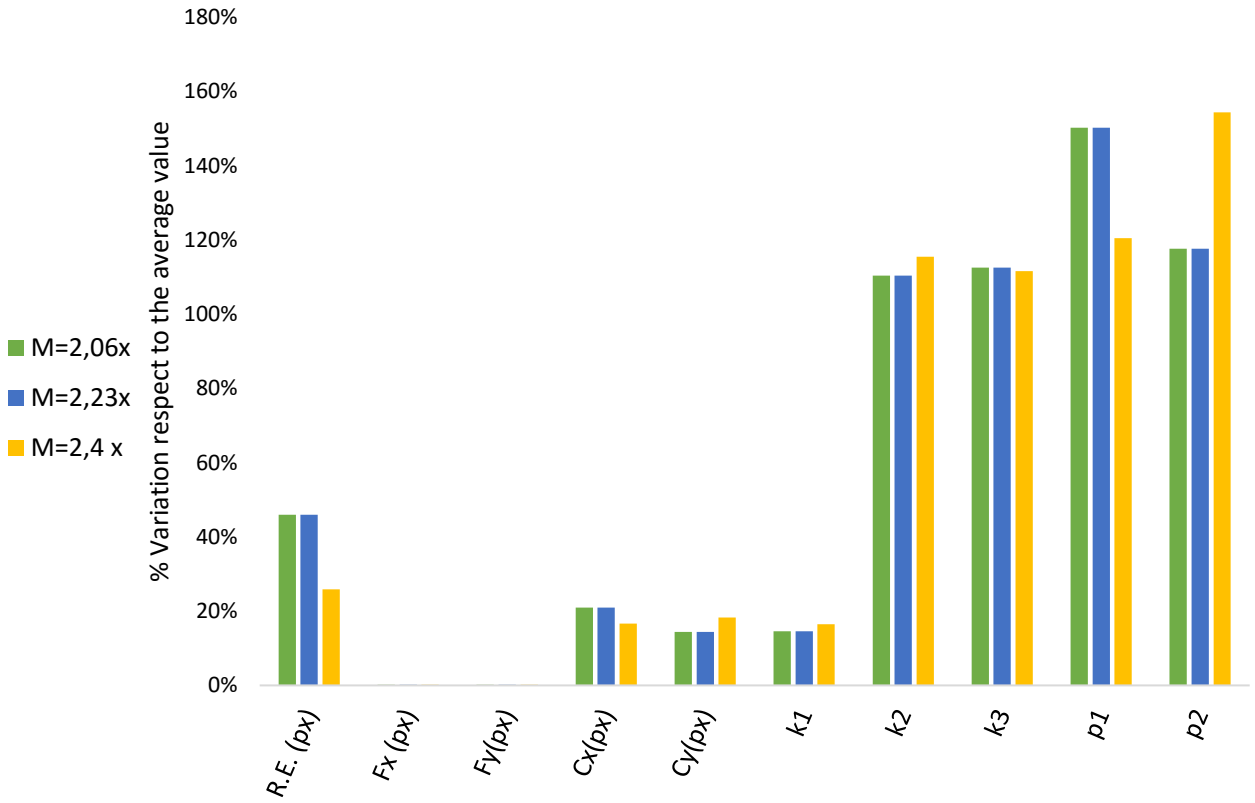

Figure 96 Variation in % of each internal parameter throughout the five repetitions.

11.2.2 Results from 3D reconstruction

For each workpiece, a 3D reconstruction in the form of polygonal mesh was retrieved for each calibration set (achieving a textured mesh of the object for each calibration certificate) and compared to the reference model. The comparison was accomplished after an Iterative Closest Point (ICP) procedure, with the commercial software Geomagic Control.
After the image processing there was still a parameter unsolved: the scale factor. During the photogrammetric alignment, this value is assumed as a random parameter whose value can change at each processing, with the same input data and conditions. The scale was computed by exploiting one method programmed into the open source software, MeshLab [34]. This software allows to scale a model with respect to another one, choosing a number of homologous points to match.
At each iteration of the Iteration Closest Point (ICP) algorithm, the software computes the transformation matrix for roto-translation and the scale factor for the photogrammetric mesh to match the reference one, minimizing the Euclidean distance between homologous points.
If more points are chosen and lower is the original difference in scale between the two models, the scaling process will be more accurate.
Data from the 3D comparisons were obtained through the commercial software Geomagic Control after a new best-fit alignment between the reference model and the photogrammetric model (test). In the colored map, resulted from the 3D Comparison analysis, each point of the test is associated with a distance from the homologous point on the reference and the distances are clustered into colored intervals, according to the legend associated, see *Figure 97* and *Figure 98*. The number of points effectively compared was about 350000 points, while number of discarded points is around 500 points and rose up to 1000 points in some cases.

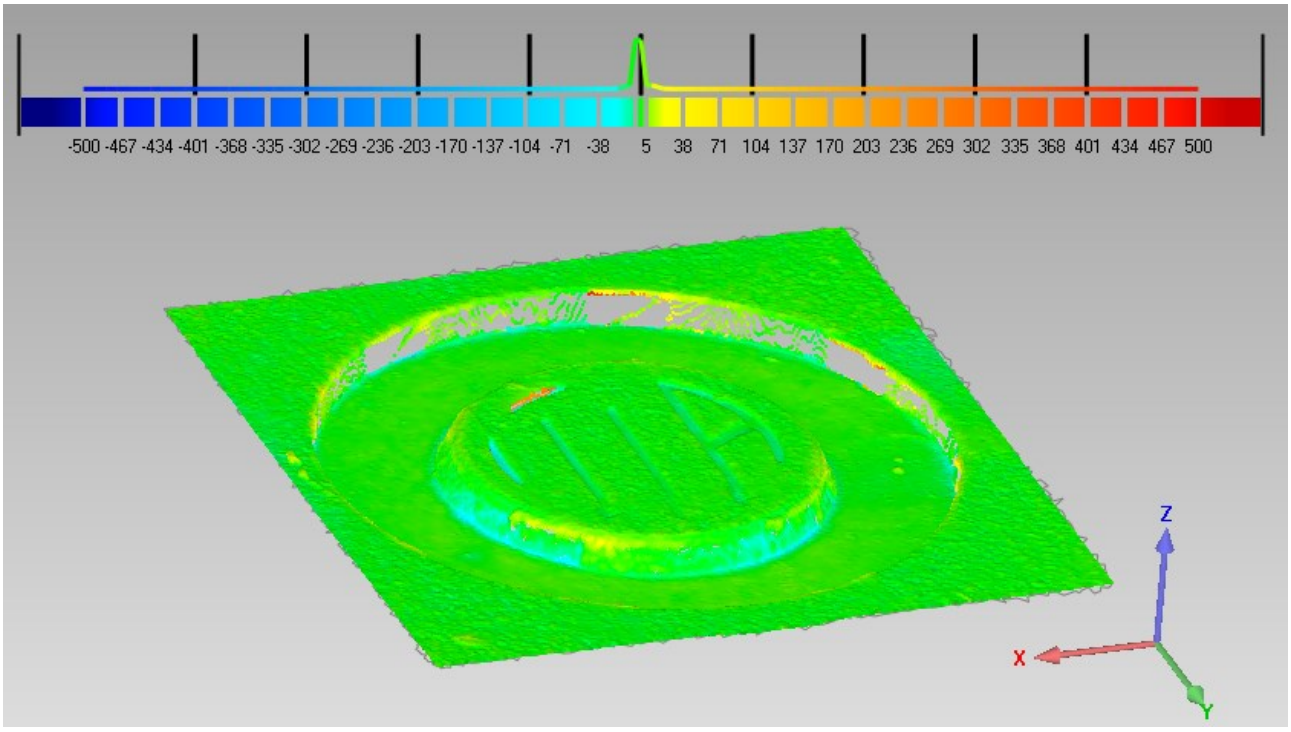

Figure 97 3D Comparison of test object 1 [104].

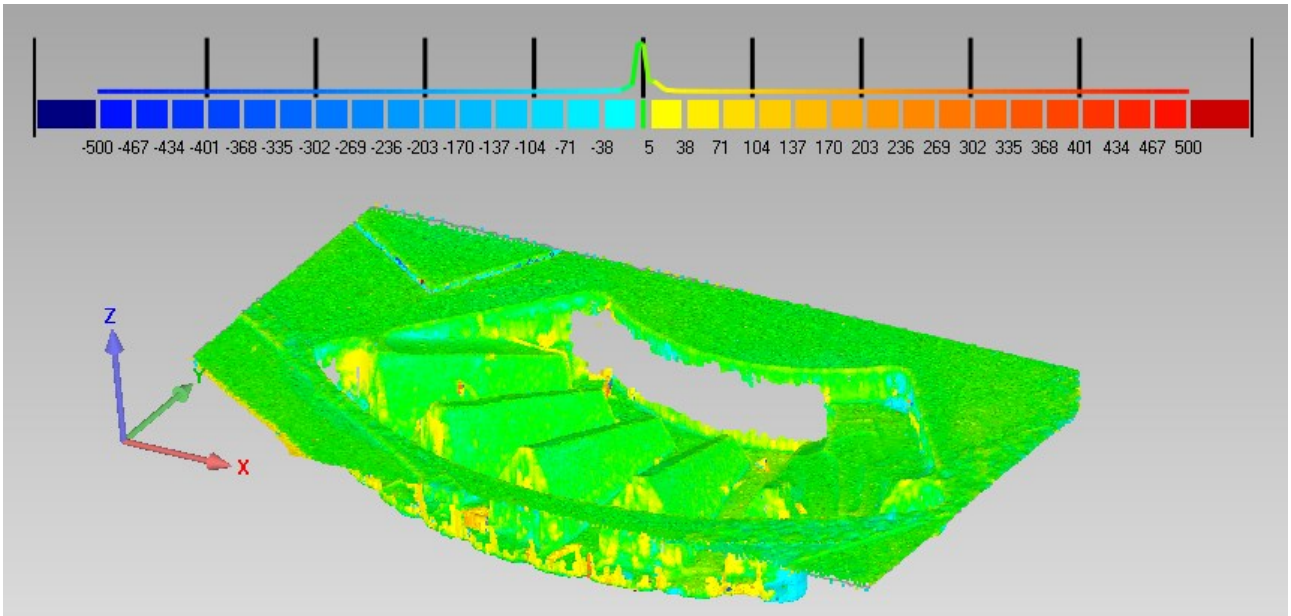

Figure 98 3D comparison of test object 2 [104].

In *Figure 99*, the distance between the reference model and the test models are reported for each magnification level used and each calibration set.

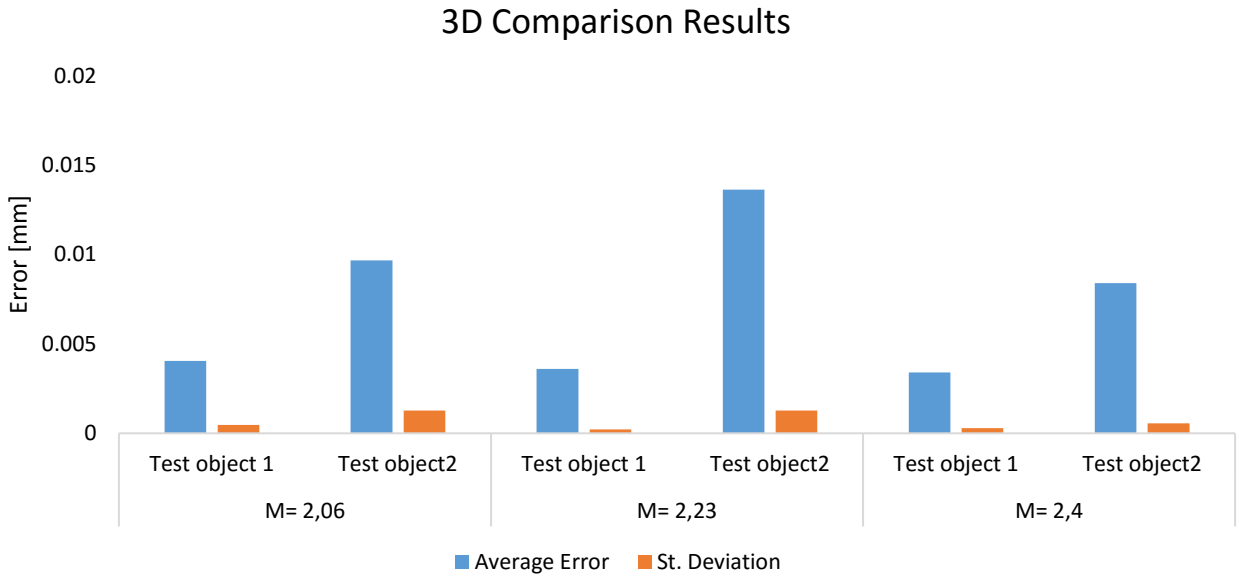

Figure 99 3D Comparison results.

In general, both reconstructions led to good results, see *Figure 99*, with average deviations of few micrometers for test object 1 and 10 µm for test object 2. A direct influence of the calibration set was not evident, being the maximum variabilities for each object and each magnification level (extension tubes, in the pictures) lower than 5 µm. It must be underlined that all the calibrations achieved a sub-pixel Reprojection error. Graphs reported in *Figure 100-Figure 101-Figure 102*, were obtained from the association of a normal distribution to data registered from each configuration, having average equal to the average error registered respect to the reference model, and as standard deviation, the standard deviation of the errors throughout the five repetitions.

The difference registered for the two objects was due to the different geometrical complexity of the artefacts.

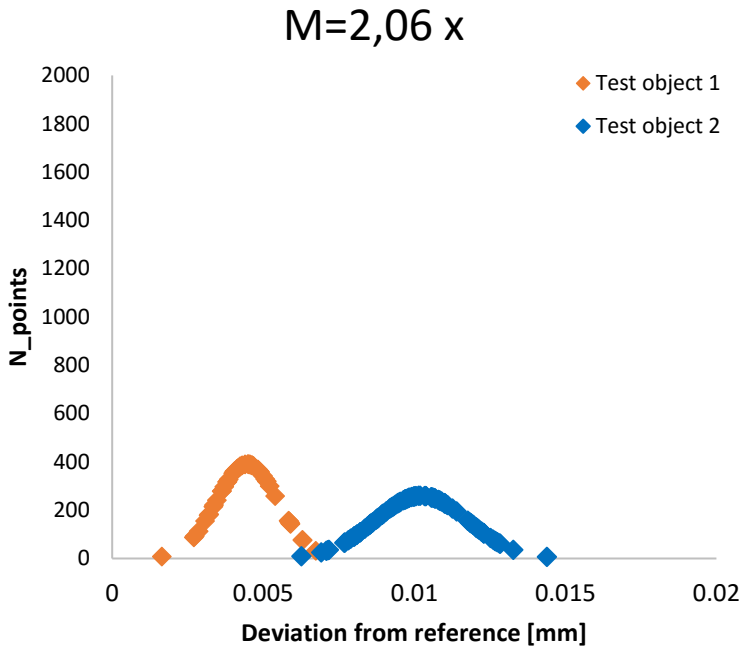

Figure 100 Normal distribution associated with M=2,06x.

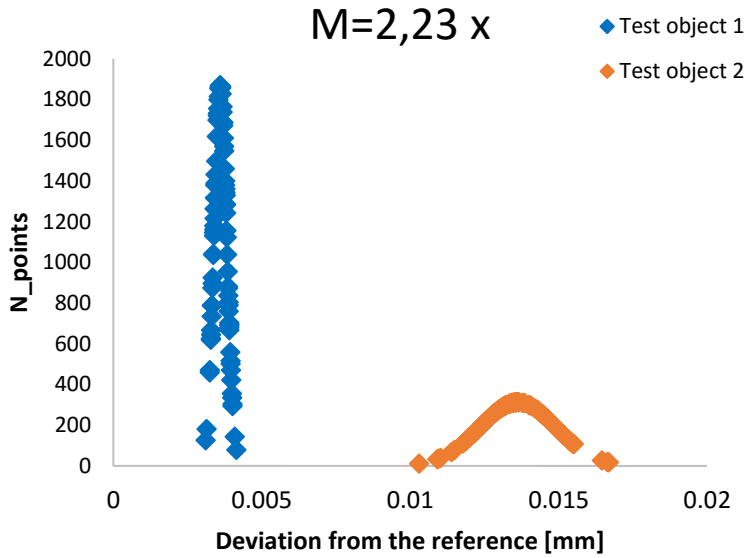

Figure 101 Normal distribution associated with M=2,23x

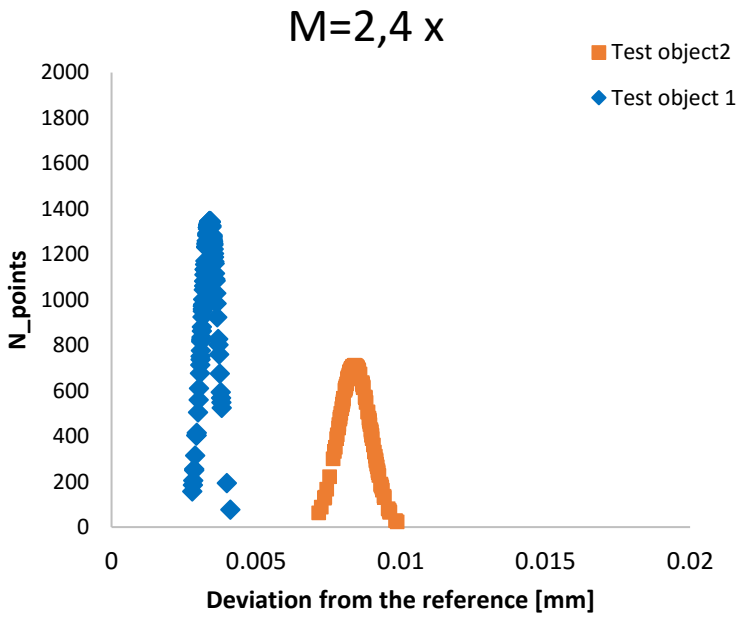

Figure 102 Normal distribution associated with M=2,4x

Test object 1 has the maximum depth equal to 244 µm; the test object 2, instead, has a very complex geometry because of its pronounced concavity (with maximum depth of 904 µm), which also made the penetration of light difficult.
The colored maps, presented in *Figure 97- Figure 98*, put in evidence that, for the test object 2, the highest deviation values were in correspondence of the outlying areas with the highest values of depth. This effect was more pronounced for the first two configurations, with slightly lower magnification levels and a lower capability of light to achieve the deepest areas, considering the difficulty of light-penetration. However, the best results were obtained for both artefacts, with the highest magnification level, with errors below 3 µm for test object 1 and slightly lower than 10 µm for test object 2. This result confirmed the effectiveness of the camera calibration model implemented even if the magnification level is more than 2x, situation characterized by a consistent reduction of the angle of view.

11.3 Conclusion

In this chapter, the stability of the traditional mathematical models for the estimation of the internal parameters characterizing the camera model was analysed for magnification levels higher than 2x. Tests were performed through two artefacts manufactured with µEDM. Results put in evidence a good stability of the internal parameters evaluated on the 3D reconstruction results and through the 3D comparisons with a reference model, with errors in the order of few micrometers for the optical configuration showing the better optical resolution equal to 2,4 µm.

Conclusions

The present thesis dealt with the development and the analysis of an optical 3D scanner based on photogrammetry, the PSSRT, with the aim to investigate its suitability for the measurement of industrial components in close and micro range. The PSSRT and, more generically, the photogrammetry based system, resulted to be in line with the needs of manufacturing metrology 4.0 in terms of flexible, reliable, holistic and fast measuring systems.

The system implemented resulted to be very flexible, since it was used from close to micro range, just changing the sensor and the optical equipment. APS-C and Full frame sensors were used equipped for magnification levels ranging from 0,3x to 2,4x to which a ground resolution of 0,012 mm and 0,0024 mm corresponds, respectively. The results obtained in terms of measuring reproducibility were in the order of few micrometers for each measuring set-up, when object with good visual texture characteristics were scanned. These two components, measuring reproducibility and resolution, define the characteristics of the measurement uncertainty attributable to the measuring instruments itself.

The scale adjustment, which is considered a great limitation of a photogrammetry-based system, was improved using a 3D reference object, instead of a bidimensional pattern of target, for the computation of the external orientation. From the calibration of the system carried out through the staircase artefact (Chapter 6) and through the miniature step gauge (Chapter 9) the PSSRT showed errors less than 0,005 mm. The uncertainty assessment was found to be greatly affected by the form error of the reference artefacts (about the 60% of the expanded uncertainty) and by the meshing process. Mostly negligible was evaluated the uncertainty component related to the repeatability of the reconstruction software. Generally, it resulted to affect the expanded uncertainty in term of statistical reproducibility of the measuring system, only when the scanning conditions were not favourable, considering the test object geometry and its visual texture.
All the results obtained in terms of errors and in terms of uncertainty are in line with the currently available non-contact measuring systems adopted in close range and in particular, the PSSRT resulted to be comparable with the structured light scanner.
Although, there are still other aspects that affect the reliability of this kind of system. The visual and tactile texture resulted to greatly affect the measuring results. The visual texture and the material characteristics, which define the optical interaction between the measuring instrument and the object, were evaluated exploiting the step gauge geometry. The analysis was extended to other two 3D optical scanners and results highlighted different effects, depending on the material and colour and on the 3D optical scanner considered. The consequence of the material and colour interaction with the optical instrument adopted was ranging from 0,025 mm to 0,045 mm, up to 2,25% of the measured value. The effect due to the visual texture was also observed when the PSSRT was applied for the measurement of the micro-fluidic devices made through additive manufacturing technologies. Errors estimated respect to the reference model were ranging from 0,01 mm for the devices showing the best visual texture characteristics up to 0,03 mm for the worst cases.

Based on these results, a fundamental consideration is that, when dealing with optical systems, all the results must be considered referred to the specific measuring equipment, the specific

object and the specific environmental conditions, or to summarize, to the specific measuring task. The generalization is not possible due to the sensitivity of such a system to the so called “boundary conditions”. This is also the main reason for the lack of standardized procedures for the metrological characterization of 3D optical scanning systems.
The accuracy and the uncertainty cannot be summarized in a single value, but a value must be used for each measuring task.

Outlooks

The investigations and the achievements of the present work have contributed to the analysis of the photogrammetry applied to close and micro range. The potentialities of the system were investigated together with its weaknesses. From results obtained, new challenges arouse, and further researches will be undertaken:

- The reconstruction software is a fundamental part of the photogrammetric reconstruction process. In this thesis, an approach to evaluate the effect of its repeatability under specific conditions was developed and it could be further applied when using the system under different operating conditions, which involve different geometries, scanning strategies, and scale adjustment procedures;
- The scale adjustment resulted to be improved from the implementation of a 3D reference artefact for the estimation of the external orientation, together with the scale factor. Although, this method is limited by the necessity of fabricating a reference object, which should have dimensional similarity requirements with the actual part which needs to be measured. New methods will be implemented, exploiting the automation and the control of the motorized system for the acquisition and the use of encoders for the computation of the mutual positions between the sensor and the object;
- When applying the system for the measurement of the step gauge reference object, the effect of the depth of field was easily detected, thanks to the peculiar geometry of the step gauge. Further investigations will be carried out with the aim to quantify how this effect is influenced by the optical configuration and the scanning strategy;
- A preliminary study was conducted for the evaluation of the interaction between different materials and colours and the optical measuring instrument. Results obtained highlighted the presence of this effect and how it differs according to optical instrument involved. Further investigation will be carried out with the aim to quantify and, eventually, compensate for this effect;
- The photogrammetry-based system, was also found to be suitable for the measurements of additive manufactured parts. Indeed, the main difficult encountered, was related to the dimensional verification of artefacts realized by filament-based technologies, like FDM due to their typical surface texture. A further development of this research, will be addressed to the evaluation of the influence of the surface texture, typically obtained through additive filament-based techniques, on different measuring instruments. With this aim, measuring systems, exploiting different measuring principles, contact and non-contact will be considered. Among the non-contact, the resolution of the system will be the key parameter for the investigation;
- The application of photogrammetry to the microscopic range was tested up to a magnification level of 2,4x. Considering the reduced distance between the sensor and the object, the encumbrance of the sensor as well as the limited depth of field, the limit of the applicability of this kind of system in the microscopic range will be explored;
- Starting from the assumption that all the results obtained within this thesis have to be considered specifically related to the measuring task investigated, it will be possible to create a collection of the results obtained for each measuring task, which involve the object characteristics (main dimensions, geometry, material and texture), as well as, the

measuring equipment (sensor, optical equipment, resolution), the scanning strategy, the reconstruction software and the environmental conditions. This will aid the potential users of the system to understand the main potentialities, as well as, the limits of the system.

Appendix

Appendix 1

The *mean*, the *standard deviation* and the *percentage variation* of each internal parameter are shown at the first three rows.
The term Δ(u,v) represents the total variation of the (u,v) projected point due to the combined variation of all the internal parameters and it has been computed for each configuration.

Table A1 *Internal parameters statistics and associated repeatability computed for each configuration involved.*

Internal parameters statistics - Configuration **I** P, L, High							
Parameter	**F_x(px)**	**F_y(px)**	**C_x (px)**	**C_y(px)**	**K_1**	**K_2**	**K_3**
Mean	14973,700	14973,700	1947,537	1318,127	-0,325	1,027	-10,892
St, Dev - **S_i**	2,685	2,685	1,349	2,655	0,003	0,212	6,054
Δ%	0,018%	0,018%	0,069%	0,201%	-0,861%	20,629%	-55,583%
Δ $(u,v)_i$[px]	1,033E-04	1,033E-04	3,989E-04	1,210E-03	1,612E-05	1,221E-03	4,997E-04
Δ $(u,v)_t$	1,841E-03 [pixel]			1,583E-05 [mm]			
Internal parameters statistics - Configuration **I** P,L, Low							
Parameter	**F_x(px)**	**F_y(px)**	**C_x(px)**	**C_y(px)**	**K_1**	**K_2**	**K_3**
Mean	14961,733	14961,733	1985,097	1311,913	-0,265	-2,970	118,395
St, Dev	3,528	3,528	2,709	1,804	0,018	1,472	37,085
Δ%	0,024%	0,024%	0,136%	0,138%	-6,730%	-49,557%	31,323%
Δ (u,v)[pixel]	1,357E-04	1,357E-04	8,012E-04	8,225E-04	1,029E-04	8,489E-03	3,061E-03
Δ $(u,v)_t$	9,100E-03 [pixel]			7,826E-05 [mm]			
Internal parameters statistics - Configuration **II** P,L, High							
Parameter	**F_x(px)**	**F_y(px)**	**C_x(px)**	**C_y(px)**	**K_1**	**K_2**	**K_3**
Mean	14958,613	14958,605	2027,663	1288,956	-0,206	-5,283	204,707
St, Dev	6,703	6,693	2,276	9,584	0,004	0,236	19,943
Δ%	0,045%	0,045%	0,112%	0,744%	-1,877%	-4,468%	9,742%
Δ (u,v)[pixel]	2,577E-04	2,577E-04	6,731E-04	2,199E-06	2,228E-05	1,362E-03	1,646E-03
Δ $(u,v)_t$	2,269E-03 [pixel]			1,952E-05 [mm]			
Internal parameters statistics - Configuration **II** P,L, Low							
Parameter	**F_x(px)**	**F_y(px)**	**C_x(px)**	**C_y(px)**	**K_1**	**K_2**	**K_3**
Mean	14929,433	14929,433	2027,680	1345,623	-0,201	-8,718	330,674
St, Dev	5,953	5,953	2,766	7,854	0,004	0,088	6,591
Δ%	0,040%	0,040%	0,136%	0,584%	-1,785%	-1,006%	1,993%
Δ (u,v)[pixel]	2,291E-04	2,291E-04	8,181E-04	3,580E-03	2,068E-05	5,060E-04	5,441E-04
Δ $(u,v)_t$	3,761E-03 [pixel]			3,234E-05 [mm]			
Internal parameters statistics - Configuration **III** P,L, High							

Parameter	**F_x(px)**	**F_y(px)**	**C_x(px)**	**C_y(px)**	**K_1**	**K_2**	**K_3**
Mean	14927,436	14925,964	1937,419	1360,726	-0,367	2,969	-75,956
St, Dev	3,925	3,831	2,498	5,663	0,008	0,434	8,355
Δ%	0,026%	0,026%	0,129%	0,416%	-2,135%	14,633%	-11,000%
Δ (u,v)[pixel]	1,492E-04	1,492E-04	7,389E-04	1,231E-06	4,523E-05	2,506E-03	6,897E-04
Δ $(u,v)_t$	2,711E-03 [pixel]			2,331E-05 [mm]			
Internal parameters statistics - Configuration **III** P,L, Low							
Parameter	**F_x(px)**	**F_y(px)**	**C_x(px)**	**C_y(px)**	**K_1**	**K_2**	**K_3**
Mean	14905,039	14905,039	1950,769	1384,986	-0,340	1,084	-26,514
St, Dev	0,561	0,561	4,884	3,315	0,002	0,379	12,026
Δ%	0,004%	0,004%	0,250%	0,239%	-0,718%	34,931%	-45,358%
Δ (u,v)[pixel]	2,157E-05	2,157E-05	1,445E-03	1,511E-03	1,409E-05	2,185E-03	9,927E-04
Δ $(u,v)_t$	3,183E-03 [pixel]			2,737E-05 [mm]			
Internal parameters statistics - Configuration **IV** P,L, High							
Parameter	**F_x(px)**	**F_y(px)**	**C_x(px)**	**C_y(px)**	**K_1**	**K_2**	**K_3**
Mean	15047,445	15047,445	1872,288	992,713	-0,355	12,079	-419,822
St, Dev	93,946	93,946	120,658	349,415	0,156	5,023	200,460
Δ%	0,624%	0,624%	6,444%	35,198%	-43,875%	41,581%	-47,749%
Δ (u,v)[pixel]	3,615E-03	3,615E-03	3,569E-02	1,041E-04	8,974E-04	2,897E-02	1,655E-02
Δ $(u,v)_t$	4,913E-02 [pixel]			4,225E-04 [mm]			
Internal parameters statistics - Configuration **IV** P,L, Low							
Parameter	**F_x(px)**	**F_y(px)**	**C_x(px)**	**C_y(px)**	**K_1**	**K_2**	**K_3**
Mean	14911,355	14911,355	2057,001	1325,644	-0,289	-6,470	237,235
St, Dev	70,817	70,817	118,843	271,472	0,217	17,627	654,987
Δ%	0,475%	0,475%	5,778%	20,478%	-74,930%	-272,446%	276,092%
Δ (u,v)[pixel]	2,725E-03	2,725E-03	3,515E-02	1,237E-01	1,250E-03	1,017E-01	5,407E-02
Δ $(u,v)_t$	1,727E-01 [pixel]			1,485E-03 [mm]			

Appendix 2

This appendix reports the calibration procedure and the measured value of four series of four step gauges used in chapters 9 and 10.

Test Report on four series of miniature step gauges made of polymers

Calibrated object:	4 Series of 5 step gauges
Manufacturer:	DTU Mekanik
Calibration Period:	November 2017
Operator:	Maria Grazia Guerra
Instrument:	Coordinate Measuring Machine (CMM) Zeiss OMC 850, MPE= (2.5+L/300) μm (with L expressed in mm), Brock and Mikkelsen Certificate S012371, calibrated on 26.07.2007
Probe Configuration:	Diameter 0.8 mm and 20 mm long stylus
Length Standard:	Grade I steel blocks were used as length references to generate traceability. DTI Certificate 128.3852, CALIBRATED ON 24.07.1995
Environmental Temperature:	20.0±1°C

Calibrated object

The calibrated object is a miniature step gauge featuring bidirectional and unidirectional lengths (Fig. A2 1).
In total 20 miniature step gauges have been manufactured by milling.

- Five made of *Acrylonitrile butadiene styrene* (ABS) and characterized by a grey color;
- Five made of *Polyoxymethylene* **(**POM) colorless material;
- Five made of *Polyoxymethylene* **(**POM) characterized by a black color;
- Five made of *Polyoxymethylene* **(**POM) and characterized by a blue color.

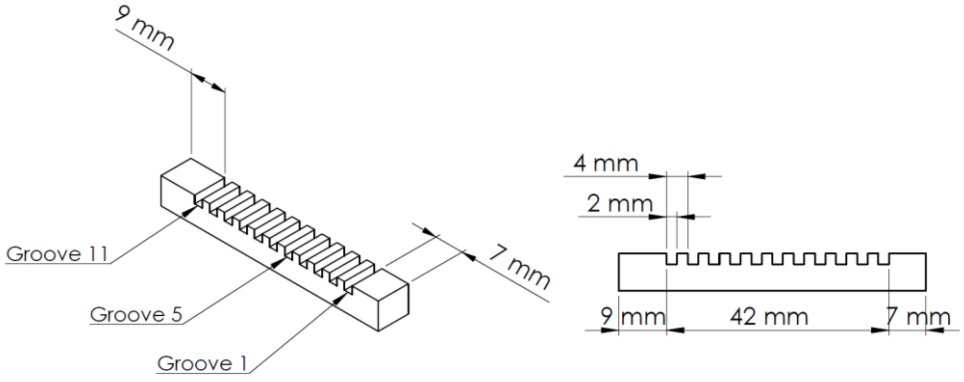

Figure A2 1 Step gauge with nominal dimensions.

Table A2 1 Material characteristics of the step gauges.

Material	Supplier	Grade	Density [g/cm^3]	Thermal Expansion coefficient [10^{-6} K^{-1}]
ABS	Röchling	SUSTAABS	1.07	90
POM	GEHR	GEHR POM-C® (Acetal)	1.39	120

Calibration Procedure

1. Definition of coordinate system

The definition of the coordinate system for the step gauge has been performed using a "3-2-1 alignment". At first, plane Z is created through least square fitting of the top surface of four teeth located between groove 4 and 8. Line X, which identifies X axis and plane YZ, has been defined as a symmetry line from two lines created on the most extreme lateral sides of the step gauges along its longitudinal length. These lines are created by best fitting approach starting from points picked up on the lateral sides above mentioned. Plane X is on the left side of the sixth groove and it has been created through a least square fitting. The reference axis has been defined as reported in Fig. A2 2.

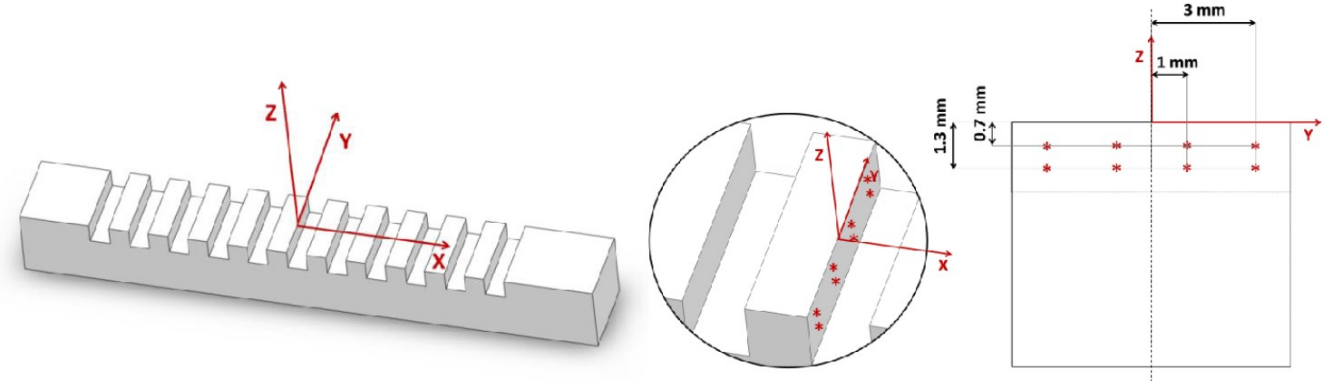

Figure A2 2 Coordinate System Definition.

The measurement strategy of incremental lengths are computed indirectly as the distance between the center points of the corresponding grove planes obtained through a least square fitting of 8 points acquired on each groove side, as it is shown in Fig. 2. All distances are defined as the distance from each side to the left side of groove 1. This leads to a total number of ten incremental unidirectional (ranging from 4 to 40mm with 4 mm intervals) and eleven bidirectional incremental distances (ranging from 2 to 42mm with 4 mm intervals). Some of these distances have identical length. In Figures 3 and 4, identification of unidirectional (U1 to U10) and bidirectional (B1-B11) lengths is reported.

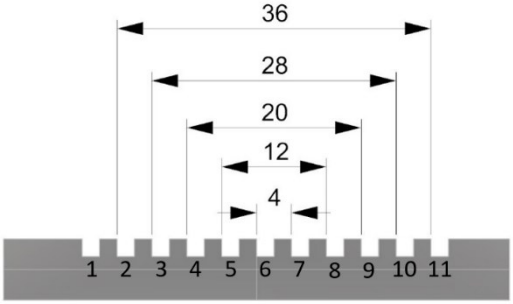

U1	4 mm
U2	12 mm
U3	20 mm
U4	28 mm
U5	36 mm

Figure A2 3. *Unidirectional lengths definitions*

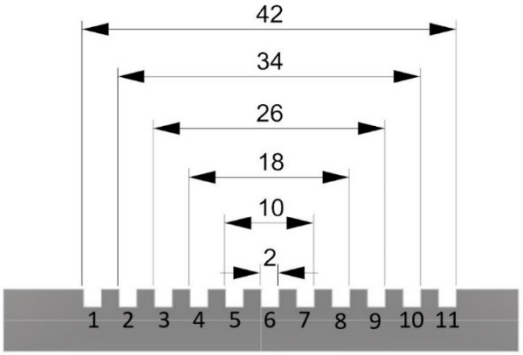

B1	2 mm
B2	10 mm
B3	18 mm
B4	26 mm
B5	34 mm
B6	42 mm

Figure A2 4. *Bidirectional lengths definitions*

Calibration uncertainty

Calibration uncertainty resulted from four main contributors:

1. Uncertainty component coming from grade I steel gauge block u_r
2. Reproducibility – the step gauge has been measured ten times u_p
3. Workpiece form error
   - Flatness u_w
4. Temperature effects
   - Deviation from the standard reference temperature u_e

Equation 1 has been used for the uncertainty assessment. The confidence level chosen is of 95%, to which a coverage factor k=2 corresponds.

$$U = k * \sqrt{u_r^2 + u_p^2 + u_w^2 + u_e^2} \quad (1)$$

All the uncertainty budget computed for each step gauges have been reported in Tables from A2 2 to 5.

Table A2 2 Calibrated measurements for step gauges made of POM-BLACK.

	POM-BLACK									
	POM-B #1		POM-B #2		POM-B #3		POM-B #4		POM-B #5	
	Y	U	Y	U	Y	U	Y	U	Y	U
U1	4,0012	0,0007	4,0006	0,0008	3,9985	0,0009	3,9990	0,0027	4,0022	0,0007
U2	11,9868	0,0014	11,9863	0,0013	11,9855	0,0013	11,9836	0,0028	11,9900	0,0012
U3	19,9817	0,0019	19,9788	0,0019	19,9774	0,0019	19,9764	0,0032	19,9834	0,0019
U4	27,9769	0,0026	27,9742	0,0026	27,9719	0,0026	27,9700	0,0036	27,9800	0,0026
U5	35,9745	0,0033	35,9713	0,0033	35,9695	0,0033	35,9671	0,0041	35,9793	0,0033
Average Value		**0,0020**		**0,0020**		**0,0020**		**0,0033**		**0,0019**
MAX-MIN range		**0,0026**		**0,0025**		**0,0024**		**0,0015**		**0,0025**
B1	2,0091	0,0010	2,0090	0,0009	2,0100	0,0006	2,0093	0,0027	2,0045	0,0007
B2	9,9789	0,0013	9,9780	0,0015	9,9766	0,0011	9,9755	0,0028	9,9855	0,0011

B3	17,9734	0,0019	17,9703	0,0020	17,9686	0,0017	17,9677	0,0031	17,9799	0,0017
B4	25,9689	0,0026	25,9660	0,0026	25,9632	0,0024	25,9620	0,0035	25,9765	0,0024
B5	33,9664	0,0033	33,9633	0,0033	33,9609	0,0031	33,9590	0,0041	33,9756	0,0031
B6	41,9625	0,0040	41,9590	0,0040	41,9554	0,0038	41,9540	0,0046	41,9720	0,0043
Average Value		**0,0026**		**0,0027**		**0,0021**		**0,0035**		**0,0022**
MAX-MIN range		**0,0026**		**0,0025**		**0,0032**		**0,0019**		**0,0036**

Table A2 3 Calibrated measurements for step gauges made of POM-COLORLESS.

POM-COLORLESS										
	POM-C #1		POM-C #2		POM-C #3		POM-C #4		POM-C #5	
	Y	U	Y	U	Y	U	Y	U	Y	U
U1	3,9973	0,0006	3,9931	0,0006	3,9984	0,0006	4,0022	0,0008	4,0019	0,0006
U2	11,9761	0,0012	11,9756	0,0011	11,9786	0,0012	11,9892	0,0013	11,9876	0,0012
U3	19,9626	0,0019	19,9633	0,0018	19,9666	0,0019	19,9855	0,0020	19,9806	0,0019
U4	27,9527	0,0026	27,9543	0,0026	27,9566	0,0026	27,9863	0,0026	27,9770	0,0026
U5	35,9461	0,0033	35,9486	0,0033	35,9499	0,0033	35,9891	0,0033	35,9755	0,0033
Average Value		**0,0019**		**0,0019**		**0,0019**		**0,0020**		**0,0019**
MAX-MIN range		**0,0027**		**0,0027**		**0,0027**		**0,0026**		**0,0027**
B1	2,0088	0,0005	2,0085	0,0006	2,0096	0,0005	1,9986	0,0006	2,0077	0,0006
B2	9,9684	0,0010	9,9688	0,0010	9,9699	0,0010	9,9891	0,0012	9,9801	0,0012
B3	17,9549	0,0017	17,9557	0,0018	17,9576	0,0017	17,9841	0,0018	17,9740	0,0017
B4	25,9453	0,0024	25,9465	0,0024	25,9477	0,0024	25,9816	0,0025	25,9692	0,0024
B5	33,9383	0,0031	33,9406	0,0032	33,9414	0,0031	33,9819	0,0032	33,9681	0,0031
B6	41,9297	0,0038	41,9338	0,0039	41,9311	0,0040	41,9935	0,0039	41,9642	0,0038
Average Value		**0,0024**		**0,0025**		**0,0021**		**0,0022**		**0,0022**
MAX-MIN range		**0,0028**		**0,0028**		**0,0035**		**0,0033**		**0,0033**

Table A2 4 Calibrated measurements for step gauges made of ABS-GREY.

ABS- GREY										
	ABS-G #1		ABS-G #2		ABS-G #3		ABS-G #4		ABS-G #5	
	Y	U	Y	U	Y	U	Y	U	Y	U
U1	3,9962	0,0005	3,9983	0,0008	3,9984	0,0007	3,9987	0,0007	3,9962	0,0006
U2	11,9875	0,0011	11,9925	0,0013	11,9951	0,0013	11,9949	0,0012	11,9831	0,0012
U3	19,9803	0,0018	19,9891	0,0019	19,9924	0,0019	19,9921	0,0019	19,9759	0,0019
U4	27,9736	0,0026	27,9868	0,0026	27,9907	0,0026	27,9915	0,0026	27,9703	0,0026
U5	35,9680	0,0033	35,9850	0,0033	35,9889	0,0034	35,9906	0,0033	35,9664	0,0033
Average Value		**0,0019**		**0,0020**		**0,0020**		**0,0019**		**0,0019**
MAX-MIN range		**0,0028**		**0,0025**		**0,0027**		**0,0026**		**0,0027**
B1	2,0119	0,0006	2,0092	0,0008	2,0119	0,0014	2,0104	0,0007	2,0110	0,0007
B2	9,9769	0,0011	9,9861	0,0012	9,9838	0,0012	9,9856	0,0012	9,9735	0,0012
B3	17,9701	0,0017	17,9820	0,0018	17,9812	0,0018	17,9822	0,0018	17,9661	0,0018
B4	25,9637	0,0024	25,9794	0,0024	25,9797	0,0025	25,9813	0,0025	25,9605	0,0025
B5	33,9583	0,0032	33,9779	0,0031	33,9783	0,0032	33,9803	0,0032	33,9568	0,0032
B6	41,9513	0,0039	41,9758	0,0038	41,9772	0,0039	41,9783	0,0039	41,9534	0,0039
Average Value		**0,0025**		**0,0025**		**0,0023**		**0,0022**		**0,0022**

MAX-MIN range	**0,0028**	**0,0027**	**0,0027**	**0,0032**	**0,0032**

Table A2 5 Calibrated measurements for step gauges made of POM-BLUE.

	POM-BLUE									
	POM-BL #1		POM-BL #2		POM-BL #3		POM-BL #4		POM-BL #5	
	Y	U	Y	U	Y	U	Y	U	Y	U
U1	4,0014	0,0006	4,0061	0,0020	3,9988	0,0045	4,0038	0,0006	3,9992	0,0007
U2	11,9904	0,0012	11,9916	0,0033	11,9891	0,0059	11,9948	0,0011	11,9816	0,0013
U3	19,9860	0,0019	19,9865	0,0033	19,9844	0,0078	19,9931	0,0019	19,9716	0,0019
U4	27,9837	0,0026	27,9840	0,0032	27,9831	0,0097	27,9937	0,0026	27,9645	0,0026
U5	35,9834	0,0033	35,9836	0,0035	35,9856	0,0109	35,9973	0,0033	35,9608	0,0034
Average Value		**0,0019**		**0,0031**		**0,0078**		**0,0019**		**0,0020**
MAX-MIN range		**0,0027**		**0,0015**		**0,0063**		**0,0027**		**0,0027**
B1	2,0092	0,0006	2,0095	0,0016	2,0097	0,0032	2,0086	0,0007	2,0090	0,0016
B2	9,9819	0,0010	9,9827	0,0016	9,9809	0,0095	9,9874	0,0011	9,9737	0,0013
B3	17,9773	0,0017	17,9778	0,0027	17,9760	0,0102	17,9856	0,0034	17,9642	0,0019
B4	25,9746	0,0024	25,9750	0,0032	25,9752	0,0138	25,9868	0,0025	25,9573	0,0026
B5	33,9745	0,0032	33,9744	0,0035	33,9775	0,0154	33,9900	0,0032	33,9532	0,0033
B6	41,9773	0,0038	41,9707	0,0042	41,9815	0,0163	41,9952	0,0039	41,9533	0,0040
Average Value		**0,0024**		**0,0030**		**0,0114**		**0,0025**		**0,0024**
MAX-MIN range		**0,0028**		**0,0026**		**0,0131**		**0,0032**		**0,0027**

References

[1] Sniderman B, Monika M, Cotteleer MJ. Industry 4.0 and manufacturing ecosystems. Deloitte Univ Press 2016:1–23.

[2] Imkamp D, Berthold J, Heizmann M, Kniel K, Peterek M, Schmitt R, et al. Challenges and trends in manufacturing measurement technology – the “Industrie 4.0” concept. J Sensors Sens Syst 2016;83:325–35. doi:10.1515/teme-2015-0081.

[3] Joint Committee For Guides In Metrology. International Vocabulary of Metrology. JCGM 2002012 2012;3:104. doi:10.1016/0263-2241(85)90006-5.

[4] ISO 14253-1:2017. Geometrical product specifications (GPS) -- Inspection by measurement of workpieces and measuring equipment -- Part 1: Decision rules for verifying conformity or nonconformity with specifications 2017.

[5] Jcgm JCFGIM. Evaluation of measurement data — Guide to the expression of uncertainty in measurement. Int Organ Stand Geneva ISBN 2008;50:134. doi:10.1373/clinchem.2003.030528.

[6] ISO 14253-2:2011. Geometrical product specifications (GPS) -- Inspection by measurement of workpieces and measuring equipment -- Part 2: Guidance for the estimation of uncertainty in GPS measurement, in calibration of measuring equipment and in product verification 2011.

[7] ISO 15530-3:2011. Geometrical product specifications (GPS) -- Coordinate measuring machines (CMM): Technique for determining the uncertainty of measurement -- Part 3: Use of calibrated workpieces or measurement standards 2011.

[8] Quinsat Y, Dubreuil L, lartigue C. A novel approach for in-situ detection of machining defects. Int J Adv Manuf Technol 2017;90:1625–38. doi:10.1007/s00170-016-9478-3.

[9] Kiraci E, Franciosa P, Turley GA, Olifent A, Attridge A, Williams MA. Moving towards in-line metrology: evaluation of a Laser Radar system for in-line dimensional inspection for automotive assembly systems. Int J Adv Manuf Technol 2017;91:69–78. doi:10.1007/s00170-016-9696-8.

[10] Sansoni G, Trebeschi M, Docchio F. State-of-The-Art and Applications of 3D Imaging Sensors in Industry, Cultural Heritage, Medicine, and Criminal Investigation. Sensors 2009;9:568–601. doi:10.3390/s90100568.

[11] Chen F, Brown G, Song M. Overview of three-dimensional shape measurement using optical methods. Opical Eng 2000;39:10–22. doi:10.1117/1.602438.

[12] Savio E, Chiffre L De, Schmitt R, Metrology G, Management Q. Metrology of freeform shaped parts 2007;56:810–35. doi:10.1016/j.cirp.2007.10.008.

[13] Barbero BR, Ureta ES. Comparative study of different digitization techniques and their accuracy. CAD Comput Aided Des 2011;43:188–206. doi:10.1016/j.cad.2010.11.005.

[14] Trifkovic B, Budak I, Todorovic A, Vukelic D, Lazic V, Puskar T. Comparative analysis on measuring performances of dental intraoral and extraoral optical 3D digitization systems. Meas J Int Meas Confed 2014;47:45–53. doi:10.1016/j.measurement.2013.08.051.

[15] Tóth T, Živčák J. A comparison of the outputs of 3D scanners. Procedia Eng 2014;69:393–401. doi:10.1016/j.proeng.2014.03.004.

[16] Zhou S, Xu J, Tao L, Yan Y. Performance evaluation of laser line scanner for in-process inspection of 3D geometries 2016:96843K. doi:10.1117/12.2241357.

[17] Bešić I, Van Gestel N, Kruth JP, Bleys P, Hodolič J. Accuracy improvement of laser line scanning

for feature measurements on CMM. Opt Lasers Eng 2011;49:1274–80. doi:10.1016/j.optlaseng.2011.06.009.

[18] Li F, Longstaff AP, Fletcher S, Myers A. Rapid and accurate reverse engineering of geometry based on a multi-sensor system. Int J Adv Manuf Technol 2014;74:369–82. doi:10.1007/s00170-014-5997-y.

[19] Gerbino S, Del Giudice DM, Staiano G, Lanzotti A, Martorelli M. On the influence of scanning factors on the laser scanner-based 3D inspection process. Int J Adv Manuf Technol 2016;84:1787–99. doi:10.1007/s00170-015-7830-7.

[20] Li F, Stoddart D, Hitchens C. Method to automatically register scattered point clouds based on principal pose estimation. Opt Eng 2017;56:044107. doi:10.1117/1.OE.56.4.044107.

[21] Poyraz Ö, Yilmaz O, Yasa E. INVESTIGATION OF FREE-FORM SURFACE RECONSTRUCTION TECHNIQUES FOR REVERSE ENGINEERING OF WORN-OUT GAS TURBINE BLADES : A CASE FOR REVERSE ENGINEERING OF WORN-OUT GAS TURBINE BLADES : 16th Int. Conf. Mach. Des. Prod. Izmir, Turkiye, 2014.

[22] Salvi J, Fernandez S, Pribanic T, Llado X. A state of the art in structured light patterns for surface profilometry. Pattern Recognit 2010;43:2666–80. doi:10.1016/j.patcog.2010.03.004.

[23] Bräuer-Burchardt C, Ölsner S, Kühmstedt P, Notni G. Comparison of calibration strategies for optical 3D scanners based on structured light projection using a new evaluation methodology. Proc. SPIE - Int. Soc. Opt. Eng., 2017. doi:10.1117/12.2269971.

[24] Luhmann T, Fraser C, Maas HG. Sensor modelling and camera calibration for close-range photogrammetry. ISPRS J Photogramm Remote Sens 2016;115:37–46. doi:10.1016/j.isprsjprs.2015.10.006.

[25] Huang J, Wu Q. A new reconstruction method based on fringe projection of three-dimensional measuring system. Opt Lasers Eng 2014;52:115–22. doi:10.1016/j.optlaseng.2013.07.002.

[26] Luhmann T. Close range photogrammetry for industrial applications. ISPRS J Photogramm Remote Sens 2010;65:558–69. doi:10.1016/j.isprsjprs.2010.06.003.

[27] Menna F, Sargeant B, Robson S. Improving automated 3D reconstruction methods via vision metrology. Proc SPIE - Int Soc Opt Eng 2015. doi:10.1117/12.2184974.

[28] Riveiro B, Arias P, Armesto J. Photogrammetry and laser scanner technology applied to length measurements in car testing laboratories. Measurement 2012;45:354–63. doi:10.1016/j.measurement.2011.11.010.

[29] Hosseininaveh A. A, Sargeant B, Erfani T, Robson S, Shortis M, Hess M, et al. Towards fully automatic reliable 3D acquisition: From designing imaging network to a complete and accurate point cloud. Rob Auton Syst 2014;62:1197–207. doi:10.1016/j.robot.2014.04.001.

[30] Zhang D-H, Liang J, Guo C, Chen Z-X. Application of photogrammetry technology to industrial inspection. Proc SPIE - Int Soc Opt Eng 2010;7546:2–7. doi:10.1117/12.852490.

[31] Barnfather JD, Goodfellow MJ, Abram T. Photogrammetric measurement process capability for metrology assisted robotic machining. Meas J Int Meas Confed 2016;78:29–41. doi:10.1016/j.measurement.2015.09.045.

[32] Zhao WL, Zhao C, Cheng JT, Yue HY. Accuracy Verification Method about Optical Three-Dimensional Measuring Instrument. Adv Mater Res 2010;142:204–8. doi:10.4028/www.scientific.net/AMR.142.204.

[33] Eiríksson ER, Wilm J, Pedersen DB, Aanæs H. Precision and Accuracy Parameters in Structured

Light 3-D Scanning. Int Arch Photogramm Remote Sens Spat Inf Sci 2016;XL-5/W8:7–15. doi:10.5194/isprsarchives-XL-5-W8-7-2016.

[34] Clark J, Robson S. Accuracy of Measurements Made With a Cyrax 2500 Laser Scanner Against Surfaces of Known Colour. Surv Rev 2004;37:626–38. doi:10.1179/sre.2004.37.294.626doi.org/10.1179/sre.2004.37.294.626.

[35] Dury MR, Woodward SD, Brown SB, McCarthy MB. Surface finish and 3D optical scanner measurement performance for precision engineering. Proc - ASPE 2015 Annu Meet 2015:419–23.

[36] Kruth JP, Bartscher M, Carmignato S, Schmitt R, De Chiffre L, Weckenmann A. Computed tomography for dimensional metrology. CIRP Ann - Manuf Technol 2011;60:821–42. doi:10.1016/j.cirp.2011.05.006.

[37] De Chiffre L, Carmignato S, Kruth J, Schmitt R, Weckenmann A. Industrial applications of computed tomography. CIRP Ann - Manuf Technol 2014;63:655–77. doi:10.1016/j.cirp.2014.05.011.

[38] Everton SK, Hirsch M, Stravroulakis P, Leach RK, Clare AT. Review of in-situ process monitoring and in-situ metrology for metal additive manufacturing. JMADE 2016;95:431–45. doi:10.1016/j.matdes.2016.01.099.

[39] Cannella E, Nielsen EK, Stolfi A. Designing a tool system for lowering friction during the ejection of in-die sintered micro gears. Micromachines 2017;8:1–15. doi:10.3390/mi8070214.

[40] Cantatore A, Angel J, De Chiffre L. Material investigation for manufacturing of reference step gauges for CT scanning verification. Proc 12th Euspen Int Conf – Stock 2012:2010–3.

[41] Angel J, De Chiffre L, Kruth JP, Tan Y, Dewulf W. Performance evaluation of CT measurements made on step gauges using statistical methodologies. CIRP J Manuf Sci Technol 2015;11:68–72. doi:10.1016/j.cirpj.2015.08.002.

[42] Gameros A, De Chiffre L, Siller HR, Hiller J, Genta G. A reverse engineering methodology for nickel alloy turbine blades with internal features. CIRP J Manuf Sci Technol 2015;9:116–24. doi:10.1016/j.cirpj.2014.12.001.

[43] Angel JAB. Quality assurance of CT scanning for industrial applications. PhD Thesis. Technical University of Denmark, 2014.

[44] Stolfi A, De Chiffre L. CT crown for on-machine scale calibration in Computed Tomography. Proc. 16th Int. Conf. Eur. Soc. Precis. Eng. Nanotechnology, EUSPEN, 2016.

[45] Stolfi A, De Chiffre L. 3D artefact for concurrent scale calibration in Computed Tomography. CIRP Ann - Manuf Technol 2016;65:499–502. doi:10.1016/j.cirp.2016.04.069.

[46] Alting L, Kimura F, Hansen HN, Bissacco G. Micro Engineering. CIRP Ann - Manuf Technol 2003;52:635–57. doi:10.1016/S0007-8506(07)60208-X.

[47] Giorleo L, Ceretti E, Giardini C. Optimization of laser micromachining process for biomedical device fabrication. Int J Adv Manuf Technol 2016;82:901–7. doi:10.1007/s00170-015-7450-2.

[48] D'Urso G, Maccarini G, Ravasio C. Influence of electrode material in micro-EDM drilling of stainless steel and tungsten carbide. Int J Adv Manuf Technol 2016;85:2013–25. doi:10.1007/s00170-015-7010-9.

[49] Baruffi F, Calaon M, Tosello G. Effects of micro-injection moulding process parameters on accuracy and precision of thermoplastic elastomer micro rings. Precis Eng 2018;51:353–61. doi:10.1016/j.precisioneng.2017.09.006.

[50] Vaezi M, Seitz H, Yang S. A review on 3D micro-additive manufacturing technologies. Int J Adv Manuf Technol 2013;67:1721–54. doi:10.1007/s00170-012-4605-2.

[51] Thalmann R, Meli F, Küng A. State of the Art of Tactile Micro Coordinate Metrology. Appl Sci 2016;6:150. doi:10.3390/app6050150.

[52] Hansen HN, Carneiro K, Haitjema H, De Chiffre L. Dimensional Micro and Nano Metrology. CIRP Ann - Manuf Technol 2006;55(2):721–43.

[53] Dai G, Neugebauer M, Stein M, Bütefisch S, Neuschaefer-Rube U. Overview of 3D Micro- and Nanocoordinate Metrology at PTB. Appl Sci 2016;6:257. doi:10.3390/app6090257.

[54] De Chiffre L, Hansen HN, Andreasen JL, Savio E, Carmignato S. Geometrical Metrology and Machine Testing.Textbook. Polyteknisk Forlag; 2015.

[55] Valiño G, Zapico P, Fernández P, Rico JC, Mateos S, Blanco D. Measurement and correction of the slope angle of flat surfaces digitized by a conoscopic holography system. Precis Eng 2016;46:369–76. doi:10.1016/j.precisioneng.2016.06.006.

[56] Valiño G, Rico JC, Zapico P, Fernàndez P. Influence of scanning strategies on measuring and surface digitising by means of a conoscopic holography sensor integrated in a machining centre. Int J Mechatronics Manuf Syst 2017;10:2004–6.

[57] Lehmann P, Tereschenko S, Xie W. Fundamental aspects of resolution and precision in vertical scanning white-light interferometry. Surf Topogr Metrol Prop 2016;4. doi:10.1088/2051-672X/4/2/024004.

[58] Fleischle D, Lyda W, Mauch F, Osten W. Optical metrology for process control: modeling and simulation of sensors for a comparison of different measurement principles. Proc SPIE 2010;7718:77181D–12. doi:10.1117/12.855053.

[59] De Chiffre L, Carli L, Eriksen RS. Multiple height calibration artefact for 3D microscopy. CIRP Ann - Manuf Technol 2011;60:535–8. doi:10.1016/j.cirp.2011.03.054.

[60] Yagüe JA, Tosello G, Carmignato S, Ontiveros S, Jiménez R, Gasparin S, et al. Measurement of micro moulded parts by computed tomography and comparison to optical and tactile techniques. Proc 11th Int Conf Eur Soc Precis Eng Nanotechnology, EUSPEN 2011 2011;1:76–9.

[61] Jiménez R, Torralba M, Yagüe-Fabra J, Ontiveros S, Tosello G. Experimental Approach for the Uncertainty Assessment of 3D Complex Geometry Dimensional Measurements Using Computed Tomography at the mm and Sub-mm Scales. Sensors 2017;17:1137. doi:10.3390/s17051137.

[62] Peggs GN, Maropoulos PG, Hughes EB, Forbes AB, Robson S, Ziebart M, et al. Recent developments in large-scale dimensional metrology. Proc Inst Mech Eng Part B J Eng Manuf 2009;223:571–95. doi:10.1243/09544054JEM1284.

[63] Maté González MÁ, Yravedra J, González-Aguilera D, Palomeque-González JF, Domínguez-Rodrigo M. Micro-photogrammetric characterization of cut marks on bones. J Archaeol Sci 2015;62:128–42. doi:10.1016/j.jas.2015.08.006.

[64] Rodríguez-martín M, Lagüela S, González-aguilera D, Rodríguez-gonzálvez P. Procedure for quality inspection of welds based on macro-photogrammetric three-dimensional reconstruction. Opt Laser Technol 2015;73:54–62.

[65] Galantucci LM, Pesce M, Lavecchia F. A powerful scanning methodology for 3D measurements of small parts with complex surfaces and sub millimeter-sized features, based on close range photogrammetry. Precis Eng 2015. doi:10.1016/j.precisioneng.2015.07.010.

[66] Shortis MR, Bellman CJ, Robson S, Johnston GJ, Johnson GW. Stability of Zoom and Fixed Lenses

used with Digital SLR Cameras. Int Arch Photogramm Remote Sensing, Spat Inf Sci 2006;36:285–90.

[67] Galantucci LM, Lavecchia F, Percoco G. Multistack Close Range Photogrammetry for Low Cost Submillimeter Metrology. J Comput Inf Sci Eng 2013;13:044501. doi:10.1115/1.4024973.

[68] Gallo A, Muzzupappa M, Bruno F. 3D reconstruction of small sized objects from a sequence of multi-focused images. J Cult Herit 2014;15:173–82. doi:10.1016/j.culher.2013.04.009.

[69] Nocerino E, Menna F, Remondino F, Beraldin JA, Cournoyer L, Reain G. Experiments on calibrating tilt-shift lenses for close-range photogrammetry. Int Arch Photogramm Remote Sens Spat Inf Sci - ISPRS Arch 2016;41:99–105. doi:10.5194/isprsarchives-XLI-B5-99-2016.

[70] Galantucci LM, Pesce M, Lavecchia F. A stereo photogrammetry scanning methodology, for precise and accurate 3D digitization of small parts with sub-millimeter sized features. CIRP Ann - Manuf Technol 2015;64:507–10. doi:10.1016/j.cirp.2015.04.016.

[71] Percoco G, Lavecchia F, Salmerón AJS. Preliminary Study on the 3D Digitization of Millimeter Scale Products by Means of Photogrammetry. Procedia CIRP 2015;33:257–62. doi:10.1016/j.procir.2015.06.046.

[72] Percoco G, Antonio JS. Photogrammetric measurement of 3D freeform millimetre-sized objects with micro features : an experimental validation of the close-range camera calibration model for narrow angles of view. Meas Sci Technol 2015;26. doi:10.1088/0957-0233/26/9/095203.

[73] Angelo Beraldin J, Mackinnon D, Cournoyer L. Metrological characterization of 3D imaging systems : progress report on standards developments. Int Congr Metrol 2015;3:1–21. doi:10.1051/metrology/20150013003.

[74] ISO 10360-7:2011. Geometrical product specifications (GPS) — Acceptance and reverification tests for coordinate measuring machines (CMM) — Part 7: CMMs equipped with imaging probing systems 2011.

[75] ISO 10360-8:2013. Geometrical product specifications (GPS) -- Acceptance and reverification tests for coordinate measuring systems (CMS) -- Part 8: CMMs with optical distance sensors 2013.

[76] VDI-Standard: VDI/VDE 2617 Blatt 6.2. Accuracy of coordinate measuring machines - Characteristics and their testing - Guideline for the application of DIN EN ISO 10360 to coordinate measuring machines with optical distance sensors 2005.

[77] VDI-Standard: VDI/VDE 2634 Blatt 2. Optical 3-D measuring systems - Optical systems based on area scanning 2012.

[78] VDI-Standard: VDI/VDE 2634 Blatt 3. Optical 3D-measuring systems - Multiple view systems based on area scanning 2008.

[79] McCarthy MB, Brown SB, Evenden A, Robinson AD. NPL freeform artefact for verification of non-contact measuring systems. Soc PhotoOptical 2011;7864:78640K–78640K–13. doi:10.1117/12.876705.

[80] Chiffre L De, Hansen HN. Metrological Limitations of Optical Probing Techniques. Ann CIRP 1995;44:5–8.

[81] Lavecchia F, Guerra MG, Galantucci LM. The influence of software algorithms on photogrammetric micro-feature measurement's uncertainty. Int J Adv Manuf Technol 2017:1–15. doi:10.1007/s00170-017-0786-z.

[82] Stamatopoulos C, Fraser CS. Calibration of long focal length cameras in close range

photogrammetry. Photogramm Rec 2011;26:339–60. doi:10.1111/j.1477-9730.2011.00648.x.

[83] Nguyen C V., Lovell DR, Adcock M, La Salle J. Capturing natural-colour 3D models of insects for species discovery and diagnostics. PLoS One 2014;9. doi:10.1371/journal.pone.0094346.

[84] Remondino F. Detectors and Descriptors for Photogrammetric Applications. Int Arch Photogramm Remote Sens Spat Inf Sci 2006:2–7.

[85] Lowe DG. Distinctive Image Features from Scale-Invariant Keypoints. Int J Comput Vis 2004;60:91–110. doi:10.1023/B:VISI.0000029664.99615.94.

[86] Bay H, Ess A, Tuytelaars T, Van Gool L. Speeded-Up Robust Features (SURF). Comput Vis Image Underst 2008;110:346–59. doi:10.1016/j.cviu.2007.09.014.

[87] Agisoft Photoscan User Manual 2016. http://www.agisoft.com/pdf/photoscan-pro_1_2_en.pdf.

[88] Fraser CS, Stamatopoulos C. Automated Target-Free Camera Calibration. ASPRS 2014 Annu Conf Louisville, Kentucky 2014.

[89] Barazzetti L, Mussio L, Remondino F, Scaioni M. Targetless camera calibration. Int Arch Photogramm Remote Sens Spat Inf Sci 2011;XXXVIII:W16. doi:10.5194/isprsarchives-XXXVIII-5-W16-335-2011.

[90] Galantucci LM, Guerra MG, Lavecchia F. Photogrammetry Applied to Small and Micro Scaled Objects: A Review. Lect Notes Mech Eng 2018:57–77. doi:https://doi.org/10.1007/978-3-319-89563-5_4.

[91] Lavecchia F, Guerra MG, Galantucci LM. Performance verification of a photogrammetric scanning system for micro-parts using a three-dimensional artifact: adjustment and calibration. Int J Adv Manuf Technol 2018;96:4267–79. doi:10.1007/s00170-018-1806-3.

[92] Dury MR, Brown S., McCarthy M., Woodward S. 3D Optical Scanner Dimensional Verification Facility at the NPL's "National FreeForm Centre." Laser Metrol Mach Perform XI - 11th Int Conf Exhib Laser Metrol Mach Tool, C Robot Performance, LAMDAMAP 2015:187–97.

[93] ISO 5436-1:2000 Geometrical Product Specifications (GPS) – Surface texture: Profile method; Measurement standards – Part 1: Material measures. 2000.

[94] Lavecchia F, Guerra MG, Galantucci LM. The influence of software algorithms on photogrammetric micro-feature measurement ' s uncertainty 2017:3991–4005. doi:10.1007/s00170-017-0786-z.

[95] UNI EN ISO 4288:2000 Geometrical Product Specifications (GPS), Surface texture: Profile method, Rules and procedures for the assessment of surface texture 2000.

[96] https://www.cloudcompare.org/ 2018.

[97] https://it.3dsystems.com/software/geomagic-control-x 2018.

[98] Schnabel R, Wahl R, Klein R. Efficient {RANSAC} for point-cloud shape detection. Comput Graph Forum 2007;26:214–26.

[99] Carmignato S, Aloisi V, Medeossi F, Zanini F, Savio E. Influence of surface roughness on computed tomography dimensional measurements. CIRP Ann - Manuf Technol 2017;66:499–502. doi:10.1016/j.cirp.2017.04.067.

[100] Guerra MG, Volpone C, Galantucci LM, Percoco G. Photogrammetric measurements of 3D printed microfluidic devices. Addit Manuf 2018;21:53–62. doi:10.1016/j.addma.2018.02.013.

[101] Percoco G, Modica F, Fanelli S. Image analysis for 3D micro-features: A new hybrid measurement

method. Precis Eng 2017;48. doi:10.1016/j.precisioneng.2016.11.012.

[102] Cantatore A, De Chiffre L, Carmignato S. Investigation on a replica step gauge for optical 3D scanning of micro parts. 10th Int. Conf. Eur. Soc. Precis. Eng. Nanotechnol., 2010.

[103] Wilm J, Madruga DG, Jensen JN, Gregersen SS, Brix ME, Guerra MG, et al. Effects of subsurface scattering on the accuracy of optical 3D measurements using miniature polymer step gauges. Proc. euspen's 18th Int. Conf. Exhib. Venice, IT, 2018euspen's 18th Int. Conf. Exhib. Venice, IT, 2018, p. 449–50.

[104] Percoco G, Guerra MG, Sanchez-Salmeron A-J, Galantucci LM. Experimental investigation on camera calibration for 3D photogrammetric scanning of micro-features for micrometric resolution. Int J Adv Manuf Technol 2017;91:2935–47.

[105] Tang R, Fritsch D. Correlation Analysis of Camera Self-Calibration in Close Range Photogrammetry. Photogramm Rec 2013;28:86–95. doi:10.1111/phor.12009.